

*High-performance Electrospun
Polymer Nanofibres and Their Composite
Materials with Hectorite*

DISSERTATION

zur Erlangung des akademischen Grades einer Doktorin/eines
Doktors der Naturwissenschaften (Dr. rer. nat.)
in der Bayreuther Graduiertenschule für Mathematik und
Naturwissenschaften (BayNAT)
der Universität Bayreuth

vorgelegt von

Jian Zhu

Chongyi County, Jiangxi Province, China

Bayreuth 2019

This doctoral thesis was prepared at the department of Macromolecular Chemistry II at the University of Bayreuth from 10/2015 until 9/2019 and was supervised by Prof. Dr. Seema Agarwal.

This is a full reprint of the dissertation submitted to obtain the academic degree of Doctor of Natural Sciences (Dr. rer. nat.) and approved by the Bayreuth Graduate School of Mathematical and Natural Sciences (BayNAT) of the University of Bayreuth.

Date of submission: 02.07.2019

Date of defence: 11.09.2019

Acting director: Prof. Dr. Dirk Schüler

Doctoral committee:

Prof. Dr. Seema Agarwal	(reviewer)
Prof. Dr. Josef Breu	(reviewer)
Prof. Dr. Matthias Breuning	(chairman)
Prof. Dr. Peter Strohsriegl	

Table of content

Table of content

Table of content	1
List of Figures	3
List of Symbols and Abbreviations	7
Summary/Zusammenfassung	9
Summary	9
Zusammenfassung.....	12
1 Introduction	15
1.1 Motivation and Aim	15
1.2 Electrospinning	16
1.2.1 Device and Principle of Electrospinning	17
1.2.2 Materials for Electrospinning	21
1.2.3 Morphology and Structure of Electrospun Fibres.....	24
1.2.4 Application of Electrospun Nanofibres.....	27
1.3 Electrospun Conjugated Rigid-Rod Polymers	28
1.3.1 Development of Rigid-Rod Polymers.....	28
1.3.2 Electrospinning of Rigid-Rod Polymers	33
1.4 Electrospun Nanofibre-Based Sponges.....	35
1.5 Polymer/Clay Composite Materials	39
1.5.1 Polymer/Clay Nanocomposite for Flame Retardant Application	40
1.5.2 Strong Polymer/Clay Nanocomposite for Gas Barrier Application.....	43
1.6 References	49
2. An Overview of The Thesis	68
2.1 Nanofibre Preparation of Non-processable Polymers by Solid-State Polymerization of Molecularly Self-Assembled Monomers	70
2.2 Low-density, Thermally Stable and Intrinsic Flame-Retardant Poly(bis(benzimidazo)Benzophenanthrolinedione) Sponge.....	74
2.3 Gradient-Structured Non-flammable Flexible Polymer Membranes.....	78

Table of content

2.4 Filter-Through Method of Making Highly Efficient Polymer-Clay Nanocomposite Membranes.....	82
3. Outlook.....	85
4. Acknowledgments	86
5. Appendix	88
5.1 Nanofibre Preparation of Non-Processable Polymers by Solid-State Polymerization of Molecularly Self-Assembled Monomers	88
5.2 Low Density, Thermally Stable, and Intrinsic Flame Retardant Poly(bis(benzimidazo)Benzophenanthrolinedione) Sponge.....	110
5.3 Gradient-Structured Nonflammable Flexible Polymer Membranes	119
5.4 Filter-Through Method of Making Highly Efficient Polymer-Clay Nanocomposite Membranes.....	135
6. List of Publications	151

List of Figures

List of Figures

Scheme 1. Synthetic scheme and chemical structure of BBB.....	15
Figure 1-1. (a) Basic device for electrospinning. (b) Diagram showing the path of an electrospun jet. (b) Reprinted with permission from ref 2. Copyright (2019) American Chemical Society.	18
Figure 1-2. (a) Examples of nozzles for multiple-needle electrospinning. (b) Industrial production line of multiple-needle electrospinning of PI nanofibrous mats/nonwovens (from Jiangxi Advanced Nanofibre Technology Co.). (c) Examples of coaxial nozzles. (d) Photographs of electrospinning processes that use a jagged metallic plate and (e) a stepped pyramid as a spinneret. (f) Photographs of electrospinning processes using a rotary metal cylinder, disc and ball as a spinneret. (a) Adapted with permission from ref 37. Copyright 2018 Wiley-VCH. (d) Reprinted with permission from ref 42. Copyright 2008 AIP Publishing. (e) Reprinted with permission from ref 43. Copyright 2015 Elsevier. (f) Reprinted with permission from ref 44. Copyright 2012 Taylor & Francis.	20
Figure 1-3. Micro/nanofibres with multi-structures obtained by the electrospinning technique: (a) Cylinder, (b) flatted ribbon, (c) bead-on-string, (d) surface porous, (e) side-by-side, (f) branched, (g) tube structure, (h) multichannel, (i) wire-in-tube, (j) multiwall, (k) vesicle, (l) pea-like, (m) aligned nanofibre belt, (n) nanofibre yarn and (o) nanoarchitecture networks. (a)-(l) Reprinted with permission from ref 65. Copyright 2018 Wiley-VCH. (m) Reprinted with permission from ref 80. Copyright 2008 IOP Publishing. (n) Reprinted with permission from ref 81. Copyright 2012 Taylor & Francis. (o) Reprinted with permission from ref 82. Copyright 2019 Springer Nature.	26
Figure 1-4. (a, b) Synthetic and chemical structures of (a) BBB and (b) BBL polymers. (c) Helical arrangement of BBB molecules. (d) Structures of the soluble Lewis acid (MX_n) complexes of BBB polymer. (c) Reprinted with permission from ref 126. Copyright (1995) American Chemical Society. (d) Adapted with permission from ref	

List of Figures

129. Copyright (1990) American Chemical Society.30
- Figure 1-5.** (a) Photos show the elasticity of CNTs sponge from chemical vapour deposition. (b) CNTs sponge for cleaning up large areas of oil. (c) Photo of CNT-graphene sponge. (d) Elasticity-responsive conductivity of CNT-graphene sponge. (e) Photo of raw cotton-based carbon fibre sponge under the water. (f) Removal of the loaded organic solvent via combustion. (a) and (b) Reprinted with permission from ref 152. Copyright 2010 Wiley-VCH. (c) and (d) Reprinted with permission from ref 154. Copyright 2013 Wiley-VCH. (e) and (f) Reprinted with permission from ref 155. Copyright 2013 Wiley-VCH.36
- Figure 1-6.** (a) PI sponge as a thermal insulator. (b) Electrical conductivity of PI/AgNW sponge changes with compression strain. (c) Thermal conductivity of PBO sponges with different density. (d) Ignition test of PBO sponges. (e) Synthesis of CMP aerogels. (f) CMP aerogel as a thermal insulator. (g) Infrared images of CMP aerogel-carbon black composite materials under different illumination and time. (a) Reprinted with permission from ref 159. Copyright (2017) American Chemical Society. (b) Reprinted with permission from ref 160. Copyright (2017) American Chemical Society. (c) and (d) Reprinted with permission from ref 165. Copyright (2018) Royal Society of Chemistry. (e)-(g) Reprinted with permission from ref 166. Copyright (2018) Royal Society of Chemistry39
- Figure 1-7.** (a) Illustration of model of flame-retardant action. (b) Sketch of the fire-shielding mechanism attributed to the CNF/clay coating on epoxy composites. (a) Reprinted with permission from ref 175. Copyright (2017) Elsevier. (b) Reprinted with permission from ref 189. Copyright (2013) Wiley-VCH.41
- Figure 1-8.** (a) Model of gas diffusion through the parallel arranged platelets nanocomposite. (b) Predictions of Nielsen's model for the relative permeability as a function of platelets volume fraction for different particle aspect ratios. (c)-(f) The preparation methods of films or coating containing clay; (c) solution casting; (d) doctor blading and spray coating; (e) layer by layer assembling; (f) vertical and horizontal

List of Figures

deposition (Langmuir-Blodgett technique). (a) and (b) Reprinted with permission from ref 203. Copyright (2009) Elsevier. (c), (e) and (f) Reprinted with permission from ref 171. Copyright (2011) Royal Society of Chemistry.	46
Figure 2-1. Pictorial summary of the prepared work as described in section 2.1-2.4.	68
Scheme 2-1. Synthetic scheme and chemical structure of the BBB polymer.	70
Figure 2-2. Procedure of the preparation of BBB nanofibres by electrospinning.	71
Figure 2-3. (a) Fourier transform infrared spectra of PVP, as-spun precursor nanofibres and BBB nanofibres. (b) Possible routes for the polymerization of NTCA and DAB to BBB.....	72
Figure 2-4. (a) TGA curve of BBB fibres and TGA curve of BBB nanofibres. (b) Stress-strain curves of the BBB nanofibre belt prepared without hot-stretching and with hot-stretching at 5 N. (c) Strength and (d) modulus of individual BBB nanofibres with different diameters (results from PND5 and PVP (8:2) and 500 °C treated sample). .	73
Figure 2-5. (a) Microphotograph of BBB short fibres. (b) Length distribution of BBB short fibres. (c) SEM images and photos of BBB sponge from pure water dispersion and (d) BBB sponge from PVA glue after annealing treatment. (e) Compression test of BBB sponge from PVA glue with different density. (f) TGA curves of BBB sponge in air and N ₂ condition.	75
Figure 2-6. (a) Thermal conductivity and (b) thermal diffusivity of BBB sponge changes with density. (c) Digital photos and IR camera photos of BBB sponge and (d) 50 % compressed BBB sponge on a high-temperature plate.	76
Figure 2-7. Photos of (a) polystyrene sponge, (b) PI sponge and (c) BBB sponge put on a naked flame.	76
Figure 2-8. (a) Preparation process for the Hec/BBB membranes. SEM images of bottom (b) and top (c) side of the membrane of H-61/B-36 (61 and 36 is the percentage of Hec and BBB fibres). (d) SEM image of cross-section and (d) Si atom mapping obtained from energy-dispersive X-ray spectrometry of the H-61/B-36 membrane. .	79
Figure 2-9. (a) Pure BBB fibre membrane fixed on a steel frame to shield the flame. (b)	

List of Figures

Cotton ball protected with the Hec/BBB composite membranes. Inset shows photos of the Hec/BBB membrane after the test. (c) Photos of the Hec/BBB membrane (H-73/B-23, 73 and 23 is the percentage of Hec and BBB fibres) placed on the flame of a Campinggaz burner (1400 °C). (d) Ignition process for the Hec/BBB (H-73/B-23) membranes in a 100 % O ₂ atmosphere. (e) Photos of the Hec/BBB membranes before and after the cone calorimeter test.	80
Figure 2-10. Fabrication procedure of TPU/PVP-Hec/TPU films.....	83
Figure 2-11. SEM images of the surface (a) and cross-section (b) of a PVP-Hec coated TPU mat. Photos of the PVP-Hec coated with TPU mat (c) and three-layered film (d) after hot press.	83
Figure 2-12. (a) The transmittances of the final laminate. (b) X-ray diffraction patterns of the neat pressed TPU support, Hec and PVP-Hec coated with TPU support, and the final hot-pressed laminate. (c) Transmission electron microscopy image of the alignment of the clay nanoplatelets in the interlayer PVP-Hec nanocomposite. (d) Stress-strain curves of final hot-pressed laminate. (e) Comparison of the elasticity modulus of the laminates of this work and the TPU nanocomposites of other publications. (f) Oxygen permeability of final laminate membranes changes with amounts of Hec at 50 % RH. The “tortuous pathway” created by incorporation of delaminated Hec nanosheets into a PVP matrix is also illustrated.	84

List of Symbols and Abbreviations

List of Symbols and Abbreviations

°C	degree celsius
2D	two-dimensional
3D	three-dimensional
BBB	poly(bisbenzimidazobenzophenanthroline-dione)
BBL	poly(benzobisimidazobenzophenanthroline)
CA	cellulose acetate
CB	carbon black
cm	centimeter
CMP	conjugated microporous polymer
CNFs	carbon nanofibres
CNTs	carbon nanotubes
DAB	3,3'-diaminobenzidine
FD	freeze-drying
FTIR	Fourier transform infrared spectroscopy
g	gram
GPa	giga pascal
h	hours
Hec	Na-hectorite
K	kelvin
m	meter
mg	milligram
min	minute
MMT	montmorillonite
MPa	mega pascal
MSA	methane sulfonic acid
mW	milliwatt
nm	nanometer

List of Symbols and Abbreviations

NTCA	1,4,5,8-naphthalene tetracarboxylic acid
OTR	oxygen transmission rate
PBI	polybenzimidazole
PBO	poly(p-phenylene benzobisoxazole)
PCL	polycaprolactone
PEO	polyethylene oxide
PET	poly(ethylene terephthalate)
PIs	polyimides
PVA	poly(vinyl alcohol)
PVP	poly(vinyl pyrrolidone)
RH	relative humidity
s	second
S	siemens
SEM	scanning electron microscopy
TEM	transmission electron microscopy
TGA	thermogravimetric analysis
TPU	thermoplastic polyurethane
μm	micrometer
W	watt
wt. %	weight percent
XRD	X-ray diffraction

Summary/Zusammenfassung

Summary

Poly(bisbenzimidazobenzophenanthroline-dione) (BBB) is a heterocyclic rigid-rod polymer exhibiting excellent thermal and mechanical performances. It is made by the condensation of 1,4,5,8-naphthalene tetracarboxylic acid (NTCA) and 3,3'-diaminobenzidine (DAB) at a high temperature. The bottleneck in the use of BBB polymer is its insolubility in organic solvents and an extremely high softening point (higher than its decomposition temperature), that makes processing to films, fibres, sponges or, in fact, to any other form impossible. The aim of this work is to provide methods of processing BBB to fibres, sponges and membranes and study their thermal and mechanical properties.

A new bottom-up approach was established for making BBB fibres by electrospinning to overcome the obstacle of insolubility and infusibility of BBB for processing fibre. The approach involved templet-assisted solid-state polymerization of the self-assembled starting monomers (NTCA and DAB) in fibre form. The self-assembled monomers were electrospun together with a templet polymer (any polymer that can be pyrolysed at a low temperature). Heating of the fibres at a temperature above 460 °C led to the polycondensation of self-assembled monomers to BBB polymer with simultaneous degradation and removal of the templet sacrificial polymer. A structural characterization, morphology study, thermal stability and mechanical testing were carried out for both a single and an aligned fibre belt. Electrospun BBB nanofibre showed an excellent thermal resistant property with the degradation onset temperature above 600 °C and a 5 % weight loss temperature of 640 °C in a N₂ atmosphere. A single BBB and an aligned fibre belt showed a very high strength of 1.43 ± 0.26 GPa (226 nm diameter) and 364.75 ± 4.76 MPa, respectively.

Furthermore, the BBB fibres were used for making three-dimensional open cell, low-density (≤ 13.9 mg cm⁻³), compressible (more than 90 % recovery after 50 %

Summary/Zusammenfassung

compression), intrinsic flame retardant and thermal insulating (thermal conductivity of 0.028-0.038 W m⁻¹K⁻¹) sponges. The sponges are made by the self-assembly of short BBB fibres (50–500 µm in length) in an aqueous dispersion during freeze-drying. The use of a sacrificial glue (poly(vinyl alcohol)) was systematically studied for improving the mechanical stability of the sponges.

The short electrospun fibres' dispersion can also be used for making a porous membrane using the wet-laid process. In this method, the vacuum-assisted filtration and drying of the short fibre dispersion provides a porous membrane by percolation of short fibres in the form of a randomly arranged fibre network. The BBB porous membranes made by this method were mechanically weak (0.04 MPa). Therefore, composite membranes of BBB with layered silicate (Na-hectorite) were studied. The composite membranes neither sustained flame, burned with smoke nor exhibited melt dripping. These porous, low-density and mechanical flexible Hec/BBB membranes showed a high char yield of 80–94 %, low thermal conductivity of 0.028–0.051 W m⁻¹K⁻¹ and a great flame-shielding effect. Such membranes are highly promising for use as lightweight construction materials and protective clothing.

Electrospun membranes with hierarchical pore structure and variable pore size are used extensively for air (high-efficiency particulate air [HEPA], ultra-low particulate air [ULPA]) and bacterial filtration. In a model study, as a last part of the work, a novel aspect of particulate filtration through electrospun thermoplastic porous membranes (TPU) is studied for the first time for making flexible, lightweight and strong polymer membranes with enhanced gas-barrier properties. The high-aspect ratio (≈ 20000) delaminated melt synthesized layered silicate (Na-hectorite) is self-assembled in a polymer matrix as a barrier-layer between two electrospun membranes by filtration and, subsequently, hot-pressed, which leads to enhanced gas-barrier properties. A highly filled (> 25 wt.%) efficient gas-barrier polymer membrane with perfectly aligned synthetic high aspect ratio hectorite of a variable and considerable thickness (up to 5 µm) can be made. The tensile modulus increased

Summary/Zusammenfassung

by up to a factor of > 60 and remarkable reduction of the oxygen permeability of 98.8 % for the composite membrane compared to the neat TPU was observed. The electrospun membrane polymer might be varied in the future, including the use of BBB polymer for combining material properties with layered silicates to generate high-performance membranes.

The results are published in peer-reviewed journals: *Nanoscale*, **2017**, 9(46), 18169-18174; *Macromol. Mater. Eng.*, **2018**, 303(4), 1700615; *ACS Appl. Mater. Interfaces*, **2019**, 11 (12), 11876-11883; *Macromol. Mater. Eng.*, **2019**, 1800779.

Zusammenfassung

Poly(bisbenzimidazobenzophenanthrolindione) (BBB) ist ein heterozyklisches *rigid-rod* Polymer mit hervorragenden thermischen und mechanischen Eigenschaften. Es wird durch Polykondensation von 1,4,5,8-Naphthalintetracarbonsäure (NTCA) und 3,3'-Diaminobenzidin (DAB) bei hohen Temperaturen erhalten. Das Problem bei der Verwendung von BBB ist dessen Unlöslichkeit in organischen Lösungsmitteln und die extrem hohe Erweichungstemperatur (oberhalb der Zersetzungstemperatur), was die Verarbeitung zu Filmen, Fasern, Schwämmen oder andere Formen unmöglich macht. Das Ziel dieser Arbeit ist es, Verarbeitungsmöglichkeiten von BBB zu Fasern, Schwämmen und Membranen zu entwickeln und deren thermische und mechanische Eigenschaften zu untersuchen.

Eine neue *bottom-up*-Methode zur Herstellung von BBB Fasern wurde durch Elektrospinning etabliert, um das Hindernis der Unlöslich- und Unschmelzbarkeit von BBB zu überwinden. Die Methode beinhaltet temperatur-assistierte Festkörperpolymerisation von selbstorganisierten Monomeren (NTCA und DAB) in Faserform. Die selbstorganisierten Monomere wurden, zusammen mit einem Templatpolymer (jedem Polymer, das bei niedrigen Temperaturen pyrolysiert werden kann) elektrogewoben. Das Erhitzen der Fasern auf Temperaturen über 460 °C führt zur Polykondensation der selbstorganisierten Monomere zu BBB mit gleichzeitigem Abbau und Entfernung des Templatpolymers. Eine strukturelle Charakterisierung, Morphologiestudien, sowie Untersuchungen der thermischen Stabilität und der mechanischen Eigenschaften wurden sowohl an Einzelfasern, als auch an Faserbündeln durchgeführt. Elektrogewobene BBB Nanofasern zeigten ausgezeichnete thermische Widerstandsfähigkeit mit einer *onset*-Abbauphase über 600 °C und 5 % Gewichtsverlust bei einer Temperatur von 640 °C unter N₂-Atmosphäre. BBB-Einzelfasern und BBB-Nanofaserverbunde wiesen einen E-Modul von 1.43 ± 0.26 GPa (226 nm Durchmesser) und 364.75 ± 4.76 MPa auf.

Darüber hinaus wurden BBB-Fasern zur Herstellung von dreidimensionalen,

Summary/Zusammenfassung

offenporigen, niederdichten ($\leq 13.9 \text{ mg cm}^{-3}$), kompressiblen (mehr als 90 % Erholung nach 50 %iger Kompression), intrinsisch flammenhemmenden und thermisch isolierenden (thermische Leitfähigkeit von $0.028\text{-}0.038 \text{ W m}^{-1}\text{K}^{-1}$) Schwämmen genutzt. Die Schwämme wurden durch Selbstorganisation von BBB Kurzfasern (50 – 500 μm Länge) in wässrigen Dispersionen durch gefriertrocknen erhalten. Die Nutzung eines wiederentfernbareren Klebstoffs (Poly(vinylalkohol)) wurde systematisch, zur Erhöhung der mechanischen Stabilität des Schwamms, untersucht.

Die elektrogewebene Kurzfaserverdispersion kann mit dem *wet-laid* Prozess zur Herstellung von porösen Membranen genutzt werden. In dieser Methode lieferten Vakuum-assistierte Filtration und Trocknung von Kurzfaserverdispersionen poröse Membranen durch Perkolation von Kurzfasern in Form eines zufällig angeordneten Fasernetzwerks. Die so hergestellten porösen BBB Membranen wiesen allerdings schlechte mechanische Eigenschaften auf (0.04 MPa). Daher wurden Kompositmembranen aus BBB und Schichtsilikaten (Na-Hectorit) untersucht. Die Kompositmembranen zeigten weder Brandverhalten unter Rauchentwicklung, noch Schmelztropfen. Diese Hec/BBB Membranen mit geringer Dichte zeigten große Ascherückstände von 80 – 94 %, niedrige Temperaturleitfähigkeiten von $28\text{ – }51 \text{ mW m}^{-1}\text{K}^{-1}$ und eine große Flamm-schutzeffektivität. Solche Membranen sind vielversprechende Materialien für Leichtbaukonstruktionsmaterialien und Schutzkleidung.

Elektrogewebene Membranen mit hierarchischer Porenstruktur und variabler Porengröße werden ausgiebig für Luft- (Schwebstofffilter [*high-efficiency particulate air*, HEPA], Hochleistungs-Schwebstofffilter [*ultra-low particulate air*, ULPA]) und Bakterienfilter verwendet. Als letzter Teil dieser Arbeit, wurde in einer Modellstudie ein neuer Aspekt von Partikelfiltration durch elektrogewebene, thermoplastische, poröse Membranen (TPU) zum ersten Mal untersucht, um flexible, ultra-leichte und stabile Polymer-Membranen mit erhöhten Gasbarriereigenschaften herzustellen. Das

Summary/Zusammenfassung

hohe Aspektverhältnis (≈ 20000) von delaminierten, in Schmelze synthetisierten Schichtsilikaten (Na-Hectorit) wurde durch Filtration in einer Polymermatrix als Barrierschicht zwischen zwei elektrogewebenen Membranen selbstorganisiert und anschließend schmelzgepresst, was zu erhöhten Gasbarriereeigenschaften führte. Eine hochgefüllte (> 25 wt.%) Hocheffizienz-Gasbarriere-Polymermembran mit perfekt ausgerichteten, synthetischen Hectoritplättchen mit hohem Aspektverhältnis und variabler Dicke (bis zu $5 \mu\text{m}$) konnte hergestellt werden. Der E-Modul konnte um bis zu einem Faktor von > 60 erhöht und die Sauerstoffpermeabilität um 98.8% reduziert werden, im Vergleich zum reinen TPU. Das elektrogewebene Membranpolymer wird zukünftig variiert, einschließlich der Verwendung von BBB, um die Materialeigenschaften mit denen von Schichtsilikaten zur Herstellung von Hochleistungsmembranen zu kombinieren.

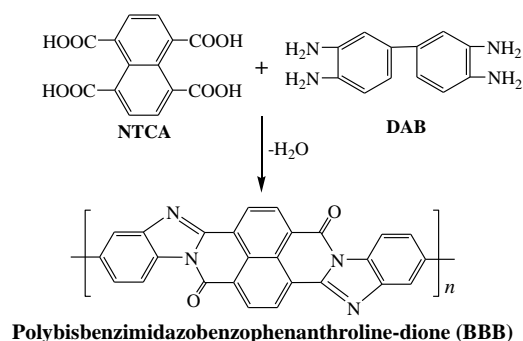
Die Ergebnisse wurden in, durch *peer-review* geprüften, Journalen publiziert: *Nanoscale*, **2017**, 9(46), 18169-18174; *Macromol. Mater. Eng.*, **2018**, 303(4), 1700615; *ACS Appl. Mater. Interfaces*, **2019**, 11(12), 11876-11883; *Macromol. Mater. Eng.*, **2019**, 1800779.

1 Introduction

1 Introduction

1.1 Motivation and Aim

Poly(bisbenzimidazobenzophenanthroline-dione) (BBB) (**Scheme 1** for the structure) is a typical example of a ladder-type rigid-rod polymer with a lot of aromatic and heterocyclic rings in the backbone that makes it a robust thermal and chemical-resistant material. The outstanding thermal resistance property of BBB is evident from no weight loss up to 600 °C in an inert atmosphere or vacuum, no softening temperatures up to 425 °C and less than 10 % weight loss at 315 °C after 1500 h in air. These special properties make BBB promising for application in the field of heat- or flame-resistant materials, such as high-performance textiles (firefighters' clothing or gloves). As early as in the middle of the last century, BBB was synthesized in the Air Force Materials Laboratory (US) by the polycondensation of 1,4,5,8-naphthalene tetracarboxylic acid (NTCA) and 3,3'-diaminobenzidine (DAB) in polyphosphoric acid at a high temperature (~200 °C). Their intrinsic insolubility in common organic solvents and infusibility has hindered the establishment of an effective way of processing BBB to fibres and films and, therefore, has been a bottleneck for its use. There has not been a major breakthrough in the processing of BBB fibres since the 1960s. Therefore, special procedures are required for the processing of BBB regarding its utility for high-performance applications.



Scheme 1. Synthetic scheme and chemical structure of BBB.

Therefore, the overall aim of the present work is to study the processing methods for BBB and the mechanical, thermal and flame-retardant properties of corresponding BBB fibres, sponges and composite membranes with layered silicate.

1 Introduction

Due to the otherwise non-processability of BBB, a bottom-up approach was considered for study in this work in which solid-state high-temperature polymerization of self-assembled monomers for BBB is carried out on a sacrificial template fibre. Electrospinning was used as the method to process the fibre. Furthermore, short BBB fibres were used for making sponges and composite membranes with layered silicate by the self-assembly of fibres from a dispersion during freeze-drying (FD) and wet-laid methods, respectively. The literature overview is provided in the subsequent sections about relevant topics.

1.2 Electrospinning

Electrostatic fibre formation, also known as “electrospinning,” has risen in the last two decades as a popular choice for producing continuous fibres, fibre arrays and nonwoven fabrics with fibre diameters below 1 μm from a wide range of materials for different applications.^[1-3] Electrospinning provides easy access to polymer, inorganic, metal and ceramic nanofibres with specific topologies. Electrospinning also allows the functionalization of the nanofibres during the preparation or post-treatment by incorporating features such as viruses, bacteria, enzymes, drugs and catalysts.^[3] The development of the electrospinning technique has experienced a long history. At first, the shape change phenomenon of liquid (water droplet) in the presence of an electric field was observed.^[2] About one century later, the electrospaying experiment of water droplet to aerosol and the theory were studied systematically.^[2] When the liquids change to viscous and viscoelastic polymer solutions, the charged jet can be kept in a continuous form to produce fibres instead of breaking into small size droplets, such as in electrospaying. This is the start of the electrospinning. Some important patents regarding the designing of the setup and equipment for electrospinning were filed in the early 20th century.^[4-6] Subsequently, the mechanistic understanding of electrospinning was gradually developed. Geoffrey Taylor has to be mentioned regarding the mechanics: He described the model where the spherical droplet would

1 Introduction

gradually evolve into a cone (now commonly referred to as the Taylor cone) and produce a liquid jet on increase in the electric field beyond a critical level.^[7-9] After twenty years of stagnancy, the development of a nanoscale size (electron microscopes) measurement technique moves toward the making the electrospinning technique prosperous. Many organic polymers electrospun into nanofibres were reported in the 1990s and this re-invented technique eventually developed into the first choice for producing long and continuous fibres with diameters down to the nanometre scale.^[10-13] At the beginning of the 21st century, electrospinning started to attract increasing attention because of its capability of expanding, leading to the fabrication of new composite materials and ceramic nanofibres with controllable structures, such as core-sheath and hollow nanofibres.^[14-16] At the same time as the emergence of new structures, new applications of electrospun nanofibres were rapidly expanded to catalysis,^[17] energy harvesting, conversion and storage (e.g. lithium battery, supercapacitor, dye-sensitized solar cells),^[18] as well as biomedical applications, including wound dressing,^[19] drug release^[20] and tissue-engineering,^[21] not only limited to initial water or air filtration.^[22,23] Nowadays, electrospinning products in large volumes from industrial lines have been designed and implemented by a number of companies, enabling downstream commercial products widely used in water and air filtration and the biomedical area.

1.2.1 Device and Principle of Electrospinning

The important components parts of an electrospinning machine are a high-voltage power supply, a syringe pump to feed the solution, a spinneret (could be a hypodermic needle with a blunt tip), and a collector connection with a negative electrode or ground, as illustrated in **Figure 1-1a**. A pendant droplet forms when the liquid (polymer solution or melt) is extruded from the spinneret as the result of surface tension. When the droplet is in the electric field, the electrostatic repulsion among the surface charges deforms the droplet into a Taylor cone,^[24,25] and a charged jet is then ejected from the cone. The fibre formation from the liquid droplet takes place in four

1 Introduction

steps. The first step is the formation of the Taylor cone, a cone-shaped jet. This is followed by the extension of the jet along a straight line. Subsequently, thinning of the jet occurs in the presence of an electric field leading to electrical bending instability (whipping instability). At the end, the fibres are solidified and collected on a collector which can be stationary or rotating.^[2,22,26,27]

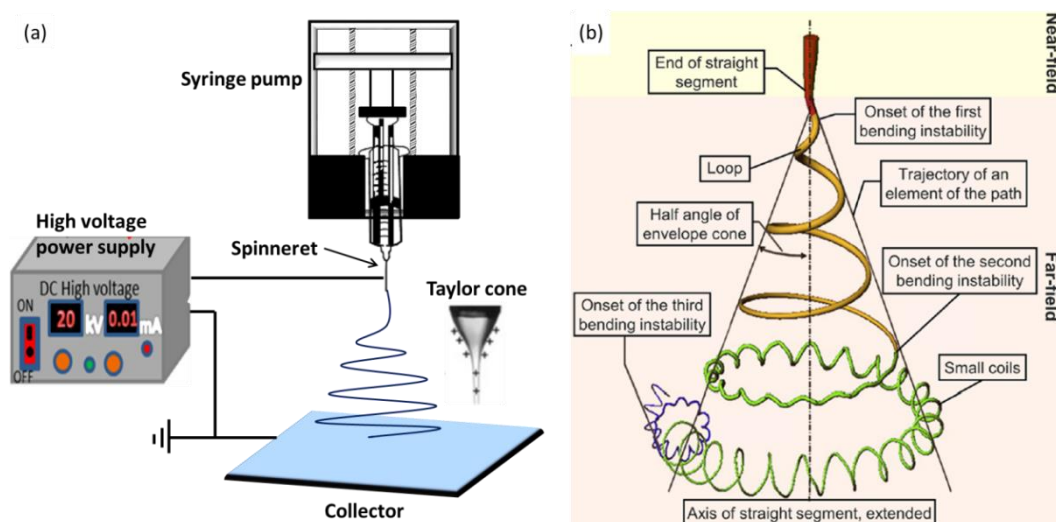


Figure 1-1. (a) Basic device for electrospinning. (b) Diagram showing the path of an electrospun jet. (b) Reprinted with permission from ref 2. Copyright (2019) American Chemical Society.

Figure 1-1b illustrates the process of the formation of an electrospun fibre. The mechanism has become by now a common knowledge and described in several literatures.^[2,11,28] In the first step, with the gradual increase of voltage, more charges are accumulated on the surface of the droplet, increasing of the density of the charges. While the electric field force on the droplet surface is higher than a critical value (surface tension plus the viscoelastic force), electrostatic repulsion deforms the droplet's shape resulting into increased surface area.^[28] The critical voltage needed to generate a conical shape for the droplet depends on the intrinsic properties of the liquid, such as viscosity and conductivity. In the second step, the tapered jet initially follows a nearly straight line for a certain distance away from the tip of the spinneret. Viscoelastic properties of the polymer solution play an important role in getting fibres by suppressing the Rayleigh instability, which otherwise will break the jet into

1 Introduction

droplets.^[28-30] The velocity of the jet at the end of the straight segment is about 1–15 m s⁻¹. The diameter of the jet in the straight part decreases monotonically with the distance away from the cone, as the jet is continuously stretched.^[31] When the jet enters the far-field region in the third step, instability occurs easily as the consequence of the electrostatic repulsion on the surface charges accumulated on the jet. There might be three different types of instability (**Figure 1-1b**) which occur to the electrically charged jet, including two kinds of axisymmetric (Rayleigh instability and another occurs at a stronger electric field) and one non-axisymmetric instability (known as whipping or bending instability).^[11,12,28,32] The physicochemical properties of the liquid and the parameters during electrospinning control the interaction between the charged jet and the external electric field and further coordinate these three different types of instability. With the driving of whipping and bending, the jet moves towards the collector where the trajectory evolves into a series of loops, generating a tapered coil with many turns. The coil consists of one continuous, looping, spiralling and gradually thinning jet moving at high velocity. Later, as shown in **Figure 1-1b**, the jet further elongates to a thinner diameter and generates a much smaller coil, triggering the formation of another stage of bending instability, the second bending instability. During the elongation process, the solidification takes place simultaneously caused by either the evaporation of solvent or the cooling of melt, which finally accomplishes the formation of the fibre. The solidified fibres are deposited on the ground-connected conductive collector and most of the static charges dissipate. With the increase of the fibre deposition, more residual charges will remain on the surface of the fibres collected, which tends to repress the similarly charged fibres, and result in limiting the achievable thickness of the nonwoven mat.^[33-35]

Most of the early reports relate to traditional electrospinning which uses a single needle and the nanofibres are produced at a relatively low output as the flow rate is generally 0.5–5.0 mL/h. In order to increase the productivity, several efforts are documented in the literature including the use of multiple-needles for electrospinning

1 Introduction

as shown in **Figure 1-2a**. There could be different arrangements of the multiple needles, i.e. a linear (straight line) or a two-dimensional array.^[36,37] The production capacity of electrospun fibres is increased to $\sim 2000 \text{ m}^2$ per day as shown for (polyimide (PI)) for lithium-ion battery separators and high-temperature filters (**Figure 1-2b**).^[38] Meanwhile, in order to pursue new structures and functions of the resultant nanofibres, coaxial electrospinning was developed by using a cone-shell or triaxial nozzles (**Figure 1-2c**).^[39,40] On the other hand, needleless spinnerets were designed to increase the number of jets and create multiple jets to replace the needle array.^[2,41-44] Some typical examples of needleless spinnerets evolving a bowl with a curved edge,^[41] a jagged metallic plate (**Figure 1-2d**),^[42] a stepped pyramid (**Figure 1-2e**),^[43] and a variety of different rotary metal cylinders, discs and balls^[44] have all been explored (**Figure 1-2f**).

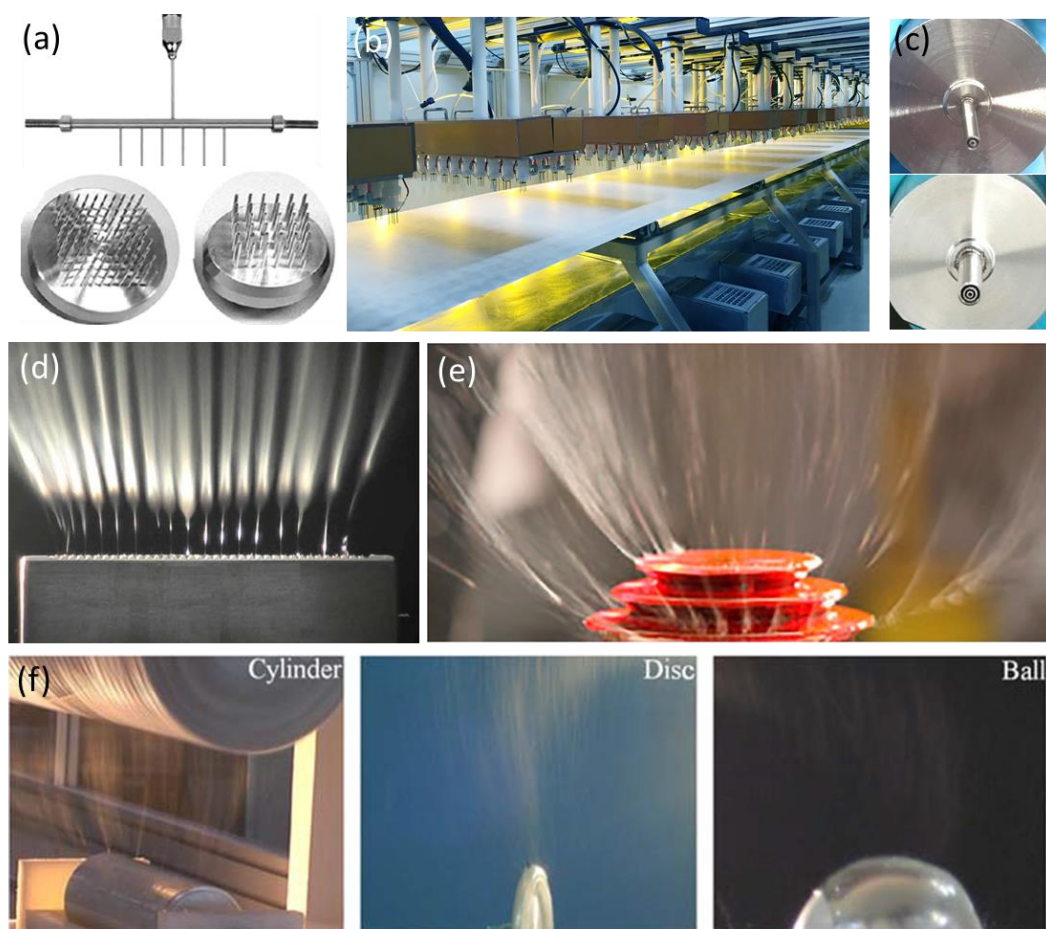


Figure 1-2. (a) Examples of nozzles for multiple-needle electrospinning. (b) Industrial production line of multiple-needle electrospinning of PI nanofibrous mats/nonwovens (from Jiangxi

1 Introduction

Advanced Nanofibre Technology Co.). (c) Examples of coaxial nozzles. (d) Photographs of electrospinning processes that use a jagged metallic plate and (e) a stepped pyramid as a spinneret. (f) Photographs of electrospinning processes using a rotary metal cylinder, disc and ball as a spinneret. (a) Adapted with permission from ref 37. Copyright 2018 Wiley-VCH. (d) Reprinted with permission from ref 42. Copyright 2008 AIP Publishing. (e) Reprinted with permission from ref 43. Copyright 2015 Elsevier. (f) Reprinted with permission from ref 44. Copyright 2012 Taylor & Francis.

1.2.2 Materials for Electrospinning

High molecular weight polymers are the most common materials for electrospinning. Small molecular weight compounds can also be directly electrospun into nanofibres in some cases if they self-assemble to liquid crystal or generate sufficient chain entanglement.^[45,46] Inorganic nanoparticles, nanorods, nanowires, nanotubes and nanosheets also can assemble to nanofibres by electrospinning with the assistance of organic polymers. In the past thirty years, several different kinds of organic polymers, both natural and synthetic polymers, have been electrospun. Depending upon their solubility and fusibility, different modified electrospinning procedures are developed, such as solution, emulsion and melt electrospinning.

Solution electrospinning is the one highly used and studied method as several organic polymers are soluble in one or the other solvents. In fact, nearly all known synthetic and natural polymers (DNA, silk fibroin, fibrinogens, dextran, chitin, chitosan, alginate, collagen, gelatin and gum), either soluble or fusible have been electrospun and related parameters affecting electrospinning and applications, such as air and liquid filtration, battery separator, electrodes, textiles, biomedical etc. are studied. Meanwhile, a large number of biocompatible and biodegradable synthetic polymers, for example, polycaprolactone, poly(lactic acid) (PLA), and poly(lactic-co-glycolic acid), have been directly electrospun into nanofibres and further explored the applications in biomedical directions.^[47-49] Conductive and functional polymers, such

1 Introduction

as polyaniline^[50], polypyrrole,^[51] poly(vinylidene fluoride)^[52] have been directly electrospun into nanofibres. Most common organic solvents used for electrospinning are tetrahydrofuran, dichloromethane, chloroform, dimethylformamide, dimethylacetamide, acetic acid, acetone, dimethyl sulfoxide, hexafluoroisopropanol, and trifluoroethanol. The volatility or vapour pressure determines the evaporation rate of the solvent and, thus, the solidification rate of the fibres. Neither very high nor very low volatility is suitable for electrospinning. Very often, a mixture of different solvents is used. High dielectric constant solvents, like water is not always the first choice due to the attenuation of electrostatic repulsion making spinning process unstable.

Both the intrinsic properties of the polymer solution and the processing parameters control the formation of fibres and their morphology and properties. Viscosity and conductivity are important parameters affecting spinning process. These parameters depend upon the polymer and solvent used for spinning. The polymer molecular weight and the solid content (concentration) are the main factors effecting the viscosity, which plays a critical role in stretching the jet.^[53] Low polymer solution viscosity leads to only particle formation (also called electrospraying) and if viscosity is very high, the ejection of the solution from spinning nozzle is hindered. Also, electrical conductivity should be optimum for electrospinning.^[54] A polymer solution which is perfectly insulating is difficult to electrospinning as it is unable to conduct charges from the interior to the surface, for example, PLA dissolved in chloroform. Therefore, ionic compounds, such as salts or mineral acids are added to the spinning formulations for increasing the conductivity and hence improves the spinning process.^[55] Applied voltage, polymer solution flow rate, the distance between the electrodes (spinning nozzle) and the collector, humidity and temperature are other important factors influencing the process of spinning, morphology and size of the fibres.

Blend electrospinning, by mixing another electrospinnable polymer which serves as a

1 Introduction

carrier phase or template, is an efficient way to obtain the functional fibres for some polymers with a small molecular weight or natural polymers with special functions which are of great potential application in the form of nanofibres but might not be suitable for electrospinning.^[56,57]

Melt electrospinning is useful for commercial thermoplastic polymers which are otherwise difficult to dissolve in organic solvents at room temperature making their solution spinning either impossible or difficult. An extra heating device keeps the polymer in a molten state during melt spinning.^[58-60] The fast heat transfer between the jets and the surrounding air solidifies the spinning jets to fibres. The stretching degree and the obtained fibre diameter are very much different in solution and melt electrospinning. The melt electrospun fibres are much thicker (more than 1 micrometre, whereas solution electrospun fibres are in the range 100-300 nm or even smaller possible). This is due to the low electric conductivity and high viscosity of the polymer melt making a low-density of the surface charges on the jets but high surface tension. Thereby, whipping instability is not effective. Adding viscosity-reducing additives or inorganic salt (such as NaCl) could effectively decrease the diameter of the melt electrospinning fibre.^[61] Until now, many common industrial polymers matching the condition of melt electrospinning (have a glass transition and melt at a temperature without involving thermal degradation) have been explored, including polyethylene, thermoplastic polyurethane (TPU), polycaprolactone, PLA, polypropylene nylon-6, poly(methyl methacrylate) and poly(ethylene terephthalate) (PET).^[58]

Emulsion dispersion consisting of liquid particles and a continuous medium phase (normally water) is always hard to electrospun directly but can be made spinnable by adding a water-soluble polymer, such as polyethylene oxide (PEO), poly(vinyl alcohol) (PVA) or poly(vinyl pyrrolidone) (PVP). A typical example is the fabrication of poly(terafluoro ethylene) fibres by emulsion electrospinning.^[62] Electrospinning of colloidal particle dispersion is also possible when there is a sufficient particle

1 Introduction

entanglement which is required to maintain the jet as a continuous structure. One of the examples is the formation of silica nanofibres by electrospinning aged sol prepared from tetraethyl orthosilicate, distilled water, ethanol and HCl.^[63] Other examples based on sol electrospinning include the fabrication of ceramic fibres made of metal oxides, such as Co_3O_4 , LiGoO_2 and NiO , and a mixture of Al_2O_3 and ZnO has been reported, by using their precursor solutions as electrospinning liquid. However, the sol-gel method of electrospinning is always limited because of the difficulty in accurately controlling the rheological properties of the sol. Sometimes additive carrier polymer is needed to improve the viscosity or conductivity of the dispersion and is, subsequently, removed by calcination.^[64] A carrier polymer plus precursor solution electrospinning system is a convenient way to fabricate inorganic ceramic nanofibres, metallic nanofibres, carbon nanofibres and their hybrid nanofibres. Nanoparticles, including nanospheres, nanotubes, nanorods and two-dimensional graphene, clay and MXene, are usual fillers for enhancing or endowing additional properties to electrospun nanofibres. Two main strategies, direct incorporation during spinning and post-treatment of the precursor fibres, have been adopted to incorporate nanoparticles into electrospun nanofibres.

1.2.3 Morphology and Structure of Electrospun Fibres

Electrospinning technique in combination with post-treatment enable the preparation of nanofibres with diverse morphologies, which were summarized by Hou and co-workers.^[65] A simple cylindrical fibre with a smooth surface, as show in **Figure 1-3a**, is the most representative and common structure produced by electrospinning.^[10] In addition to the cylinder-shaped nanofibres, there are two other structures that are frequently obtained by electrospinning: Ribbon-like oblate fibre (**Figure 1-3b**) and periodic bead-on-string structure fibre (**Figure 1-3c**).^[66,67] These three basic structures are the results of the balance of intrinsic viscoelasticity of the polymer solution and Rayleigh instability aroused from the external electrical field. Periodic bead-on-string

1 Introduction

fibres are obtained, in most cases, when spun from diluted solution with a low viscosity. Increasing the concentration of the solution will change the beads from spherical to spindle-like morphology, decrease the density of beads and, eventually, the beads will disappear when the concentration rises to a critical value.^[10] On the other hand, the introduction of a small amount of salt which increases the conductivity would avoid the formation of beads in some cases. If the electrospinning is carried out by using a high volatility solvent, the surface of the resulting fibres tend to be porous (**Figure 1-3d**).^[68] A typical example of porous fibres is the fabrication of PLA fibre with dichloromethane or chloroform as the solvent and polystyrene fibres from tetrahydrofuran. The surface porosity is attributed mainly to the phase separation induced from the rapid evaporation of the solvent and a subsequent rapid solidification. The humidity of the surrounding air, the evaporation rate of the solvent is an important parameter effect, is also one of the main factors for the formation of pores with nanoscales.^[69] When the solvent has high volatility, the temperature at the surface of the jet is rapidly decreased with the evaporation of solvent, resulting in the condensation of the surrounding water vapour into tiny water droplets at the surface or penetrating into the jet.^[2,70] The pores form after the water droplets and solvent are removed completely. When pores are introduced into the nanofibres, the specific surface area of the resultant nanofibre-based mat will be drastically increased.^[2,71]

The electrospinning technique could also be used flexibly to fabricate heterogeneous nanofibres by a direct or indirect route, such as side-by-side fibre from a juxtaposed spinneret (**Figure 1-3e**) and pine branch-like fibre structures (**Figure 1-3f**) from the post-treatment of deposited heterogeneous materials on the surface of electrospun nanofibre substrate.^[72-73]

Electrospinning is also a technique that can generate nanofibres with complex inner structures, including core/sheath, hollow and more complex structures, as show in **Figure 1-3g-i**.^[16,74-76] Adoption of a coaxial nozzle, as present on **Figure 1-2c**, is one one-step direct route to access core/sheath fibre structure combining two or more

1 Introduction

different components. It should be mentioned here that sometimes one of the components cannot be electrospun into fibres directly but obtains the composite fibres smoothly by coaxial electrospinning with the assistance of another spinnable polymer. Expand the materials of choice is a benefit of coaxial electrospinning, especially for some small molecular weight compounds with special functions which cannot electrospun into fibres by themselves. Based on the routine coaxial electrospinning method, many further developments of electrospinning have emerged recently, such as multi-fluidic compound-jet electrospinning and multi-fluidic coaxial electrospinning. Core, hollow or heterogeneous wire-in-tube structured fibres have been prepared. On the other hand, post-treatment with the chemical deposition method is also adapted to fabricate hollow nanotubes with the electrospun fibres as the substrate (**Figure 1-3j**).^[77] Ultra-porous nanofibres and pea-like hollow fibres were fabricated by electrospinning heterogeneous liquid, followed by the removal of the sacrificial phase by calcination and pyrolysis (**Figure 1-3k-l**).^[78,79]

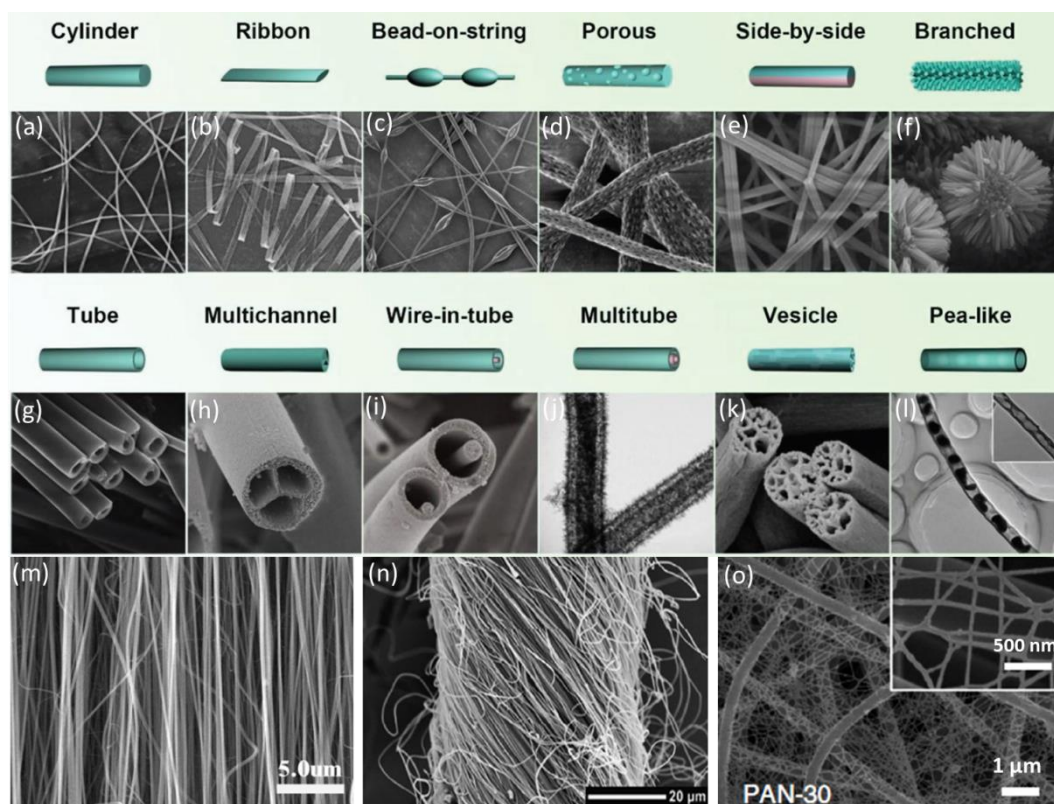


Figure 1-3. Micro/nanofibres with multi-structures obtained by the electrospinning technique: (a) Cylinder, (b) flattened ribbon, (c) bead-on-string, (d) surface porous, (e) side-by-side, (f) branched,

1 Introduction

(g) tube structure, (h) multichannel, (i) wire-in-tube, (j) multiwall, (k) vesicle, (l) pea-like, (m) aligned nanofibre belt, (n) nanofibre yarn and (o) nanoarchitecture networks. (a)-(l) Reprinted with permission from ref 65. Copyright 2018 Wiley-VCH. (m) Reprinted with permission from ref 80. Copyright 2008 IOP Publishing. (n) Reprinted with permission from ref 81. Copyright 2012 Taylor & Francis. (o) Reprinted with permission from ref 82. Copyright 2019 Springer Nature.

The macroscopical arrangement of fibres is determined by the type of the collector. With the exception of the traditional random fibre arranged in a nonwoven manner obtained from a flat, stationary collector, other architectures, such as fibre-aligned belts (**Figure 1-3m**) and twisted nanofibre yarn (**Figure 1-3n**), could be fabricated by using a high-speed rotated disc and rotary funnel as a collector, respectively.^[80,81] In addition, nanoarchitecture networks (**Figure 1-3o**) were prepared by electrospinning extremely diluted solutions with a polyacrylonitrile fibre membrane as a collector.^[82]

1.2.4 Application of Electrospun Nanofibres

An electrospun nanofibre mat, self-standing or coated on the substrate possesses a large surface-to-volume ratio and high porosity, making it useful as a filter for various purposes. The high porosity allows the gas steam and solution transport through the membrane in high flux without experiencing much resistance. Moreover, the pore size of the nanofibre-based mat could be adjusted conveniently by changing the diameter and the surface functionalization is achieved by post-spinning modifications. These mats have been extensively explored as advance filters for the removal or absorption of pollutants, such as particulate matters, toxic ions and organic molecules from both air^[83-87] and wastewater.^[88-91] On the other hand, electrospinning combined with post-treatment is a versatile approach to achieve superhydrophobic fabrics with self-cleaning properties from a variety of materials for water/oil separation.^[92-94]

Regarding the energy field, continuous carbon nanofibres from electrospinning, characterised by a high surface-to-volume ratio, large specific surface area and short diffusion distance, have notably shown great promise as electrode materials for

1 Introduction

advanced batteries and supercapacitors.^[95-101] Porous electrospun fibre mats made of thermal stable polymer, such as PI and PET, have attracted increased attention as safe battery separators, particularly in high-temperature conditions.^[38,73,102] The use of electrospun porous semiconductors (e.g. TiO₂) nanofibres, coated with a photo-active substance, such as the photoanode, is an effective way to improve the power conversion efficiency of solar cells.^[103-105] Electrospinning has recently been adopted for the design of solar desalination devices.^[106,107]

Electrospun polymer or ceramic nanofibres containing catalytic nanoparticles (such as Pt, Au nanoparticles and enzymes) also have great advantages in heterogeneous catalysts system.^[108-110] Large surface area-to-volume ratio, high porosity, uniformity in fibre size, diversity in composition, flexibility in assembled structure and ease of functionalization with bioactive molecules make electrospun nanofibre-based scaffolds promising candidates as carriers for drug delivery^[111-113] and scaffolds for regenerative medicine.^[114-117]

1.3 Electrospun Conjugated Rigid-Rod Polymers

1.3.1 Development of Rigid-Rod Polymers

High-performance synthetic polymer materials, called special engineering plastics, with outstanding mechanical, thermal and electric properties, combined with a lightweight and chemical resistant, have attracted a lot of interest and achieved huge progress since the middle of the last century. High-strength, high modulus and high-temperature-resistant polymeric fabric material is one of the most important and developed special engineering plastics both in theoretic research and commercialization. Good examples of commercialized high-performance fabric materials include flexible polymer-based ultra-high molecular weight polyethylene, PET, and aromatic polyamides (Kevlar[®] and Nomex[®]) and PIs containing rod-like macromolecular chains. In order to pursue higher temperature resistance satisfying the requirement in military and aerospace engineering, more rigid-rod polymers

1 Introduction

containing a conjugated aromatic heterocyclic ring in the backbone were developed and commercialized, such as polybenzimidazole (PBI), poly(p-phenylene benzobisthiazole), poly(p-phenylene benzobisoxazole) (PBO) and poly(pyridobisimidazole).^[118,119] The tensile strength of commercialized PBO (Zylon HM) and poly(pyridobisimidazole) (M5) fibres reach 5.8 and 3.5 GPa, respectively, and the tensile modulus reaches 270 and 330 GPa, respectively.^[120] Both the strength and the modulus are much higher than steel but have smaller densities. This kind of conjugated polymer also shows good flame-resistance properties, for example, PBO shows the highest limiting oxygen index of 68 vol%.^[121] These polymers containing aromatic or heterocyclic rings combine with many chemical factors, such as strong primary and van der Waals bonding forces, hydrogen bonding, resonance stabilization, molecular symmetry or cross-linking promoted from modified groups, making them robust materials with a combination of thermal stability and physical properties. The polymers with high-temperature resistance provide wide potential applications for uses in electronics, aircraft and aerospace vehicles, engine components, engineering structures, heat-resistant coatings, molecular composites and other high-performance technological applications.^[120]

Another type of high-performance polymer is the ladder and semi-ladder type polymers first reported by the Air Force Materials Laboratory.^[122] Two of the noteworthy examples are the BBB and poly(benzobisimidazobenzophenanthroline) (BBL), which were prepared by the polycondensation of either 3,3',4,4'-tetraaminobenzidine (DAB) or 1,2,4,5-tetraaminobenzene (TAB) with 1,4,5,8-naphthalene tetracarboxylic acid (NTCA) in polyphosphoric acid at a high temperature (180-190 °C) (**Figure 1-4a -b**). Polymerization of NTCA and DAB in solid phase lead to low molecular weight which is soluble in sulfuric acid.^[123] They were first synthesized in an effort to develop polymers with a very high strength and high-temperature resistance for use as structural materials in aerospace applications. Both of these polymers are thermally stable (i.e. exhibit no weight loss) to 550 °C in

1 Introduction

air and 700 °C in nitrogen.^[122,123] Thermal-mechanical and creep studies in the range of 30–500 °C indicated that this rigid molecule structure is relatively insensitive to temperature and no glass or other transition was evident in this temperature range.^[124,125] Different to other rod-like structure polymers, such as poly(p-phenylene benzobisthiazole) revealing as liquid-crystalline in solution, BBB molecules containing a rotatable single bond link in the backbone between each repeat unit give it a flexible-coil behaviour. The same helical structure arrangement (**Figure 1-4c**) is also observed on BBB film.^[126]

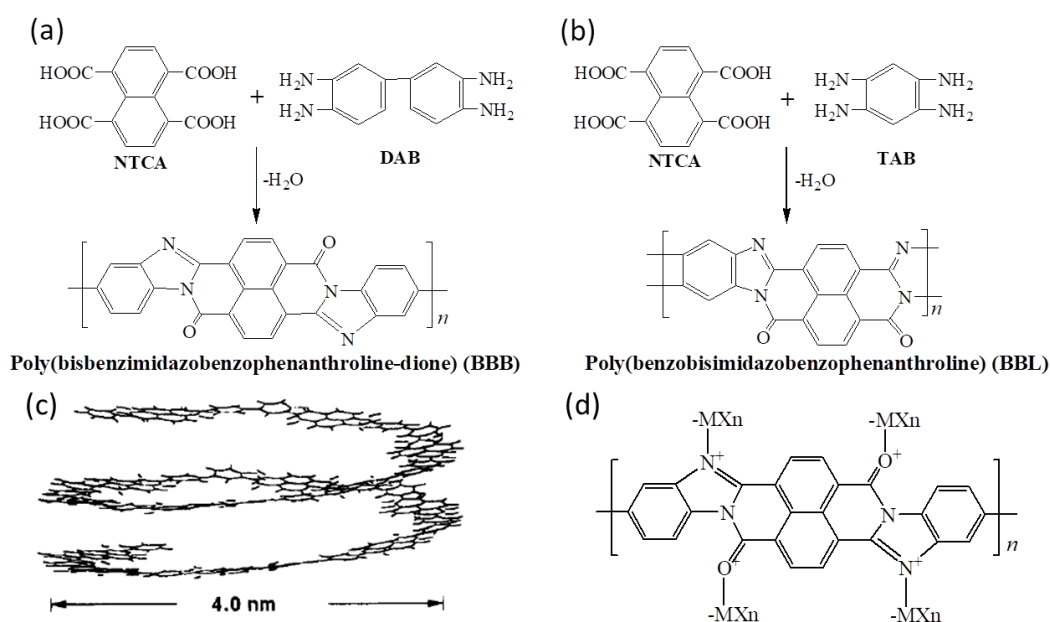


Figure 1-4. (a, b) Synthetic and chemical structures of (a) BBB and (b) BBL polymers. (c) Helical arrangement of BBB molecules. (d) Structures of the soluble Lewis acid (MX_n) complexes of BBB polymer. (c) Reprinted with permission from ref 126. Copyright (1995) American Chemical Society. (d) Adapted with permission from ref 129. Copyright (1990) American Chemical Society.

Rigid-rod structures, which endow great thermal and mechanical properties, unfortunately, simultaneously cause processing difficulties due to insolubility in organic solvents and the glass transition temperature and melting point of these materials is above their decomposition temperatures. Processing rigid-rod polymers into fibres or films is always carried out by dissolving in strong protonic acids.^[126]

1 Introduction

Take BBB as an example: BBB film is prepared by evaporation to dryness from methane sulfonic acid (MSA) solution or slow coagulation of a solution of BBB in MSA by the action of water absorbed from moist air.^[124,125] BBB fibres were prepared by the dry-jet wet-spin process. However, the processing based on ultra-strong protonic acid solutions brings serious problems, such as a high demand for equipment and environmental contamination. Two common strategies have been adapted to enhance the solubility and processing of rigid-rod polymers. Firstly, modification of the basic rigid-chain structures by the introduction of flexibilizing linkages (e.g. -O-, -CO-, -CH₂-, -SO₂-) or molecular asymmetry (ortho, meta, versus para linkages) into the backbone or the addition of bulky side groups (e.g. -SO₃H) to improve solubility.^[127,128] The major disadvantage of this strategy is that processability is achieved at the expense of thermal stability, chemical resistance or mechanical properties. Secondly, a two-s synthetic route including processing a soluble intermediate or precursor polymer and subsequent conversion to the rigid-chain structure by using a thermally activated cyclization was designed. This approach is typically exemplified in the commercial processing of PIs via soluble polyamic acid precursor.^[38] One important approach which has to be mentioned is the use of metal halide Lewis acids as the cosolvent to promote the dissolution of rigid-rod polymer in aprotic organic solvents and the subsequent conventional solution processing.^[129] During the dissolution process, a reversible electron donor-acceptor complex was formed between heterocyclic polymers and Lewis acids in aprotic organic solvents. This reversible electron donor-acceptor complex arises from a Lewis acid base reaction at specific heteroatom nonbonded electron pair donor sites (N, S, O) on the polymer chains rather than from a π -electron charge-transfer reaction (**Figure 1-4d**).^[129] The resultant solutions of rigid-rod polymer can be processed into films, fibres and coatings, as well as purification. In another attempt at processing BBL polymer, hydrophilic functional groups of a short PEO chain were grafted into the ends of BBL molecule chains enabling the formation of homogenous dispersion of

1 Introduction

BBL-PEO in water.^[130,131] The formation of BBL films was successful from BBL-PEO water dispersion via an air flow-assisted spraying process and the electrochemical and photocurrent generation properties of the resultant films were studied.^[131] Both BBB and BBL exhibit a third-order nonlinear optical coefficient.^[132] It has been observed that both pristine BBB and BBL are insulators with the electron conductivity of 10^{-14} - 10^{-12} S cm⁻¹ at room temperature.^[133] However, the typical large delocalized conjugated electron structures indicate that BBB and BBL are capable of being conductivity polymers. One side, increasing the temperature, the conductivity of them trends to increasing both reveals from the film and fibres.^[134-136] On the other hand, protonated doping is an efficient way to increase conductivity, for example, protonic acid (H₂SO₄) doped BBL and BBB films were found to be highly conductive (2 S cm⁻¹).^[137] However, this type of protonated doping is unstable. In one report, the same conductivity of 2 S cm⁻¹ was achieved by BBB and BBL doped with poly(styrenesulfonic acid) and showed good ambient air stability even to a temperature of 100 °C. The conducting BBL/ and BBB/poly(styrenesulfonic acid) complexes may be useful for the fabrication of photovoltaic cells and light-emitting diodes.^[133]

A recent interest in BBB and BBL focused on their intrinsic semiconducting properties and relative applications. Both BBL and BBB have an identical optical band gap ($E_g = 1.8$ eV) and absorption spectra, electron affinity (EA = ca. 4.0-4.4 eV) and redox properties, and dc conductivity when chemically doped.^[138] The major difference between the two polymers is that BBL films spin-coated or cast from MSA solutions are semi-crystalline, whereas BBB films are completely amorphous, which was revealed by X-ray and electron diffraction.^[139,140] The field-effect mobility of electrons is several orders of magnitude enhanced in BBL (0.03 cm² V⁻¹ s⁻¹) with a ladder architecture compared to semi-ladder conjugated polymer BBB (10^{-6} cm² V⁻¹ s⁻¹) observed from field-effect transistors.^[138] The BBL nanobelts, prepared via precipitating BBL/MSA solution on environmentally benign solvents, such as

1 Introduction

methanol and water, were also used to construct field-effect transistors that exhibited electron mobility up to $\sim 7 \times 10^{-3} \text{ cm}^2 \text{ V}^{-1} \text{ s}^{-1}$.^[141] One more example is given by the thin film transistors fabricated from an n-channel BBL transistor and a p-channel poly(3-hexylthiophene) transistor. The electrical parameters (electron mobility, on/off current ratio and threshold voltage) of the n-channel BBL transistors in air were found to be constant over the four years.^[142] Solar cells made from spin-coated bilayer thin-film heterojunctions of poly(*p*-phenylene vinylene) and BBL were found to have a photovoltaic charge collection efficiency as high as 49 % and maximum power conversion efficiency reached 2.0 % under sunlight illumination.^[143]

1.3.2 Electrospinning of Rigid-Rod Polymers

Electrospinning is the most effective state-of-the-art method for the generation of continuous polymer nanofibres with extensive materials, such as polymers, ceramics, metals and metal oxide, carbon nanotubes, and even bacteria and viruses, as described in 1.2.2. The mechanical properties of most electrospun polymer nanofibres are generally not comparable with conventional microfibrils manufactured by melt-spinning. However, the fibres with a diameter less than 1 μm reveal some particular performances, such as a huge surface area to volume ratio, large porosity, high aspect ratio of length to diameter and easy-tailored nanofibre products, which usually arouse more feasible applications (see 1.2.4). Examples of high-strength electrospun nanofibre have been reported, including PI nanofibre belts of 1.1 GPa^[80] and single polyacrylonitrile nanofibre of 1.75 GPa^[144]. It is conceivable that nanoscale rigid-rod fibres produced with outstanding mechanical and thermal properties are a good candidate for filtration in a harsh environment or as a filler for the enhancement of mechanical and thermal properties in composites. In one recent piece of research, an electrospun PBI nanofibre membrane demonstrated a higher surface potential than other commercially available mask filters because of its high dipole moment (6.12).^[145] The filter developed with PBI nanofibres provided a high particulate matter filtering efficiency of $\sim 98.5\%$ but only a small drop in pressure. Furthermore, this PBI membrane demonstrated negligible damage and

1 Introduction

retained its original performance for reuse after several cycles of cleaning.

However, processing of other rigid-rod polymers by electrospinning are confronted with more challenges because of their poor solubility in common solvents and degradation temperature below their melting points. Traditionally, dry jet-wet spinning of these rigid-rod polymers is commonly carried out based on the solutions of extremely strong acid.^[120] Kevlar, for example, is dissolved in concentrated sulfuric acid (98–100 %), PBO and poly(pyridobisimidazole) in polyphosphoric acid. Direct electrospinning of these strong acid-based systems placed higher requirements on the electrospinning equipment and the parameter control due to the involatile and strong causticity of the solvent. A water bath, for example, was adopted as the collector and for extracting the solvent when electrospinning 2–3 wt% Kevlar solution in a solvent of 95–98 % sulfuric acid.^[146] Nanofibres with a diameter ranging from 40 nm to hundreds of nanometres were produced successfully and molecular orientation was investigated, but some important issues, such as the mechanical properties, were missing. Another study of electrospinning highly concentrated Kevlar solution in 98 wt% sulfuric acid gave micrometre size fibres with a diameter in the range of 2.1–15.8 μm .^[147] The maximum Young's modulus and tensile strength of 59 and 1.1 GPa, respectively, were found at a diameter of 2.1 μm . Meta-aramid (Nomex) can dissolve in common organic solvent, such as dimethylformamide, dimethylacetamide and dimethyl sulfoxide, in the presence of salts, such as LiCl and CaCl₂.^[148] Unfortunately, the resultant meta-aramid fibre mats had an extremely low strength of below 30 MPa. As has been mentioned previously, a two-step processing method including electrospinning soluble precursor solution into nanofibres and the subsequent suitable post-treatment is an efficient strategy for the preparation of non-processable polymer or inorganic nanofibre. Typical examples processed by this method are PI nanofibres. The first step is the electrospinning of polyamic acids followed by imidization by heating to a high temperature.^[38,80] In another study, conjugated polydiacetylenes nanofibres were prepared by electrospinning precursor solution containing diacetylene

1 Introduction

monomer, matrix polymer of PEO and stability enhancer of tetraethyl orthosilicate, and subsequently irradiated with 254 nm light.^[149] Regarding other conjugated or rigid-rod polymers, PBO and its copolymers^[150,151] have been electrospun into nanofibres using this indirect method and the mechanical and thermal properties of the resultant fibre mat have been explored. Thermal mechanical analysis revealed that electrospun PBO nanofibre belts sustain excellent mechanical properties even at a high temperature of 350 °C, with a tensile strength of 490 MPa and strength retention of over 90 %.

Nanofibre formation techniques of BBB and BBL are always a bottleneck to progress which has not moved forward for a long period since the 1960s. In contrast to PI and PBO, the precursor route is not suitable for BBB and BBL. The precursor solution BBB forms an insoluble and non-processable gel owing to the reaction of the four amino groups in the monomer DAB with 1,4,5,8-naphthalenetetracarboxylic dianhydride. Inspired by the fabrication of inorganic nanofibres such as SiO₂ and TiO₂,^[88,89,103] not only the macromolecules but also the small molecules can be used as a precursor for electrospinning in the presence of an electrospinnable polymer as a template. A new strategy for making BBB fibres was designed in this thesis by using the corresponding monomers' solution, DAB and NTCA dissolved in dimethylacetamide, as a precursor for electrospinning with a template polymer followed by solid-state polymerization at a high temperature with simultaneous pyrolysis of the template polymer. The fibre formation parameter, reaction process of monomers and properties of the BBB fibre mats, aligned belts and individual fibres were investigated (reference **Appendix 5.1**).

1.4 Electrospun Nanofibre-Based Sponges

Three-dimensional (3D), porous, ultra-low density, mechanically stable sponge materials have attracted a lot of attention for their wide range of applications in the fields of thermal insulation, sensors, absorption, catalyst supports, tissue engineering, battery electrodes and acoustic, vibration or shock energy shielding.^[152] Depending on the raw materials and intended applications, different methods can be used for the

1 Introduction

preparation of sponges of advanced materials, including foaming, sol-gel processing, template growth, FD or casting, self-assembly and chemical vapour deposition.^[152]

Carbon material-based aerogel, including carbon nanotubes (CNTs) and graphene, is one of the highly studied materials, due to its low-density and chemical inertness. A CNT sponge, for example, synthesized by chemical vapour deposition was reported in which a precursor solution of ferrocene in dichlorobenzene was injected at 860 °C.^[153]

This elastic and hydrophobic sponge can actively absorb and remove different type of oils spreading on the surface of the water, as shown in **Figure 1-5a-b**. In another interesting study, ultra-lightweight CNT-graphene aerogels (**Figure 1-5c**) were prepared through the bottom-up FD process and applied as a conductivity sensor (**Figure 1-5d**) and for absorption of organic solvent.^[154] Carbon fibre is a fascinating material for its outstanding physicochemical property and an extensive natural source of raw material. Carbon fibre sponge prepared from carbonation of natural fibres, such as raw cotton (**Figure 1-5e-f**),^[155] wood^[156] and bacterial cellulose,^[157] are exhibit hydrophobicity, elasticity and flame-resistance.

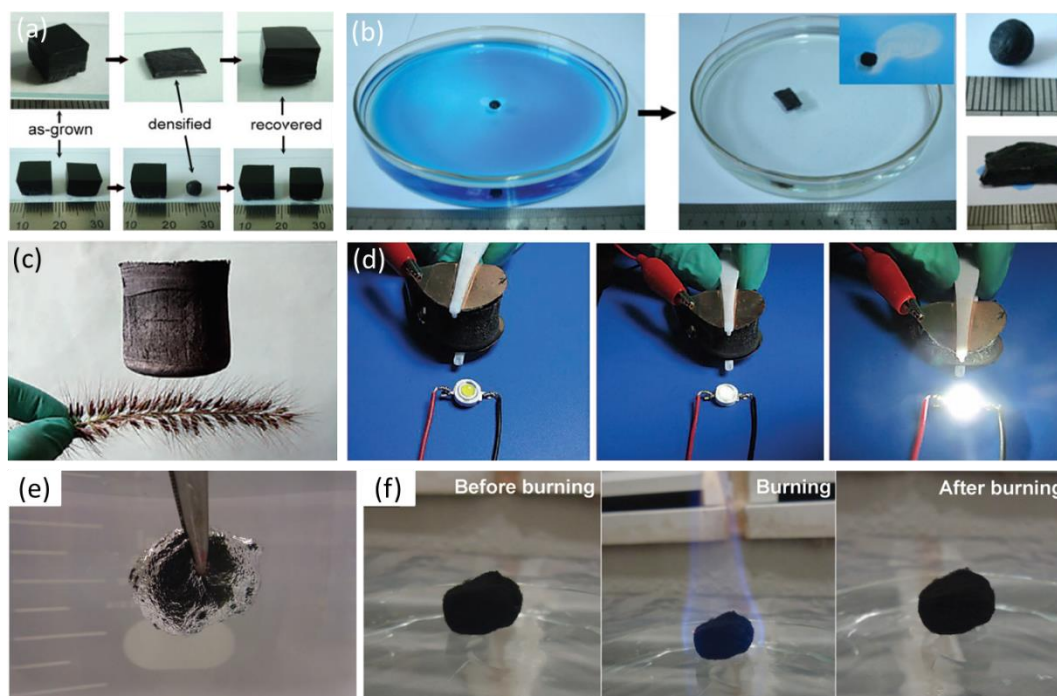


Figure1-5. (a) Photos show the elasticity of CNTs sponge from chemical vapour deposition. (b) CNTs sponge for cleaning up large areas of oil. (c) Photo of CNT-graphene sponge. (d) Elasticity-responsive conductivity of CNT-graphene sponge. (e) Photo of raw cotton-based carbon

1 Introduction

fibre sponge under the water. (f) Removal of the loaded organic solvent via combustion. (a) and (b) Reprinted with permission from ref 152. Copyright 2010 Wiley-VCH. (c) and (d) Reprinted with permission from ref 154. Copyright 2013 Wiley-VCH. (e) and (f) Reprinted with permission from ref 155. Copyright 2013 Wiley-VCH.

Large specific surface area, controllable aspect ratio and morphology, tunable wetting characteristics, versatility and easy modification endow electrospun fibre with unique advantages to fabricate 3D sponge materials, which either broaden the applications of electrospun nanofibres or provide novel properties to the sponges. In recent years, ultralight 3D sponge made from electrospun polymer nanofibres has already become a hot topic and achieved fruitful progress, especially applied in the medical and energy field. Pristine electrospun long fibres tend to randomly entangle and harden to structure stable large volume 3D architecture. Therefore, short electrospun fibres, made by mechanical cutting of long fibres, were chosen for the bottom-up assembly of 3D sponges by FD followed by some necessary post-treatment.^[152,158,159] Simply self-assembled short fibres together frequently unstable and fragile structures due to lack of effective junctions between each other. The density, porosity, pore size distribution and orientation of the final sponges can be easily altered during the FD process by controlling the concentration of short fibre dispersion, freeze rate and directions. Inspired by the biomimicry of extracellular matrix biodegradable polymer sponges, PLA,^[160] polycaprolactone^[161] and PVA^[162] were prepared with corresponding short fibres by using the approach of FD, which was applied as a scaffold in tissue engineering. In addition, polyacrylonitrile-SiO₂^[158] and polyacrylate-based polymer^[163] sponges were developed at the nearly the same time, which were used in water-in-oil emulsion separation and organic solvent absorption, drug release and catalyst supports.

Considering that most polymer-based sponges have the common drawback of poor thermal properties which limits their application in high-temperature areas, thermally

1 Introduction

stable PI short electrospun fibres were adopted to assemble superior thermal resistance sponges.^[159,163,164] Low-density and porosity self-glued PI sponge shows low thermal conductivity of $26 \text{ mW m}^{-1}\text{K}^{-1}$, making it a promising candidate for potential application as a thermal insulator, as shown in **Figure 1-6a**.^[159] Furthermore, stress-responsive conductive PI sponges were designed by the corporation of silver nanowires with PI short fibres forming a double-network structure.^[163] The conductivity of the double-network sponges alter in a wide range depending on the compression strain, as show in **Figure 1-6b**, which make an interesting application as a pressure sensor. Some other examples of thermal, stable, conjugated rigid-rod polymer sponges, some not from electrospun fibres, have to be mentioned here. The first one is PBO sponge prepared through a proton consumption-induced gelation of PBO nanofibre sol and a controlled FD with a low cooling rate, followed by thermal cross-linking.^[165] The resulting PBO sponge not only presents the similar properties to other sponges, such as porosity, low-density, low thermal conductivity (**Figure 1-6c**) and elasticity, but more importantly also shows outstanding flame-resistance (**Figure 1-6d**). The second example is a conjugated microporous polymer (CMP) aerogel achieved from a cross-coupling reaction based on 1,3,5-triethynylbenzene, as illustrated in **Figure 1-6e**.^[166] The CMP aerogels possess a low thermal conductivity of $22 \text{ mW m}^{-1} \text{ K}^{-1}$, which is an ideal application for a high-temperature insulator (**Figure 1-6f**). When treated with carbon black, CMP aerogel can effectively absorb solar energy and transfer it to heat (**Figure 1-6g**), the corresponding solar steam generation efficiencies of up to 81, 85 and 88 % are achieved at light intensities of 1, 2 and 3 kW m^{-2} , respectively. The same as a conjugated polymer, there are reasons to believe that the BBB nanofibre-based sponges have promising potential applications in thermal insulation, high-temperature filtration and as a catalyst carrier for high-temperature reactions and solar steam generation.

1 Introduction

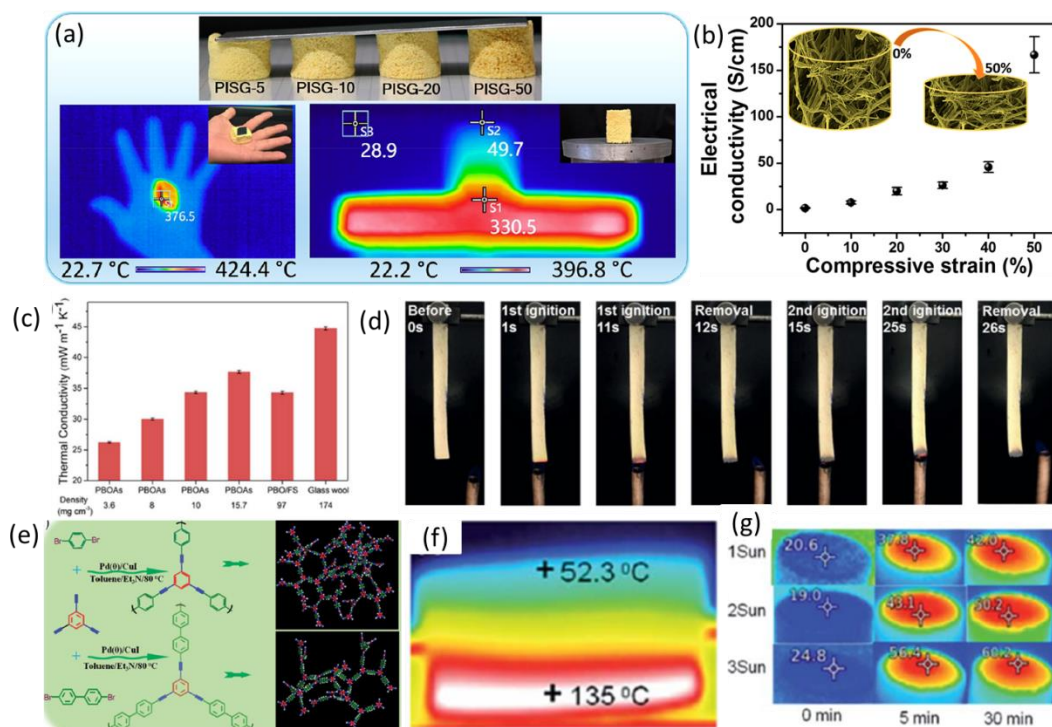


Figure 1-6. (a) PI sponge as a thermal insulator. (b) Electrical conductivity of PI/AgNW sponge changes with compression strain. (c) Thermal conductivity of PBO sponges with different density. (d) Ignition test of PBO sponges. (e) Synthesis of CMP aerogels. (f) CMP aerogel as a thermal insulator. (g) Infrared images of CMP aerogel-carbon black composite materials under different illumination and time. (a) Reprinted with permission from ref 159. Copyright (2017) American Chemical Society. (b) Reprinted with permission from ref 160. Copyright (2017) American Chemical Society. (c) and (d) Reprinted with permission from ref 165. Copyright (2018) Royal Society of Chemistry. (e)-(g) Reprinted with permission from ref 166. Copyright (2018) Royal Society of Chemistry

1.5 Polymer/Clay Composite Materials

Smectic clays are one type of naturally abundant, multilayered platelet, inorganic material with a well-characterized lamellar structured, high surface area and ionic charges on the surface.^[167] The phyllosilicate clays of the 2:1 type, including montmorillonite (MMT), bentonite, saponite and hectorite, have conventionally been employed as catalysts,^[168] adsorbents,^[169] metal chelating agents^[170] and polymer nanocomposites.^[167,171] The generic multilayered structure is constituted of

1 Introduction

silicate/aluminium oxide in multilayer stacks and counter ions sandwiched inside. These counter ions in the galleries can be exchanged with alkali metal ions, such as Na^+ or Li^+ , and further exchanged with organic ions.^[167,168] Multi-layered silicates are natively hydrophilic, water-swelling and exist in nature as large aggregates.^[167] Natural original clay, such as low price MMT available by open-cast mining, appear typically with a lateral extension $L < 250$ nm owing to their genesis in low-temperature environments.^[172] Synthetic high-purity clay, such as sodium hectorite and lithium hectorite with larger lateral extension and aspect ratios from melt synthesis processing at a high temperature, has recently attracted increasing attention. Sodium fluorohectorite, for example, obtained from a combination of melt synthesis followed by long-term annealing, shows exceptional aspect ratios of around 20,000 upon delamination.^[173] High-temperature melt synthesis of the clays not only offers the significant advantages of a larger aspect ratio, higher purity and homogeneity, but also allows the control of the nature of interlayer cation, layer charge and composition by adjusting the crucial parameters.^[174] The most common application of platelets nanomaterial such as clay is as the stiff filler incorporated in polymeric matrices for the enhancement of the mechanical, flame-retardant and gas-diffusion barrier properties.

1.5.1 Polymer/Clay Nanocomposite for Flame Retardant Application

The increased use of polymer products in varied applications results not only in the continuous demand for improved mechanical, thermal and electrical properties, but also increasing concern regarding the security and ecological pollution issues. The reduction of ignite or burn propensity of the plastic material is an efficiency measure for the security guarantee and pollution controlling of its applications in houses, commercial environments and transportation. As shown in the model illustrated in **Figure 1-7a**, the condensed- and gas-phase mechanism are generally considered as the primary effective mechanism of flame retardancy.^[175] It is nicely described in the review article by Wang et al.^[175] According to the description, if a flame retardant acts

1 Introduction

in the gas phase (flame zone) by radical absorption to break off combustion processes, it can be called a gas-phase mechanism. By contrast, the condensed-phase mechanism means that the flame-retardant functions in the condensed phase through enhancing the formation of char on the surface that serves as a barrier to inhibit flammable volatiles from diffusing to the flame zone and to shield the polymer from heat and oxygen. Many innovative solutions have been tried in previous publications to address the challenges of improving the heat- and flame-resistance of polymers based on the aforementioned mechanism.^[175-178] Phosphorus-containing additives, for example, lead to the formation of an expandable carbonaceous protective char layer, which belongs to the condensed-phase mechanism. The degradation of the additives leads to thermally stable pyro- or polyphosphoric species that catalyse polymers to form a protective barrier. On the other hand, the additives containing halogen, usually chlorine and bromine, are well-known for their inhibiting effects via the gas-phase mechanism. The additives of compounds containing halogen preferentially release specific radicals (e.g. $\text{Cl}\cdot$ and $\text{Br}\cdot$) in the gas phase that can react with highly reactive species (such as $\text{H}\cdot$ and $\text{OH}\cdot$) to form less reactive halogen atoms, thereby, suppressing the radical reactions of the combustion process.^[175,176,179] Other additives generate inert gases, thus, diluting the oxygen supply at the surface of the burning polymer, which is also classified as a gas-phase mechanism.^[179,180]

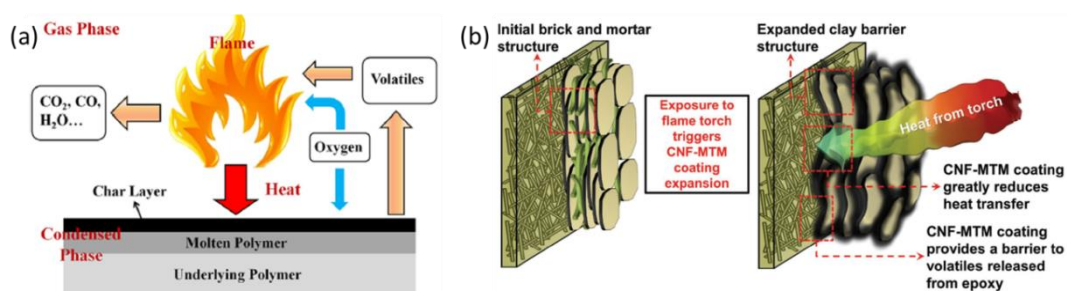


Figure 1-7. (a) Illustration of model of flame-retardant action. (b) Sketch of the fire-shielding mechanism attributed to the CNF/clay coating on epoxy composites. (a) Reprinted with permission from ref 175. Copyright (2017) Elsevier. (b) Reprinted with permission from ref 189. Copyright (2013) Wiley-VCH.

1 Introduction

However, it is unfortunate that the commonly used flame-retardants, either halogenated or phosphorous compounds, are unsuitable for large-scale applications due to their potential impacts on the environment and human health, especially the brominated flame-retardants which generate neurotoxic and potentially carcinogenic brominated furans and dioxins.^[181-183] Inorganic fillers, such as layered silicate (clay), SiO₂, metal oxide and carbonaceous (CNTs, graphene), have been extensively studied as effective additives for polymer-based nanocomposite materials focusing on improved fire retardancy with superior mechanical properties without the toxicity and leaching issues.^[175,177] Two types of strategies, including directly blending in the matrix^[184] and coating on the surface of the substance,^[185,186] are usually adopted for the employment of inorganic additives, also classified as a condensed-phase mechanism.

New types of intrinsic flame-shielding papers/films were developed with the incorporation of one-dimensional nanofibres and two-dimensional nanoplatelets.^[187,188] The multilayer intercalation of nanofibre between the clay platelets produce a lot of nanogaps which makes it lower density and flexible, reduces the heat transfer but does not influence the flame-resistance property. In one study, nanopaper with the thickness of only 100 µm based on multilayers of aligned clay nanoplatelets in a cellulose nanofibre matrix, as sketched in **Figure 1-7b**, exhibits an extreme flame-shielding effect and a reduction of heat transportation.^[189] In another report, a ternary, bioinspired mechanically strong nanocomposite film, containing renewable forestry waste, montmorillonite and reduced graphene oxide, were fabricated by utilizing the synergistic effect of hydrogen and covalent bonds among them.^[190] The resultant films also demonstrate very good flame-shielding effects.

Development of low-density 3D polymer/clay aerogels or sponges with intrinsic flame retardancy and thermal insulation properties is an interesting and practical significant direction. The FD process utilized to produce these aerogels is unique in its ability to produce polymer/clay composites containing 25–75 wt% clay, whereas the

1 Introduction

traditional melt compounded clay composites rarely exceed 5 % clay content due to viscosity limitations.^[186] A water-soluble polymer, such as PVA, and alginate are commonly used as the binder/matrix to construct nanocomposite sponges but other binder/ matrix are used.^[191-193] Self-extinguishing sponges, for example, composed of biopolymer poly(furfuryl alcohol) and clay were synthesized by *in situ* polymerization of furfuryl alcohol in water, in the presence of MMT clay, followed by the an FD process.^[194] Non-flammable alginate-based nanocomposite aerogels with low thermal conductivity and useful mechanical strengths were also fabricated using the similar method.^[195]

The additives normally used to facilitate the formation of a continuous char barrier or generation of active radicals and inert gas just slow down the rate of polymer mass loss but do not stop completely.^[184 -186] The same is true that the total heat release does not decrease but rather spreads out over a longer time with a concomitant reduction of the peak of heat release rate. Another direction for making polymer intrinsically flame-resistant is the introduction of aromatic units and heterocyclic rings in the molecule chains.^[196] High-performance rigid-rod polymers, talked about in 1.3.1, such as polyamides, PIs, PBI and PBO, have high degradation temperatures and self-extinguishing properties because of their highly rigid backbones and strong chain-to-chain interactions. These polymers exhibit a negligible heat release rate on burning and release little smoke prior to decomposition with the release of water, carbon oxides, and traces of hydrogen cyanide.^[196] The exploration of BBB regarding fire resistance is rarely reported but the potential has been predicted by its molecule structures.

1.5.2 Strong Polymer/Clay Nanocomposite for Gas Barrier Application

Highly transparent, flexible and affordable gases diffusion barrier technologies are highly required ranging from low-tech films for flexible packaging to high-tech products for encapsulation of thin-film transistors and organic light-emitting diode displays.^[197-199] Still, many polymer barriers are less effective than desired.^[200]

1 Introduction

Incorporation of layered nanoplatelets with large aspect ratios, such as clay and graphene oxide or graphene, is an efficient and economical way to enhance the gas barrier property. In contrast to the high price, clays have more advantages regarding larger-scale applications, particularly for relatively low-tech food packaging. The performance of the gas diffusion barrier films is determined by three main factors: Filler properties (aspect ratio, volume fraction), the intrinsic barrier property of the polymer matrix and the quality of filler distribution (aggregation, orientation of filler platelets, free volume generated by mediocre interface management).^[201-203] As illustrated in **Figure 1-8a**, according to Cussler's suggestion, the diffusion path of oxygen molecules through a highly aligned barrier membrane is not a staircase-like pattern; rather, the molecule follows a more extended route between nanosheets layers and travels perpendicular to the diffusion direction.^[201] Nielsen proposed a very similar model for the relative permeability for a regular arrangement of platelets and give predictions for the relative permeability of the nanocomposite with different platelets volume fraction and different particle aspect ratios (**Figure 1-8b**).^[203] Based on their theory, the synthetic hectorite, which is completely exfoliated with a larger aspect ratio, is the best choice as the filler. Möller et al. compared the barrier and optical properties of the natural MMT and a series of synthesis hectorite-coated polypropylene films. The results show that the lithium-hectorite with an aspect ratio $\gg 1000$ is superior in the barrier properties enhancement which represents as little as 0.4 % of the neat PP substrate's transmission rate.^[202]

Traditional melt extrusion for blending thermoplastic polymer and clay is limited due to the inefficient exfoliation of platelets filler and the concentration of filler, and thereby decreasing the aspect ratio. Zhou et al. concluded the state-of-the-art method for the preparation of clay containing films and their functionality.^[171] Solvent casting, spin-casting (**Figure 1-8c**) and doctor blading (**Figure 1-8d**) are frequently used approaches for assembling polymer/clay nanocomposite films. The existence of clay nanoplatelets homogenously distributed on the complete films frequently increases

1 Introduction

the mechanical and barrier properties. In some cases, the results show that a high content of clay will lead to non-uniform and brittle films. The layer of many of these mineral clays is negatively charged, because of isomorphous substitution,^[171] which might cause aggregation or precipitation of clay in some organic solvent or meet with some charged polymers. Modification of clay with organic compounds through cation exchange has proven an efficient way to eliminate the aggregation in the dispersion and enhance the interaction between clay platelets and polymer matrix after solidification.^[204,205] Many researchers have reported on the preparation of platelet-reinforced polymer/clay nanocomposites with high strength and toughness by mimicking the mechanically excellent structure of nacre. Das et al. prepared transparent, highly ordered, large-scale nacre-mimetics films via incorporation of different aspect ratios between nanoclay and PVA matrix and investigated the relationships among structure formation, nanostructure, deformation mechanisms, mechanical properties and the aspect ratio of the filler.^[206] Investigation results demonstrate a large aspect ratio benefit, and superior mechanical and barrier properties. Walther et al. report a nacre mimetic paper with excellent mechanical properties, lightweight character and fire- and heat-shielding performances prepared through a paper-making process by using poly(diallyldimethyl-ammonium chloride) modified montmorillonite as a raw material.^[187] Many other studies have also suggested that the functional films containing clay have potential applications in many areas, such as catalysis, modified electrodes, optoelectronic devices, and anti-corrosion and packaging materials.^[197,207,208]

On the other hand, coating a compact layer of clay containing nanocomposite with nanoscale thickness on the surface of the matrix films can enhance the barrier properties extremely regarding the precondition of retaining the intrinsic excellent mechanical and optical properties. The facile strategies for polymer and clay nanocomposite coating include drop-casting, spray coating, layer-by-layer assembling (**Figure 1-8e**) and vertical and horizontal deposition (**Figure 1-8f**).^[171] All of these

1 Introduction

coating processes enable the versatile and benign assembly of the polymer and clay nanocomposite layer on the substrate with different thicknesses and morphologies.

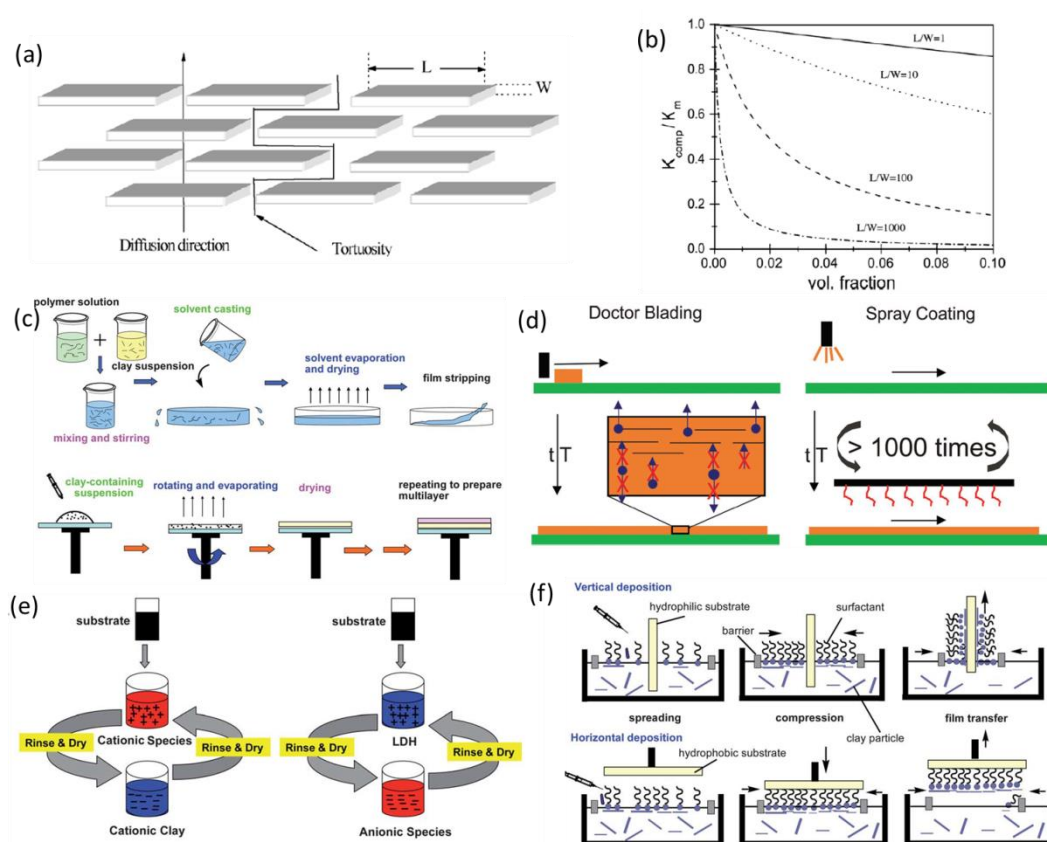


Figure 1-8. (a) Model of gas diffusion through the parallel arranged platelets nanocomposite. (b) Predictions of Nielsen's model for the relative permeability as a function of platelets volume fraction for different particle aspect ratios. (c)-(f) The preparation methods of films or coating containing clay; (c) solution casting; (d) doctor blading and spray coating; (e) layer by layer assembling; (f) vertical and horizontal deposition (Langmuir-Blodgett technique). (a) and (b) Reprinted with permission from ref 203. Copyright (2009) Elsevier. (c), (e) and (f) Reprinted with permission from ref 171. Copyright (2011) Royal Society of Chemistry.

Inspired by mussel shell-like natural bio-nanocomposites, for example, a nanocomposite layer containing cationic recombinant spider silk protein and synthetic sodium hectorite was coated onto a PET substrate by an all aqueous-based drop-casting process.^[209] The testing results of the oxygen transmission rate (OTR) demonstrated the bio-nanocomposite is 60-fold more efficient than high-performance

1 Introduction

packaging materials such as poly(vinylidene chloride) and 600-fold better than PET, which makes it highly suitable for new, green, flexible packaging applications. In another report, a modified hectorite and polyurethane nanocomposite layer was coated on PET foil by simple doctor-blading.^[210] The coated nanocomposite layer with a thickness as low as 1.5 μm , but with an enhanced OTR and water vapour transmission rates reached exceptionally low values of $1.0 \times 10^{-2} \text{ cm}^3 \text{ m}^{-2} \text{ day}^{-1} \text{ bar}^{-1}$ and $< 0.05 \text{ g m}^{-2} \text{ day}^{-1}$ at 50 % relative humidity (RH), respectively. One example of spray coating is given by Habel et al.: A glycol chitosan-clay nanocomposite layer was coated on PLA film via spraying with “all green” solution.^[211] The resultant fully degradable polymer-based film shows competitive oxygen barrier properties (OTR = $0.17 \text{ cm}^3 \text{ m}^{-2} \text{ day}^{-1} \text{ bar}^{-1}$ at 75 % RH) which affords a valuable alternative to conventional less eco-friendly food packaging materials.

Utilizing the opposite charged character, layer-by-layer assembly, multilayer structured coating of alternate depositions of clay and polyelectrolyte on the polymer substrate was designed.^[212,213] The thickness of the bilayer of clay and polyelectrolyte can be controlled by changing the concentration of the clay suspension and the polyelectrolyte solution, as well as the number of layers. Polyelectrolytes such as poly(diallyldimethylammonium chloride), poly(ethylenimine), poly(vinylbenzyl quaternary ammonium chloride), and polyacrylamide have been used to form layer-by-layer films with clay platelets.^[171] In one study, a 231 nm assembly was formed after 70 layers of poly(ethylenimine) and clay coating on 179 μm PET film, and the OTR was below the detection limit of commercial instrumentation ($< 0.005 \text{ cc}/(\text{m}^2 \text{ day atm})$).^[212] Vertical and horizontal deposition, also known as the Langmuir-Blodgett technique, is adopted to coat the ionic surfactant-modified nanoclay on the substrate material by controlling the hydrophilicity and hydrophobicity.^[171,214,215] The substrate materials for Langmuir-Blodgett assembly focus on inorganic materials, such as silicon and glass, so as to lack of the example for the gas barrier application.

1 Introduction

1 Introduction

1.6 References

- [1] A. Greiner, J. H. Wendorff, Electrospinning: a fascinating method for the preparation of ultrathin fibers, *Angew Chem Int Ed*, 46 (2007), 5670.
- [2] J. Xue, T. Wu, Y. Dai, Y. Xia, Electrospinning and Electrospun Nanofibers: Methods, Materials, and Applications, *Chem Rev*, (2019), DOI: 10.1021/acs.chemrev.8b00593.
- [3] S. Agarwal, M. Burgard, A. Greiner, & J. Wendorff. *Electrospinning: A Practical guide to nanofibers*. Walter de Gruyter GmbH & Co KG, 2016.
- [4] J. F. Cooley, Apparatus for electrically dispersing fluids. U.S. Pat. 692,631, 1902.
- [5] W. J. Morton, Method of dispersing fluids. U.S. Pat. 705,691, 1902.
- [6] Formhals, A. Method and Apparatus for Spinning. U.S. Pat. 2,349,950, 1944.
- [7] G. I. Taylor, Disintegration of water drops in an electric field, *Proceedings of the Royal Society of London Series A Mathematical and Physical Sciences*, 280 (1964), 383.
- [8] G. I. Taylor, The force exerted by an electric field on a long cylindrical conductor, *Proceedings of the Royal Society of London Series A Mathematical and Physical Sciences*, 291 (1966), 145.
- [9] G. I. Taylor, Electrically driven jets, *Proceedings of the Royal Society of London A Mathematical and Physical Sciences*, 313 (1969), 453.
- [10] H. Fong, I. Chun, D. Reneker, Beaded nanofibers formed during electrospinning, *Polymer*, 40 (1999), 4585.
- [11] D. H. Reneker, A. L. Yarin, H. Fong, S. Koombhongse, Bending instability of electrically charged liquid jets of polymer solutions in electrospinning, *J Appl Phys*, 87 (2000), 4531.
- [12] Y. Shin, M. Hohman, M. Brenner, G. Rutledge, Experimental characterization of electrospinning: the electrically forced jet and instabilities, *Polymer*, 42 (2001), 09955.
- [13] H. Dai, J. Gong, H. Kim, D. Lee, A novel method for preparing ultra-fine alumina-borate oxide fibres via an electrospinning technique, *Nanotechnology*, 13 (2002), 674.
- [14] Z. Sun, E. Zussman, A. L. Yarin, J. H. Wendorff, A. Greiner, Compound core-shell polymer nanofibers by co-electrospinning, *Adv Mater*, 15 (2003), 1929.
- [15] J. T. McCann, D. Li, Y. Xia, Electrospinning of nanofibers with core-sheath, hollow, or

1 Introduction

porous structures, *J Mater Chem*, 15 (2005), 735.

[16] D. Li, Y. Xia, Direct fabrication of composite and ceramic hollow nanofibers by electrospinning, *Nano Lett*, 4 (2004), 933.

[17] A. C. Patel, S. Li, C. Wang, W. Zhang, Y. Wei, Electrospinning of porous silica nanofibers containing silver nanoparticles for catalytic applications, *Chem Mater*, 19 (2007), 1231.

[18] Q. Liu, J. Zhu, L. Zhang, Y. Qiu, Recent advances in energy materials by electrospinning, *Renewable and Sustainable Energy Reviews*, 81 (2018), 1825.

[19] D. S. Coelho, B. Veleirinho, T. Alberti, A. Maestri, R. Yunes, P. F. Dias, M. Maraschin, Electrospinning Technology: Designing Nanofibers toward Wound Healing Application. In *Nanofibers-from Preparation to Applications*, IntechOpen: 2018.

[20] S. Chen, R. Li, X. Li, J. Xie, Electrospinning: An enabling nanotechnology platform for drug delivery and regenerative medicine, *Advanced drug delivery reviews*, 132 (2018), 188.

[21] M. Shin, H. Yoshimoto, J. P. Vacanti, In vivo bone tissue engineering using mesenchymal stem cells on a novel electrospun nanofibrous scaffold, *Tissue Eng*, 10 (2004), 33.

[22] Y. Liao, C.-H. Loh, M. Tian, R. Wang, A. G. Fane, Progress in electrospun polymeric nanofibrous membranes for water treatment: fabrication, modification and applications, *Prog Polym Sci*, 77 (2018), 69.

[23] M. Zhu, J. Han, F. Wang, W. Shao, R. Xiong, Q. Zhang, H. Pan, Y. Yang, S. K. Samal, F. Zhang, Electrospun nanofibers membranes for effective air filtration, *Macromolecular Materials and Engineering*, 302 (2017), 1600353.

[24] D. H. Reneker, A. L. Yarin, Electrospinning jets and polymer nanofibers, *Polymer*, 49 (2008), 2387.

[25] A. L. Yarin, S. Koombhongse, D. H. Reneker, Taylor cone and jetting from liquid droplets in electrospinning of nanofibers, *J Appl Phys*, 90 (2001), 4836.

[26] S. Agarwal, A. Greiner, J. H. Wendorff, Functional materials by electrospinning of polymers, *Prog Polym Sci*, 38 (2013), 963.

[27] D. Li, Y. Xia, Electrospinning of Nanofibers: Reinventing the Wheel?, *Adv Mater*, 16 (2004), 1151.

1 Introduction

- [28] D. H. Reneker, H. Fong, Eds. *Polymeric Nanofibers*. American Chemical Society: Washington, DC, USA, 2006, DOI: 10.1021/bk-2006-0918.
- [29] D. Li, M. Marquez, Y. Xia, Capturing electrified nanodroplets under Rayleigh instability by coupling electrospray with a sol–gel reaction, *Chem Phys Lett*, 445 (2007), 271.
- [30] D. Duft, T. Achtzehn, R. Müller, B. A. Huber, T. Leisner, Coulomb fission: Rayleigh jets from levitated microdroplets, *Nature*, 421 (2003), 128.
- [31] M. E. Helgeson, K. N. Grammatikos, J. M. Deitzel, N. J. Wagner, Theory and kinematic measurements of the mechanics of stable electrospun polymer jets, *Polymer*, 49 (2008), 2924.
- [32] D. R. Salem, *Structure formation in polymeric fibers*. Carl Hanser Verlag GmbH Co KG: 2018.
- [33] G. Collins, J. Federici, Y. Imura, L. H. Catalani, Charge generation, charge transport, and residual charge in the electrospinning of polymers: A review of issues and complications, *J Appl Phys*, 111 (2012), 044701.
- [34] L. H. Catalani, G. Collins, M. Jaffe, Evidence for molecular orientation and residual charge in the electrospinning of poly (butylene terephthalate) nanofibers, *Macromolecules*, 40 (2007), 1693.
- [35] Y. Filatov, A. Budyka, V. Kirichenko, Electrospinning of micro-and nanofibers: fundamentals in separation and filtration processes, *J Eng Fibers Fabrics*, 3 (2007), 488.
- [36] S. A. Theron, A. L. Yarin, E. Zussman, E. Kroll, Multiple jets in electrospinning: experiment and modeling, *Polymer*, 46 (2005), 2889.
- [37] O. Akampumuza, H. Gao, H. Zhang, D. Wu, X.-H. Qin, Raising Nanofiber Output: The Progress, Mechanisms, Challenges, and Reasons for the Pursuit, *Macromolecular Materials and Engineering*, 303 (2018), 1700269.
- [38] Y. Ding, H. Hou, Y. Zhao, Z. Zhu, H. Fong, Electrospun polyimide nanofibers and their applications, *Prog Polym Sci*, 61 (2016), 67.
- [39] I. G. Loscertales, A. Barrero, I. Guerrero, R. Cortijo, M. Marquez, A. M. Gañán-Calvo, Micro/Nano Encapsulation via Electrified Coaxial Liquid Jets, *Science*, 295 (2002), 1695.
- [40] G.-Z. Yang, J.-J. Li, D.-G. Yu, M.-F. He, J.-H. Yang, G. R. Williams, Nanosized

1 Introduction

sustained-release drug depots fabricated using modified tri-axial electrospinning, *Acta biomaterialia*, 53 (2017), 233.

[41] N. Thoppey, J. Bochinski, L. Clarke, R. Gorga, Edge electrospinning for high throughput production of quality nanofibers, *Nanotechnology*, 22 (2011), 345301.

[42] D. Lukas, A. Sarkar, P. Pokorny, Self-organization of jets in electrospinning from free liquid surface: A generalized approach, *J Appl Phys*, 103 (2008), 084309.

[43] G. Jiang, S. Zhang, Y. Wang, X. Qin, An improved free surface electrospinning with micro-bubble solution system for massive production of nanofibers, *Mater Lett*, 144 (2015), 22.

[44] H. Niu, T. Lin, X. Wang, Needleless electrospinning. I. A comparison of cylinder and disk nozzles, *J Appl Polym Sci*, 114 (2009), 3524.

[45] M. G. McKee, J. M. Layman, M. P. Cashion, T. E. Long, Phospholipid Nonwoven Electrospun Membranes, *Science*, 311 (2006), 353.

[46] M. Hecht, B. Soberats, J. Zhu, V. Stepanenko, S. Agarwal, A. Greiner, F. Wüthner, Anisotropic microfibrils of a liquid-crystalline diketopyrrolopyrrole by self-assembly-assisted electrospinning, *Nanoscale Horizons*, 4 (2019), 169.

[47] B. W. Tillman, S. K. Yazdani, S. J. Lee, R. L. Geary, A. Atala, J. J. Yoo, The in vivo stability of electrospun polycaprolactone-collagen scaffolds in vascular reconstruction, *Biomaterials*, 30 (2009), 583.

[48] C. Zhou, Q. Shi, W. Guo, L. Terrell, A. T. Qureshi, D. J. Hayes, Q. Wu, Electrospun bio-nanocomposite scaffolds for bone tissue engineering by cellulose nanocrystals reinforcing maleic anhydride grafted PLA, *ACS applied materials & interfaces*, 5 (2013), 3847.

[49] H. K. Makadia, S. J. Siegel, Poly Lactic-co-Glycolic Acid (PLGA) as Biodegradable Controlled Drug Delivery Carrier, *Polymers*, 3 (2011), 1377.

[50] Y. Zhang, G. C. Rutledge, Electrical conductivity of electrospun polyaniline and polyaniline-blend fibers and mats, *Macromolecules*, 45 (2012), 4238.

[51] I. S. Chronakis, S. Grapenson, A. Jakob, Conductive polypyrrole nanofibers via electrospinning: electrical and morphological properties, *Polymer*, 47 (2006), 1597.

[52] S. W. Choi, S. M. Jo, W. S. Lee, Y.-R. Kim, An Electrospun Poly(vinylidene fluoride)

1 Introduction

- Nanofibrous Membrane and Its Battery Applications, *Adv Mater*, 15 (2003), 2027.
- [53] S. V. Fridrikh, H. Y. Jian, M. P. Brenner, G. C. Rutledge, Controlling the fiber diameter during electrospinning, *Phys Rev Lett*, 90 (2003), 144502.
- [54] A. Haider, S. Haider, I.-K. Kang, A comprehensive review summarizing the effect of electrospinning parameters and potential applications of nanofibers in biomedical and biotechnology, *Arabian Journal of Chemistry*, 11 (2018), 1165.
- [55] N. A. Barakat, M. A. Kanjwal, F. A. Sheikh, H. Y. Kim, Spider-net within the N6, PVA and PU electrospun nanofiber mats using salt addition: Novel strategy in the electrospinning process, *Polymer*, 50 (2009), 4389.
- [56] V. V. T. Padil, C. Senan, S. Wacławek, M. LERNÍK, Electrospun fibers based on Arabic, karaya and kondagogu gums, *Int J Biol Macromol*, 91 (2016), 299.
- [57] F. Ozel, M. Kus, A. Yar, E. Arkan, M. Z. Yigit, A. Aljabour, S. Büyükcebi, C. Tozlu, M. Ersoz, Electrospinning of $\text{Cu}_2\text{ZnSnSe}_4\text{-xSx}$ nanofibers by using PAN as template, *Mater Lett*, 140 (2015), 23.
- [58] D. W. Hutmacher, P. D. Dalton, Melt Electrospinning, *Chemistry – An Asian Journal*, 6 (2011), 44.
- [59] P. D. Dalton, K. Klinkhammer, J. Salber, D. Klee, M. Möller, Direct in vitro electrospinning with polymer melts, *Biomacromolecules*, 7 (2006), 686.
- [60] M. Molki, P. Damronglerd, Electrohydrodynamic enhancement of heat transfer for developing air flow in square ducts, *Heat Transfer Engineering*, 27 (2006), 35.
- [61] R. Nayak, I. L. Kyratzis, Y. B. Truong, R. Padhye, L. Arnold, Melt-electrospinning of polypropylene with conductive additives, *Journal of Materials Science*, 47 (2012), 6387.
- [62] Y. Feng, T. Xiong, S. Jiang, S. Liu, H. Hou, Mechanical properties and chemical resistance of electrospun polytetrafluoroethylene fibres, *RSC Advances*, 6 (2016), 24250.
- [63] J. Geltmeyer, J. De Roo, F. Van den Broeck, J. C. Martins, K. De Buysser, K. De Clerck, The influence of tetraethoxysilane sol preparation on the electrospinning of silica nanofibers, *J Sol-Gel Sci Technol*, 77 (2016), 453.
- [64] Y. Gu, D. Chen, X. Jiao, Synthesis and electrochemical properties of nanostructured LiCoO_2

1 Introduction

fibers as cathode materials for lithium-ion batteries, *The Journal of Physical Chemistry B*, 109 (2005), 17901.

[65] L. Hou, N. Wang, J. Wu, Z. Cui, L. Jiang, Y. Zhao, Bioinspired Superwettability Electrospun Micro/Nanofibers and Their Applications, *Adv Funct Mater*, 28 (2018), 1801114.

[66] S. Koombhongse, W. Liu, D. H. Reneker, Flat polymer ribbons and other shapes by electrospinning, *J Polym Sci, Part B: Polym Phys*, 39 (2001), 2598.

[67] H. Dong, N. Wang, L. Wang, H. Bai, J. Wu, Y. Zheng, Y. Zhao, L. Jiang, Bioinspired Electrospun Knotted Microfibers for Fog Harvesting, *ChemPhysChem*, 13 (2012), 1153.

[68] M. Bognitzki, W. Czado, T. Frese, A. Schaper, M. Hellwig, M. Steinhart, A. Greiner, J. H. Wendorff, Nanostructured Fibers via Electrospinning, *Adv Mater*, 13 (2001), 70.

[69] C. L. Casper, J. S. Stephens, N. G. Tassi, D. B. Chase, J. F. Rabolt, Controlling surface morphology of electrospun polystyrene fibers: effect of humidity and molecular weight in the electrospinning process, *Macromolecules*, 37 (2004), 573.

[70] P. Dayal, J. Liu, S. Kumar, T. Kyu, Experimental and theoretical investigations of porous structure formation in electrospun fibers, *Macromolecules*, 40 (2007), 7689.

[71] K. A. G. Katsogiannis, G. T. Vladislavjević, S. Georgiadou, R. Rahmani, Assessing the increase in specific surface area for electrospun fibrous network due to pore induction, *ACS applied materials & interfaces*, 8 (2016), 29148.

[72] Z. Liu, D. D. Sun, P. Guo, J. O. Leckie, An efficient bicomponent TiO₂/SnO₂ nanofiber photocatalyst fabricated by electrospinning with a side-by-side dual spinneret method, *Nano Lett*, 7 (2007), 1081.

[73] W. Ye, J. Zhu, X. Liao, S. Jiang, Y. Li, H. Fang, H. Hou, Hierarchical three-dimensional micro/nano-architecture of polyaniline nanowires wrapped-on polyimide nanofibers for high performance lithium-ion battery separators, *J Power Sources*, 299 (2015), 417.

[74] D. Li, J. T. McCann, Y. Xia, Use of Electrospinning to Directly Fabricate Hollow Nanofibers with Functionalized Inner and Outer Surfaces, *Small*, 1 (2005), 83.

[75] A. V. Bazilevsky, A. L. Yarin, C. M. Megaridis, Co-electrospinning of core-shell fibers using a single-nozzle technique, *Langmuir*, 23 (2007), 2311.

1 Introduction

- [76] H. Chen, N. Wang, J. Di, Y. Zhao, Y. Song, L. Jiang, Nanowire-in-microtube structured core/shell fibers via multifluidic coaxial electrospinning, *Langmuir*, 26 (2010), 11291.
- [77] R. Jin, Y. Yang, Y. Xing, L. Chen, S. Song, R. Jin, Facile synthesis and properties of hierarchical double-walled copper silicate hollow nanofibers assembled by nanotubes, *ACS nano*, 8 (2014), 3664.
- [78] H. Chen, J. Di, N. Wang, H. Dong, J. Wu, Y. Zhao, J. Yu, L. Jiang, Fabrication of hierarchically porous inorganic nanofibers by a general microemulsion electrospinning approach, *small*, 7 (2011), 1779.
- [79] C. Niu, J. Meng, X. Wang, C. Han, M. Yan, K. Zhao, X. Xu, W. Ren, Y. Zhao, L. Xu, General synthesis of complex nanotubes by gradient electrospinning and controlled pyrolysis, *Nature communications*, 6 (2015), 7402.
- [80] S. Chen, P. Hu, A. Greiner, C. Cheng, H. Cheng, F. Chen, H. Hou, Electrospun nanofiber belts made from high performance copolyimide, *Nanotechnology*, 19 (2007), 015604.
- [81] U. Ali, Y. Zhou, X. Wang, T. Lin, Direct electrospinning of highly twisted, continuous nanofiber yarns, *Journal of the Textile Institute*, 103 (2012), 80.
- [82] S. Zhang, H. Liu, N. Tang, J. Ge, J. Yu, B. Ding, Direct electronetting of high-performance membranes based on self-assembled 2D nanoarchitected networks, *Nature Communications*, 10 (2019), 1458.
- [83] Y. Wang, W. Li, Y. Xia, X. Jiao, D. Chen, Electrospun flexible self-standing γ -alumina fibrous membranes and their potential as high-efficiency fine particulate filtration media, *Journal of Materials Chemistry A*, 2 (2014), 15124.
- [84] C. Wang, S. Wu, M. Jian, J. Xie, L. Xu, X. Yang, Q. Zheng, Y. Zhang, Silk nanofibers as high efficient and lightweight air filter, *Nano Research*, 9 (2016), 2590.
- [85] B. Liu, S. Zhang, X. Wang, J. Yu, B. Ding, Efficient and reusable polyamide-56 nanofiber/nets membrane with bimodal structures for air filtration, *J Colloid Interface Sci*, 457 (2015), 203.
- [86] C. Liu, P.-C. Hsu, H.-W. Lee, M. Ye, G. Zheng, N. Liu, W. Li, Y. Cui, Transparent air filter for high-efficiency PM 2.5 capture, *Nature communications*, 6 (2015), 6205.

1 Introduction

- [87] J. Kim, S. Chan Hong, G. N. Bae, J. H. Jung, Electrospun magnetic nanoparticle-decorated nanofiber filter and its applications to high-efficiency air filtration, *Environmental science & technology*, 51 (2017), 11967.
- [88] S. Krishnamoorthy, C. Hinderling, H. Heinzelmann, Nanoscale patterning with block copolymers, *Mater Today*, 9 (2006), 40.
- [89] Q. Wen, J. Di, Y. Zhao, Y. Wang, L. Jiang, J. Yu, Flexible inorganic nanofibrous membranes with hierarchical porosity for efficient water purification, *Chemical Science*, 4 (2013), 4378.
- [90] Y. Wang, H. Huang, J. Gao, G. Lu, Y. Zhao, Y. Xu, L. Jiang, TiO₂-SiO₂ composite fibers with tunable interconnected porous hierarchy fabricated by single-spinneret electrospinning toward enhanced photocatalytic activity, *Journal of Materials Chemistry A*, 2 (2014), 12442.
- [91] G. Xu, Y. Xie, J. Cao, M. Tao, W.-Q. Zhang, Highly selective and efficient chelating fiber functionalized by bis (2-pyridylmethyl) amino group for heavy metal ions, *Polymer Chemistry*, 7 (2016), 3874.
- [92] M. Ma, M. Gupta, Z. Li, L. Zhai, K. K. Gleason, R. E. Cohen, M. F. Rubner, G. C. Rutledge, Decorated electrospun fibers exhibiting superhydrophobicity, *Adv Mater*, 19 (2007), 255.
- [93] X. Li, M. Wang, C. Wang, C. Cheng, X. Wang, Facile immobilization of Ag nanocluster on nanofibrous membrane for oil/water separation, *ACS applied materials & interfaces*, 6 (2014), 15272.
- [94] L. Wang, S. Yang, J. Wang, C. Wang, L. Chen, Fabrication of superhydrophobic TPU film for oil-water separation based on electrospinning route, *Mater Lett*, 65 (2011), 869.
- [95] J.-W. Jung, C.-L. Lee, S. Yu, I.-D. Kim, Electrospun nanofibers as a platform for advanced secondary batteries: a comprehensive review, *Journal of materials chemistry A*, 4 (2016), 703.
- [96] Z. Dong, S. J. Kennedy, Y. Wu, Electrospinning materials for energy-related applications and devices, *J Power Sources*, 196 (2011), 4886.
- [97] L. Bulusheva, A. Okotrub, A. Kurennya, H. Zhang, H. Zhang, X. Chen, H. Song, Electrochemical properties of nitrogen-doped carbon nanotube anode in Li-ion batteries, *Carbon*, 49 (2011), 4013.
- [98] Y. Xu, Y. Zhu, C. Wang, Mesoporous carbon/silicon composite anodes with enhanced

1 Introduction

- performance for lithium-ion batteries, *Journal of materials chemistry A*, 2 (2014), 9751.
- [99] J. Shin, K. Park, W.-H. Ryu, J.-W. Jung, I.-D. Kim, Graphene wrapping as a protective clamping layer anchored to carbon nanofibers encapsulating Si nanoparticles for a Li-ion battery anode, *Nanoscale*, 6 (2014), 12718.
- [100] K. Liu, W. Liu, Y. Qiu, B. Kong, Y. Sun, Z. Chen, D. Zhuo, D. Lin, Y. Cui, Electrospun core-shell microfiber separator with thermal-triggered flame-retardant properties for lithium-ion batteries, *Science advances*, 3 (2017), e1601978.
- [101] C. Wang, Y. V. Kaneti, Y. Bando, J. Lin, C. Liu, J. Li, Y. Yamauchi, Metal–organic framework-derived one-dimensional porous or hollow carbon-based nanofibers for energy storage and conversion, *Materials Horizons*, 5 (2018), 394.
- [102] Y. Sun, R. B. Sills, X. Hu, Z. W. Seh, X. Xiao, H. Xu, W. Luo, H. Jin, Y. Xin, T. Li, A bamboo-inspired nanostructure design for flexible, foldable, and twistable energy storage devices, *Nano Lett*, 15 (2015), 3899.
- [103] X. Zhang, V. Thavasi, S. G. Mhaisalkar, S. Ramakrishna, Novel hollow mesoporous 1D TiO₂ nanofibers as photovoltaic and photocatalytic materials, *Nanoscale*, 4 (2012), 1707.
- [104] Y. Cao, Y.-J. Dong, H.-L. Feng, H.-Y. Chen, D.-B. Kuang, Electrospun TiO₂ nanofiber based hierarchical photoanode for efficient dye-sensitized solar cells, *Electrochim Acta*, 189 (2016), 259.
- [105] W. S. Yang, B.-W. Park, E. H. Jung, N. J. Jeon, Y. C. Kim, D. U. Lee, S. S. Shin, J. Seo, E. K. Kim, J. H. Noh, Iodide management in formamidinium-lead-halide–based perovskite layers for efficient solar cells, *Science*, 356 (2017), 1376.
- [106] W. Xu, X. Hu, S. Zhuang, Y. Wang, X. Li, L. Zhou, S. Zhu, J. Zhu, Flexible and salt resistant Janus absorbers by electrospinning for stable and efficient solar desalination, *Advanced Energy Materials*, 8 (2018), 1702884.
- [107] T. Wu, H. Li, M. Xie, S. Shen, W. Wang, M. Zhao, X. Mo, Y. Xia, Incorporation of gold nanocages into electrospun nanofibers for efficient water evaporation through photothermal heating, *Materials Today Energy*, 12 (2019), 129.
- [108] Y. Zhang, J. Ge, Z. Liu, Enhanced activity of immobilized or chemically modified

1 Introduction

enzymes, *Acs Catalysis*, 5 (2015), 4503.

[109] Z. Ding, Q. Cheng, L. Zou, J. Fang, Z. Zou, H. Yang, Controllable synthesis of titanium nitride nanotubes by coaxial electrospinning and their application as a durable support for oxygen reduction reaction electrocatalysts, *Chem Commun*, 53 (2017), 13233.

[110] P. Lu, B. Qiao, N. Lu, D. C. Hyun, J. Wang, M. J. Kim, J. Liu, Y. Xia, Photochemical Deposition of Highly Dispersed Pt Nanoparticles on Porous CeO₂ Nanofibers for the Water-Gas Shift Reaction, *Adv Funct Mater*, 25 (2015), 4153.

[111] X. Wang, B. Ding, B. Li, Biomimetic electrospun nanofibrous structures for tissue engineering, *Mater Today*, 16 (2013), 229.

[112] D.-G. Yu, X.-Y. Li, X. Wang, J.-H. Yang, S. A. Bligh, G. R. Williams, Nanofibers fabricated using triaxial electrospinning as zero order drug delivery systems, *ACS applied materials & interfaces*, 7 (2015), 18891.

[113] S. T. Yohe, J. A. Kopechek, T. M. Porter, Y. L. Colson, M. W. Grinstaff, Triggered Drug Release from Superhydrophobic Meshes using High-Intensity Focused Ultrasound, *Advanced healthcare materials*, 2 (2013), 1204.

[114] L. Sun, W. Gao, X. Fu, M. Shi, W. Xie, W. Zhang, F. Zhao, X. Chen, Enhanced wound healing in diabetic rats by nanofibrous scaffolds mimicking the basketweave pattern of collagen fibrils in native skin, *Biomaterials science*, 6 (2018), 340.

[115] P. Pal, P. K. Srivas, P. Dadhich, B. Das, D. Maulik, S. Dhara, Nano-/microfibrous cotton-wool-like 3D scaffold with core-shell architecture by emulsion electrospinning for skin tissue regeneration, *ACS Biomaterials Science & Engineering*, 3 (2017), 3563.

[116] B. Ma, J. Xie, J. Jiang, J. Wu, Sandwich-type fiber scaffolds with square arrayed microwells and nanostructured cues as microskin grafts for skin regeneration, *Biomaterials*, 35 (2014), 630.

[117] E. J. Lee, B. K. Huh, S. N. Kim, J. Y. Lee, C. G. Park, A. G. Mikos, Y. B. Choy, Application of materials as medical devices with localized drug delivery capabilities for enhanced wound repair, *Prog Mater Sci*, 89 (2017), 392.

1 Introduction

- [118] P. M. Hergenrother, The use, design, synthesis, and properties of high performance/high temperature polymers: an overview, *High Perform Polym*, 15 (2003), 3.
- [119] M. Afshari, D. J. Sikkema, K. Lee, M. Bogle, High performance fibers based on rigid and flexible polymers, *Polymer Reviews*, 48 (2008), 230.
- [120] S. Bourbigot, X. Flambard, Heat resistance and flammability of high performance fibres: A review, *Fire and materials*, 26 (2002), 155.
- [121] R. Van Deusen, Benzimidazo-benzophenanthroline polymers, *Journal of Polymer Science Part B: Polymer Letters*, 4 (1966), 211.
- [122] R. Van Deusen, O. Goins, A. Sicree, Thermally stable polymers from 1, 4, 5, 8-naphthalenetetracarboxylic acid and aromatic tetraamines, *Journal of Polymer Science Part A-1: Polymer Chemistry*, 6 (1968), 1777.
- [123] G. Berry, M. Murakami, Thermal–mechanical studies on a heterocyclic polymer (BBB). II. Dynamic mechanical studies at elevated temperatures, *Journal of Polymer Science: Polymer Physics Edition*, 14 (1976), 1721.
- [124] G. Berry, Thermal–mechanical studies on a heterocyclic polymer (BBB). I. Tensile creep and recovery, *Journal of Polymer Science: Polymer Physics Edition*, 14 (1976), 451.
- [125] M. Ballauff, Stiff-Chain Polymers—Structure, Phase Behavior, and Properties, *Angewandte Chemie International Edition in English*, 28 (1989), 253.
- [126] M. Ballauff, Stiff-chain polymers—structure, phase behavior, and properties, *Angewandte Chemie International Edition in English*, 28 (1989), 253.
- [127] N. Li, S. Zhang, J. Liu, F. Zhang, Synthesis and properties of sulfonated poly [bis (benzimidazobenzisoquinolinones)] as hydrolytically and thermooxidatively stable proton conducting ionomers, *Macromolecules*, 41 (2008), 4165.
- [128] S. A. Jenekhe, P. O. Johnson, Complexation-mediated solubilization and processing of rigid-chain and ladder polymers in aprotic organic solvents, *Macromolecules*, 23 (1990), 4419.
- [129] M. F. Roberts, S. A. Jenekhe, Lewis acid coordination complexes of polymers: 3. Poly (benzobisimidazobenzophenanthroline) ladder and semiladder polymers, *Polymer*, 35 (1994), 4313.

1 Introduction

- [130] M. Wagner, A. Österholm, S. P. Hirvonen, H. Tenhu, A. Ivaska, C. Kvarnström, Characterization of Water-Dispersible n-Type Poly (benzimidazobenzophenanthroline) Derivatives, *Macromol Chem Phys*, 212 (2011), 1567.
- [131] M. Salomäki, O. Jaakkola, S.-P. Hirvonen, H. Tenhu, C. Kvarnström, Highly controllable ambient atmosphere spray deposition of water dispersible poly (benzimidazobenzophenanthroline) films, *Synth Met*, 245 (2018), 144.
- [132] J. Lindle, F. Bartoli, C. Hoffman, O. K. Kim, Y. Lee, J. Shirk, Z. Kafafi, Nonlinear optical properties of benzimidazobenzophenanthroline type ladder polymers, *Appl Phys Lett*, 56 (1990), 712.
- [133] M. M. Alam, S. A. Jenekhe, Conducting ladder polymers: insulator-to-metal transition and evolution of electronic structure upon protonation by poly (styrenesulfonic acid), *The Journal of Physical Chemistry B*, 106 (2002), 11172.
- [134] K. Narayan, A. Alagiriswamy, R. Spry, dc transport studies of poly (benzimidazobenzophenanthroline) a ladder-type polymer, *Physical Review B*, 59 (1999), 10054.
- [135] D. Davidov, I. Belaish, C. Rettori, M. R. McLean, L. R. Dalton, High intrinsic conductivity in ladder type polymers: Pyrolyzed BBB, *Polym Adv Technol*, 1 (1990), 181.
- [136] O. K. Kim, Electrical conductivity of heteroaromatic ladder polymers, *Journal of Polymer Science: Polymer Letters Edition*, 20 (1982), 663.
- [137] A. Babel, S. A. Jenekhe, High electron mobility in ladder polymer field-effect transistors, *J Am Chem Soc*, 125 (2003), 13656.
- [138] S. A. Jenekhe, S. J. Tibbetts, Ion implantation doping and electrical properties of high-temperature ladder polymers, *J Polym Sci, Part B: Polym Phys*, 26 (1988), 201.
- [139] H. Song, A. Fratini, M. Chabinyk, G. Price, A. Agrawal, C.-S. Wang, J. Burkette, D. Dudis, F. Arnold, Crystal structure and thin film morphology of BBL ladder polymer, *Synth Met*, 69 (1995), 533.
- [140] A. L. Briseno, S. C. Mannsfeld, P. J. Shamberger, F. S. Ohuchi, Z. Bao, S. A. Jenekhe, Y. Xia, Self-assembly, molecular packing, and electron transport in n-type polymer semiconductor nanobelts, *Chem Mater*, 20 (2008), 4712.

1 Introduction

- [141] A. L. Briseno, F. S. Kim, A. Babel, Y. Xia, S. A. Jenekhe, n-Channel polymer thin film transistors with long-term air-stability and durability and their use in complementary inverters, *J Mater Chem*, 21 (2011), 16461.
- [142] S. A. Jenekhe, S. Yi, Efficient photovoltaic cells from semiconducting polymer heterojunctions, *Appl Phys Lett*, 77 (2000), 2635.
- [143] D. Papkov, Y. Zou, M. N. Andalib, A. Goponenko, S. Z. Cheng, Y. A. Dzenis, Simultaneously strong and tough ultrafine continuous nanofibers, *ACS nano*, 7 (2013), 3324.
- [144] S. Lee, A. R. Cho, D. Park, J. K. Kim, K. S. Han, I.-J. Yoon, M. H. Lee, J. Nah, Reusable Polybenzimidazole Nanofiber Membrane Filter for Highly Breathable PM2.5 Dust Proof Mask, *ACS applied materials & interfaces*, 11 (2019), 2750.
- [145] G. Srinivasan, D. H. Reneker, Structure and morphology of small diameter electrospun aramid fibers, *Polym Int*, 36 (1995), 195.
- [146] J. Yao, J. Jin, E. Lepore, N. M. Pugno, C. W. Bastiaansen, T. Peijs, Electrospinning of p-Aramid Fibers, *Macromolecular Materials and Engineering*, 300 (2015), 1238.
- [147] L. Yao, C. Lee, J. Kim, Fabrication of electrospun meta-aramid nanofibers in different solvent systems, *Fibers and Polymers*, 11 (2010), 1032.
- [148] J. Yoon, S. K. Chae, J.-M. Kim, Colorimetric sensors for volatile organic compounds (VOCs) based on conjugated polymer-embedded electrospun fibers, *J Am Chem Soc*, 129 (2007), 3038.
- [149] H. Zhang, S. Jiang, G. Duan, J. Li, K. Liu, C. Zhou, H. Hou, Heat-resistant polybenzoxazole nanofibers made by electrospinning, *Eur Polym J*, 50 (2014), 61.
- [150] S. Jiang, G. Duan, L. Chen, X. Hu, Y. Ding, C. Jiang, H. Hou, Thermal, mechanical and thermomechanical properties of tough electrospun poly (imide-co-benzoxazole) nanofiber belts, *New J Chem*, 39 (2015), 7797.
- [151] S. Jiang, S. Agarwal, A. Greiner, Low-Density Open Cellular Sponges as Functional Materials, *Angew Chem Int Ed*, 56 (2017), 15520.
- [152] X. Gui, J. Wei, K. Wang, A. Cao, H. Zhu, Y. Jia, Q. Shu, D. Wu, Carbon nanotube sponges, *Adv Mater*, 22 (2010), 617.

1 Introduction

- [153] H. Sun, Z. Xu, C. Gao, Multifunctional, ultra-flyweight, synergistically assembled carbon aerogels, *Adv Mater*, 25 (2013), 2554.
- [154] H. Bi, Z. Yin, X. Cao, X. Xie, C. Tan, X. Huang, B. Chen, F. Chen, Q. Yang, X. Bu, Carbon fiber aerogel made from raw cotton: a novel, efficient and recyclable sorbent for oils and organic solvents, *Adv Mater*, 25 (2013), 5916.
- [155] S. C. Li, B. C. Hu, Y. W. Ding, H. W. Liang, C. Li, Z. Y. Yu, Z. Y. Wu, W. S. Chen, S. H. Yu, Wood-Derived Ultrathin Carbon Nanofiber Aerogels, *Angew Chem Int Ed*, 57 (2018), 7085.
- [156] Z. Y. Wu, C. Li, H. W. Liang, J. F. Chen, S. H. Yu, Ultralight, flexible, and fire-resistant carbon nanofiber aerogels from bacterial cellulose, *Angew Chem Int Ed*, 52 (2013), 2925.
- [157] Y. Si, J. Yu, X. Tang, J. Ge, B. Ding, Ultralight nanofibre-assembled cellular aerogels with superelasticity and multifunctionality, *Nature communications*, 5 (2014), 5802.
- [158] S. Jiang, B. Uch, S. Agarwal, A. Greiner, Ultralight, thermally insulating, compressible polyimide fiber assembled sponges, *ACS applied materials & interfaces*, 9 (2017), 32308.
- [159] M. Mader, V. r. Jérôme, R. Freitag, S. Agarwal, A. Greiner, Ultraporous, compressible, wettable polylactide/polycaprolactone sponges for tissue engineering, *Biomacromolecules*, 19 (2018), 1663.
- [160] T. Xu, J. M. Miszuk, Y. Zhao, H. Sun, H. Fong, Electrospun polycaprolactone 3D nanofibrous scaffold with interconnected and hierarchically structured pores for bone tissue engineering, *Advanced healthcare materials*, 4 (2015), 2238.
- [161] F. Deuber, S. Mousavi, M. Hofer, C. Adlhart, Tailoring pore structure of ultralight electrospun sponges by solid templating, *ChemistrySelect*, 1 (2016), 5595.
- [162] G. Duan, S. Jiang, V. Jérôme, J. H. Wendorff, A. Fathi, J. Uhm, V. Altstädt, M. Herling, J. Breu, R. Freitag, Ultralight, soft polymer sponges by self-assembly of short electrospun fibers in colloidal dispersions, *Adv Funct Mater*, 25 (2015), 2850.
- [163] S. Jiang, S. Reich, B. Uch, P. Hu, S. Agarwal, A. Greiner, Exploration of the electrical conductivity of double-network silver nanowires/polyimide porous low-density compressible sponges, *ACS applied materials & interfaces*, 9 (2017), 34286.
- [164] Z. Qian, Z. Wang, Y. Chen, S. Tong, M. Ge, N. Zhao, J. Xu, Superelastic and ultralight

1 Introduction

polyimide aerogels as thermal insulators and particulate air filters, *Journal of Materials Chemistry A*, 6 (2018), 828.

[165] Z. Qian, M. Yang, R. Li, D. Li, J. Zhang, Y. Xiao, C. Li, R. Yang, N. Zhao, J. Xu, Fire-resistant, ultralight, superelastic and thermally insulated polybenzazole aerogels, *Journal of Materials Chemistry A*, 6 (2018), 20769.

[166] P. Mu, W. Bai, Z. Zhang, J. He, H. Sun, Z. Zhu, W. Liang, A. Li, Robust aerogels based on conjugated microporous polymer nanotubes with exceptional mechanical strength for efficient solar steam generation, *Journal of Materials Chemistry A*, 6 (2018), 18183.

[167] C.-W. Chiu, J.-J. Lin, Self-assembly behavior of polymer-assisted clays, *Prog Polym Sci*, 37 (2012), 406.

[168] T. J. Pinnavaia, Intercalated clay catalysts, *Science*, 220 (1983), 365.

[169] R. Celis, M. C. Hermosín, M. J. Carrizosa, J. Cornejo, Inorganic and organic clays as carriers for controlled release of the herbicide hexazinone, *J Agric Food Chem*, 50 (2002), 2324.

[170] Z. Kiraly, B. Veisz, A. Mastalir, G. Köfaragó, Preparation of ultrafine palladium particles on cationic and anionic clays, mediated by oppositely charged surfactants: catalytic probes in hydrogenations, *Langmuir*, 17 (2001), 5381.

[171] C.-H. Zhou, Z.-F. Shen, L.-H. Liu, S.-M. Liu, Preparation and functionality of clay-containing films, *J Mater Chem*, 21 (2011), 15132.

[172] M. W. Möller, T. Lunkenbein, H. Kalo, M. Schieder, D. A. Kunz, J. Breu, Barrier Properties of Synthetic Clay with a Kilo-Aspect Ratio, *Adv Mater*, 22 (2010), 5245.

[173] M. Stöter, D. A. Kunz, M. Schmidt, D. Hirsemann, H. Kalo, B. Putz, J. r. Senker, J. Breu, Nanoplatelets of sodium hectorite showing aspect ratios of $\approx 20\,000$ and superior purity, *Langmuir*, 29 (2013), 1280.

[174] H. Kalo, M. W. Möller, M. Ziadeh, D. Dolejš, J. Breu, Large scale melt synthesis in an open crucible of Na-fluorohectorite with superb charge homogeneity and particle size, *Applied Clay Science*, 48 (2010), 39.

[175] X. Wang, E. N. Kalali, J.-T. Wan, D.-Y. Wang, Carbon-family materials for flame retardant polymeric materials, *Prog Polym Sci*, 69 (2017), 22.

1 Introduction

- [176] A. Dasari, Z.-Z. Yu, G.-P. Cai, Y.-W. Mai, Recent developments in the fire retardancy of polymeric materials, *Prog Polym Sci*, 38 (2013), 1357.
- [177] P. Kiliaris, C. Papaspyrides, Polymer/layered silicate (clay) nanocomposites: an overview of flame retardancy, *Prog Polym Sci*, 35 (2010), 902.
- [178] B. Yuan, Y. Sun, X. Chen, Y. Shi, H. Dai, S. He, Poorly-/well-dispersed graphene: Abnormal influence on flammability and fire behavior of intumescent flame retardant, *Composites Part A: Applied Science and Manufacturing*, 109 (2018), 345.
- [179] F. Laoutid, L. Bonnaud, M. Alexandre, J.-M. Lopez-Cuesta, P. Dubois, New prospects in flame retardant polymer materials: from fundamentals to nanocomposites, *Materials science and engineering: R: Reports*, 63 (2009), 100.
- [180] H. Horacek, R. Grabner, Advantages of flame retardants based on nitrogen compounds, *Polym Degrad Stab*, 54 (1996), 205.
- [181] G. Stieger, M. Scheringer, C. A. Ng, K. Hungerbühler, Assessing the persistence, bioaccumulation potential and toxicity of brominated flame retardants: Data availability and quality for 36 alternative brominated flame retardants, *Chemosphere*, 116 (2014), 118.
- [182] G.-L. Wei, D.-Q. Li, M.-N. Zhuo, Y.-S. Liao, Z.-Y. Xie, T.-L. Guo, J.-J. Li, S.-Y. Zhang, Z.-Q. Liang, Organophosphorus flame retardants and plasticizers: sources, occurrence, toxicity and human exposure, *Environ Pollut*, 196 (2015), 29.
- [183] I. Van der Veen, J. de Boer, Phosphorus flame retardants: properties, production, environmental occurrence, toxicity and analysis, *Chemosphere*, 88 (2012), 1119.
- [184] J. W. Gilman, C. L. Jackson, A. B. Morgan, R. Harris, E. Manias, E. P. Giannelis, M. Wuthenow, D. Hilton, S. H. Phillips, Flammability properties of polymer– layered-silicate nanocomposites. Polypropylene and polystyrene nanocomposites, *Chem Mater*, 12 (2000), 1866.
- [185] P. Das, H. Thomas, M. Moeller, A. Walther, Large-scale, thick, self-assembled, nacre-mimetic brick-walls as fire barrier coatings on textiles, *Scientific reports*, 7 (2017), 39910.
- [186] H.-B. Chen, P. Shen, M.-J. Chen, H.-B. Zhao, D. A. Schiraldi, Highly efficient flame retardant polyurethane foam with alginate/clay aerogel coating, *ACS applied materials & interfaces*, 8 (2016), 32557.

1 Introduction

- [187] A. Walther, I. Bjurhager, J. M. Malho, J. Ruokolainen, L. Berglund, O. Ikkala, Supramolecular control of stiffness and strength in lightweight high-performance nacre-mimetic paper with fire-shielding properties, *Angew Chem Int Ed*, 49 (2010), 6448.
- [188] G. Wen, Z. Guo, Nonflammable superhydrophobic paper with biomimetic layered structure exhibiting boiling-water resistance and repairable properties for emulsion separation, *Journal of Materials Chemistry A*, 6 (2018), 7042.
- [189] F. Carosio, J. Kochumalayil, A. Fina, L. A. Berglund, Extreme thermal shielding effects in nanopaper based on multilayers of aligned clay nanoplatelets in cellulose nanofiber matrix, *Advanced Materials Interfaces*, 3 (2016), 1600551.
- [190] G.-G. Chen, Y.-J. Hu, F. Peng, J. Bian, M.-F. Li, C.-L. Yao, R.-C. Sun, Fabrication of strong nanocomposite films with renewable forestry waste/montmorillonite/reduction of graphene oxide for fire retardant, *Chem Eng J*, 337 (2018), 436.
- [191] H.-B. Chen, Y. Zhao, P. Shen, J.-S. Wang, W. Huang, D. A. Schiraldi, Effects of molecular weight upon irradiation-cross-linked poly (vinyl alcohol)/clay aerogel properties, *ACS applied materials & interfaces*, 7 (2015), 20208.
- [192] H.-B. Chen, B. Liu, W. Huang, J.-S. Wang, G. Zeng, W.-H. Wu, D. A. Schiraldi, Fabrication and properties of irradiation-cross-linked poly (vinyl alcohol)/clay aerogel composites, *ACS applied materials & interfaces*, 6 (2014), 16227.
- [193] H. Sun, D. A. Schiraldi, D. Chen, D. Wang, M. Sánchez-Soto, Tough polymer aerogels incorporating a conformal inorganic coating for low flammability and durable hydrophobicity, *ACS applied materials & interfaces*, 8 (2016), 13051.
- [194] T. Wang, H. Sun, J. Long, Y.-Z. Wang, D. Schiraldi, Biobased poly (furfuryl alcohol)/clay aerogel composite prepared by a freeze-drying process, *ACS Sustainable Chemistry & Engineering*, 4 (2016), 2601.
- [195] K. Shang, W. Liao, J. Wang, Y.-T. Wang, Y.-Z. Wang, D. A. Schiraldi, Nonflammable alginate nanocomposite aerogels prepared by a simple freeze-drying and post-cross-linking method, *ACS applied materials & interfaces*, 8 (2015), 643.
- [196] S. Bourbigot, S. Duquesne, Fire retardant polymers: recent developments and

1 Introduction

opportunities, *J Mater Chem*, 17 (2007), 2283.

[197] A. Arora, G. Padua, Nanocomposites in food packaging, *J Food Sci*, 75 (2010), R43.

[198] J. Lewis, Material challenge for flexible organic devices, *Mater Today*, 9 (2006), 38.

[199] S. Logothetidis, Flexible organic electronic devices: Materials, process and applications, *Materials Science and Engineering: B*, 152 (2008), 96.

[200] J. Lange, Y. Wyser, Recent innovations in barrier technologies for plastic packaging—a review, *Packaging Technology and Science: An International Journal*, 16 (2003), 149.

[201] E. Cussler, S. E. Hughes, W. J. Ward III, R. Aris, Barrier membranes, *Journal of Membrane Science*, 38 (1988), 161.

[202] M. W. Mödler, D. A. Kunz, T. Lunkenbein, S. Sommer, A. Nennemann, J. Breu, UV-cured, flexible, and transparent nanocomposite coating with remarkable oxygen barrier, *Adv Mater*, 24 (2012), 2142.

[203] G. Choudalakis, A. Gotsis, Permeability of polymer/clay nanocomposites: a review, *Eur Polym J*, 45 (2009), 967.

[204] H.-L. Tyan, Y.-C. Liu, K.-H. Wei, Thermally and mechanically enhanced clay/polyimide nanocomposite via reactive organoclay, *Chem Mater*, 11 (1999), 1942.

[205] Y.-L. Liu, Y. Li, J.-T. Xu, Z.-Q. Fan, Cooperative effect of electrospinning and nanoclay on formation of polar crystalline phases in poly (vinylidene fluoride), *ACS applied materials & interfaces*, 2 (2010), 1759.

[206] P. Das, J.-M. Malho, K. Rahimi, F. H. Schacher, B. Wang, D. E. Demco, A. Walther, Nacre-mimetics with synthetic nanoclays up to ultrahigh aspect ratios, *Nature communications*, 6 (2015), 5967.

[207] J. Feng, X. Hu, P. L. Yue, Discoloration and mineralization of Orange II by using a bentonite clay-based Fe nanocomposite film as a heterogeneous photo-Fenton catalyst, *Water Res*, 39 (2005), 89.

[208] N.-o. Saelim, R. Magaraphan, T. Sreethawong, TiO₂/modified natural clay semiconductor as a potential electrode for natural dye-sensitized solar cell, *Ceram Int*, 37 (2011), 659.

1 Introduction

- [209] E. Doblhofer, J. Schmid, M. Rieß, M. Daab, M. Suntinger, C. Habel, H. Bargel, C. Hugenschmidt, S. Rosenfeldt, J. Breu, Structural Insights into Water-Based Spider Silk Protein–Nanoclay Composites with Excellent Gas and Water Vapor Barrier Properties, *ACS applied materials & interfaces*, 8 (2016), 25535.
- [210] D. A. Kunz, J. Schmid, P. Feicht, J. Erath, A. Fery, J. Breu, Clay-based nanocomposite coating for flexible optoelectronics applying commercial polymers, *ACS nano*, 7 (2013), 4275.
- [211] C. Habel, M. Schötle, M. Daab, N. J. Eichstaedt, D. Wagner, H. Bakhshi, S. Agarwal, M. A. Horn, J. Breu, High-Barrier, Biodegradable Food Packaging, *Macromolecular Materials and Engineering*, 303 (2018), 1800333.
- [212] M. A. Priolo, D. Gamboa, J. C. Grunlan, Transparent clay–polymer nano brick wall assemblies with tailorable oxygen barrier, *ACS Applied Materials & Interfaces*, 2 (2009), 312.
- [213] M. A. Priolo, K. M. Holder, D. Gamboa, J. C. Grunlan, Influence of clay concentration on the gas barrier of clay–polymer nanobrick wall thin film assemblies, *Langmuir*, 27 (2011), 12106.
- [214] D. Y. Takamoto, E. Aydil, J. A. Zasadzinski, A. T. Ivanova, D. K. Schwartz, T. Yang, P. S. Cremer, Stable ordering in Langmuir-Blodgett films, *Science*, 293 (2001), 1292.
- [215] R. H. Ras, Y. Umemura, C. T. Johnston, A. Yamagishi, R. A. Schoonheydt, Ultrathin hybrid films of clay minerals, *PCCP*, 9 (2007), 918.

2. An Overview of The Thesis

2. An Overview of The Thesis

Rigid-rod polymers, such as BBB, with ladder or semi-ladder conjugated structures have proven to be high strength, high modulus and high-temperature resistant, but the insolubility in common solvent and infusibility limit their processing and applications. The present studies have been carried out with the aim of processing BBB to nanofibres by electrospinning, assembling BBB nanofibres into 3D sponges and composite membranes incorporating layered silicate (Na-Hectorite). The results are presented in the form of a cumulative thesis with four published articles in peer-reviewed journals (**section 2.1 to 2.4**) as summarized in the following picture (**Figure 2-1**).

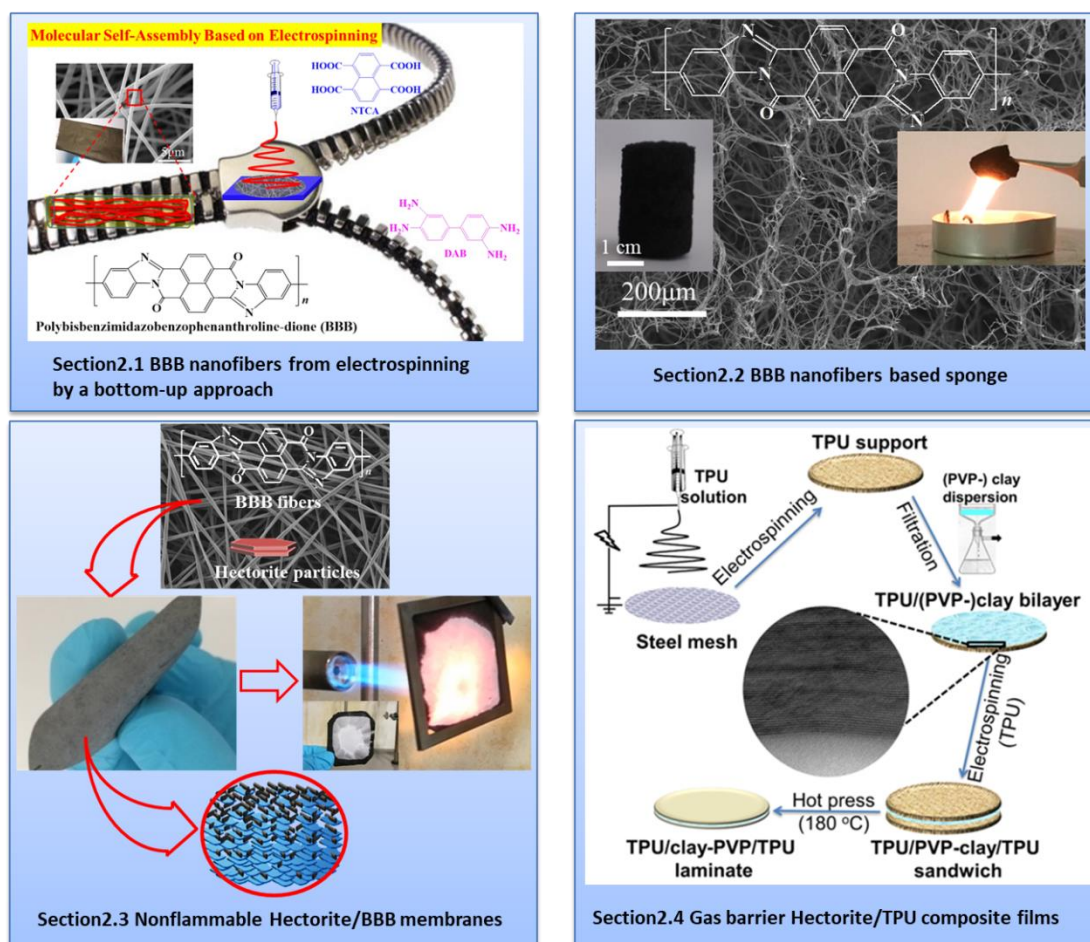


Figure 2-1. Pictorial summary of the prepared work as described in section 2.1-2.4.

The BBB nanofibres were prepared successfully for the first time using a bottom-up approach by electrospinning the corresponding monomers' solution with a template

2. An Overview of The Thesis

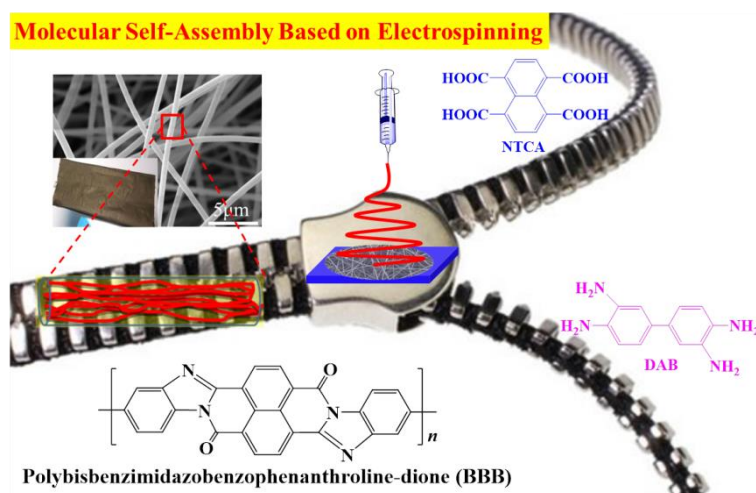
polymer (PVP) followed by solid-state polymerization of monomers at a high temperature and simultaneous pyrolysis of the template polymer. Details about the preparation procedures and characterizations are described in **section 2.1**. This part of work was started as my master's thesis and elaborated further together with Prof. Haoqing Hou, Jiangxi Normal University. In **section 2.2**, in order to expand the application of BBB nanofibres, the BBB short fibres were assembled into low-density 3D sponges. The structure, mechanical stability, intrinsic flame-retardant property and applications of BBB sponges in organic solvents uptake and thermal insulation were explored.

Furthermore, the composite porous membranes of BBB and layered silicate were studied for their preparation method and properties. Layered silicate, with great thermal stability and intrinsic flame-resistance, is considered as a processing additive for the preparation of low-density, flexible and non-flammable BBB membranes. In this section (**section 2.3**), the composite membranes were prepared via an upscalable vacuum-assisted filtration self-assembly process and their flame-resistant properties are studied.

In the last section (**section 2.4**), the unique gas barrier advantageous features of layered silicate and the specific hierarchical pore structure of electrospun membranes are combined together to make a flexible, strong and high gas-barrier membrane. This section aims to obtain a layered structured thin film with an independent compact clay-based nanocomposite layer embedded inside a polymer matrix. The final part of the work would provide a basis for making gas-barrier thin films using high-temperature polymers in the future. Detailed coverage of the experimental parts, results and discussions can be found in the appendix (**Chapter 5**).

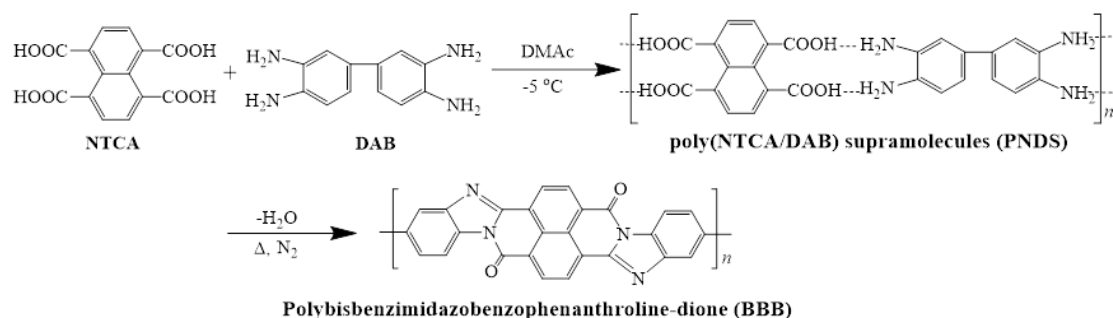
2. An Overview of The Thesis

2.1 Nanofibre Preparation of Non-processable Polymers by Solid-State Polymerization of Molecularly Self-Assembled Monomers



Jian Zhu, Yichun Ding, Seema Agarwal, Andreas Greiner, Hean Zhang and Haoqing Hou. Nanofibre preparation of non-processable polymers by solid-state polymerization of molecularly self-assembled monomers. *Nanoscale*, **2017**, 9(46), 18169-18174.

High-performance BBB is generally prepared by polycondensation of 3,3',4,4'-tetraaminobenzidine (DAB) and 1,4,5,8-naphthalene tetracarboxylic acid (NTCA) at a high temperature (**Scheme 2-1**).



Scheme 2-1. Synthetic scheme and chemical structure of the BBB polymer.

The BBB nanofibres were successfully prepared for the first time by a bottom-up approach using an electrospinning technique. The complete new procedure of BBB

2. An Overview of The Thesis

nanofibre formation includes two steps, as shown in **Figure 2-2**: 1) Electrospinning of monomers (DAB and NTCA) precursor fibres incorporating a high molecular weight sacrificial polymer (PVP was used) to assist the fibre formation; and 2) transforming the monomers to high molecular weight BBB in a solid state at a high temperature and pyrolysis, simultaneously with the sacrificial polymer. Using this approach, a random BBB nanofibre mat and aligned nanofibre belt were prepared by using a stationary plate and high-speed rotating collector, respectively.

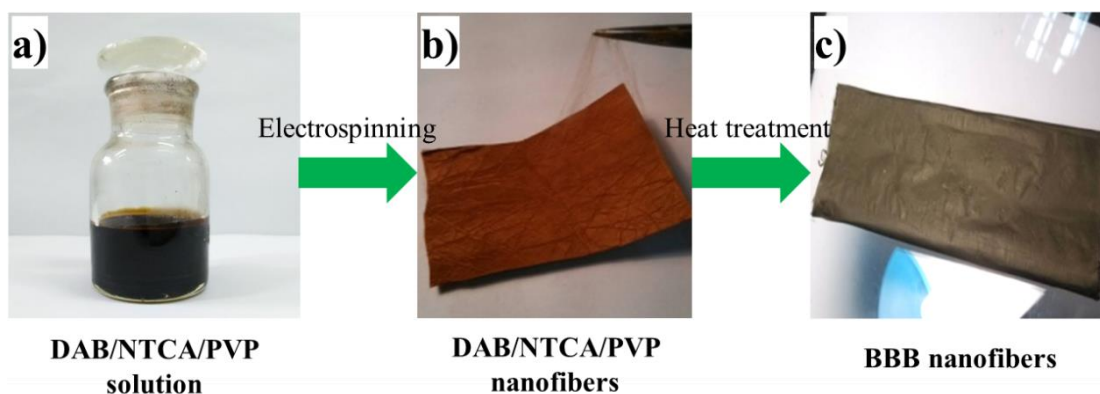


Figure 2-2. Procedure of the preparation of BBB nanofibres by electrospinning.

The formation of BBB on a template (PVP) fibre was followed by Fourier transform infrared spectroscopy (**Figure 2-3a**). The PVP characteristic absorptions at 1669 cm^{-1} (C=O stretching vibrations) and 2948 cm^{-1} (C-H stretching vibrations) disappeared. New peaks appeared at 1699 , 1616 , 1578 and 1547 cm^{-1} corresponding to the C=O, C=C, C=N and C–N vibrations attributed to BBB on heating above $400\text{ }^{\circ}\text{C}$. The formation of BBB took place through condensation of the intermediate structure, such as amide (structure **A**), imide (structure **B**) and benzimidazole (structure **C**) (**Figure 2-3b**).

2. An Overview of The Thesis

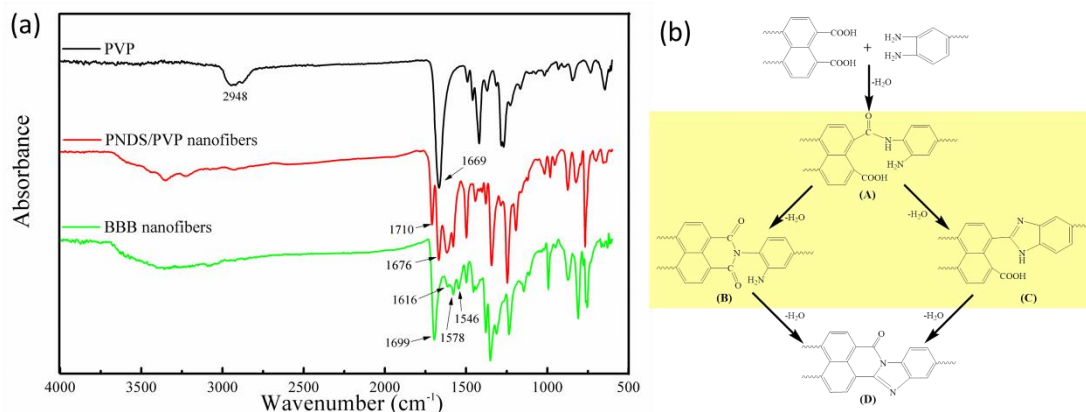


Figure 2-3. (a) Fourier transform infrared spectra of PVP, as-spun precursor nanofibres and BBB nanofibres. (b) Possible routes for the polymerization of NTCA and DAB to BBB.

The final BBB fibres are excellently thermal-resistant with the degradation onset temperature above 600 °C, and 5 % ($T_{5\%}$) and 10 % ($T_{10\%}$) weight loss temperatures of 641 °C and 698 °C, respectively, at N₂ atmosphere (**Figure 2-4a**). There is no clear glass transition temperature, as observed from the dynamic mechanical analysis measurement up to 500 °C. The morphology and diameter of BBB fibres were observed by scanning electron microscopy (SEM).

The effect of the amount of the template polymer and heat-treatment temperature on the mechanical properties of BBB nanofibre belts were studied systematically. The highest tensile strength (365 ± 5 MPa) was achieved for a BBB belt made from precursor PNDS and PVP (8:2) and a heat treatment at 500 °C. Furthermore, the strength could also be increased by hot-stretching of the fibres due to the molecular orientation (**Figure 2-4b**). The mechanical properties of individual BBB nanofibres were also investigated, and the results are shown in **Figure 2-4c** and **d**. Both the stress and modulus of single nanofibres increased with the decrease of the fibre diameter, similar to the observations in previous reports on other fibres, whereas the strain changes less with the fibre diameter.

2. An Overview of The Thesis

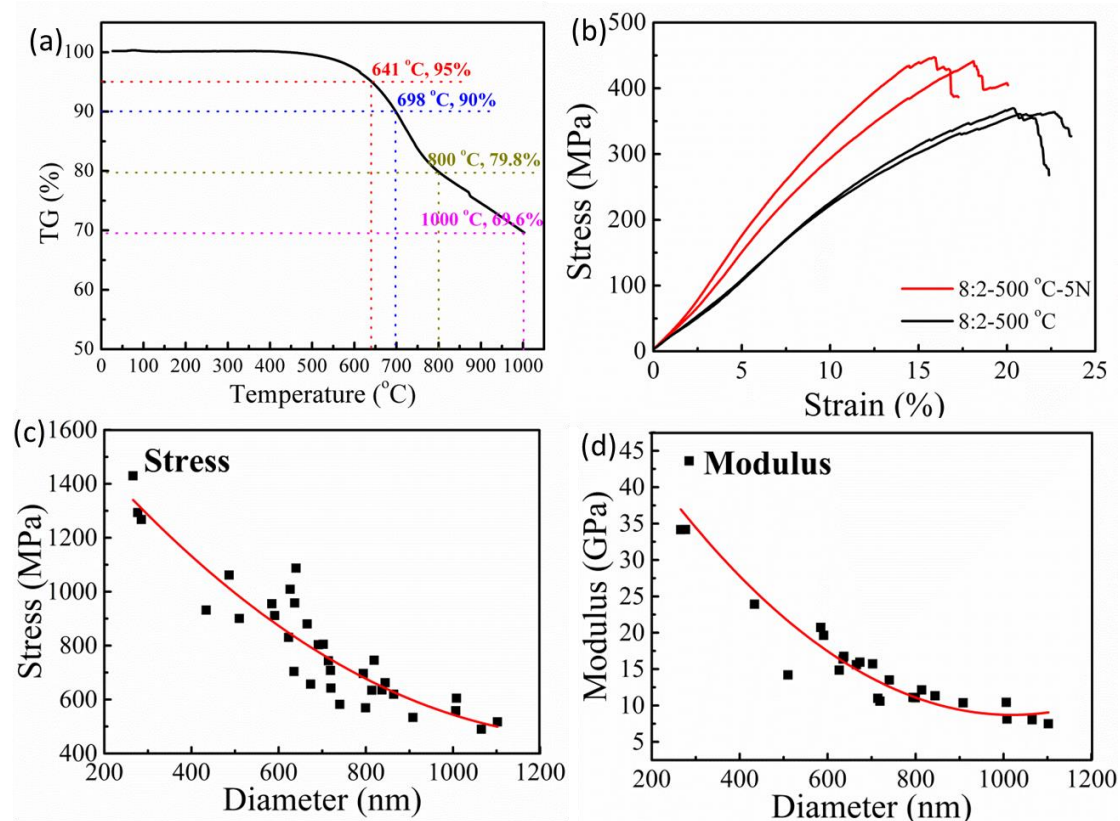
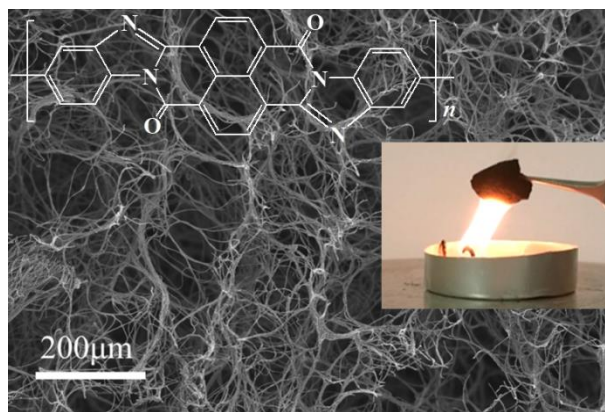


Figure 2-4. (a) TGA curve of BBB fibres and TGA curve of BBB nanofibres. (b) Stress-strain curves of the BBB nanofibre belt prepared without hot-stretching and with hot-stretching at 5 N. (c) Strength and (d) modulus of individual BBB nanofibres with different diameters (results from PNDS and PVP (8:2) and 500 °C treated sample).

In conclusion, high-strength, high moduli, high-temperature-resistant electrospun BBB nanofibres were prepared for the first time using a new strategy including monomers precursor electrospinning followed by solid polycondensation. The transformation process was confirmed by Fourier transform infrared spectroscopy. In the next sections the BBB fibres were used for making 3D sponges and porous composite membranes with layered silicate (Na-hectorite) with excellent thermal stability and non-flammability.

2. An Overview of The Thesis

2.2 Low-density, Thermally Stable and Intrinsic Flame-Retardant Poly(bis(benzimidazo)Benzophenanthrolinedione) Sponge



Jian Zhu, Shaohua Jiang, Haoqing Hou, Seema Agarwal, Andreas Greiner. Low Density, Thermally Stable, and Intrinsic Flame Retardant Poly (bis (benzimidazo) Benzophenanthroline-dione) Sponge. *Macromolecular Materials and Engineering*, **2018**, 303(4), 1700615.

In this part of the work, BBB fibres prepared in the previous section were used for the preparation of mechanically stable, low-density and compressible sponges with thermal stability, flame-retardant and thermal insulating properties. In order to prepare the sponges, the BBB fibres were mechanically cut to short fibres with a diameter of 700–800 nm and a length in the range of 50–500 μm (**Figure 2-5a, b**). The short fibre dispersion in water was freeze-dried to get a sponge with the hierarchically ordered dual pore structure (large pores more than 100 μm and small pores < 5–10 μm) (**Figure 2-5c, d**).

The use of a glue (PVA) was found to be critical for the stability of the sponges prepared. A systematic study showed the increase in the compressibility of the sponges upon use of PVA glue (**Figure 2-5e**). The sponges inherit the great thermal resistance of BBB polymer (**Figure 2-5f**). More than 95 % size recovery was achieved after a very high compression of 80 % which achieved about 90 % recovery after 50 cycles.

2. An Overview of The Thesis

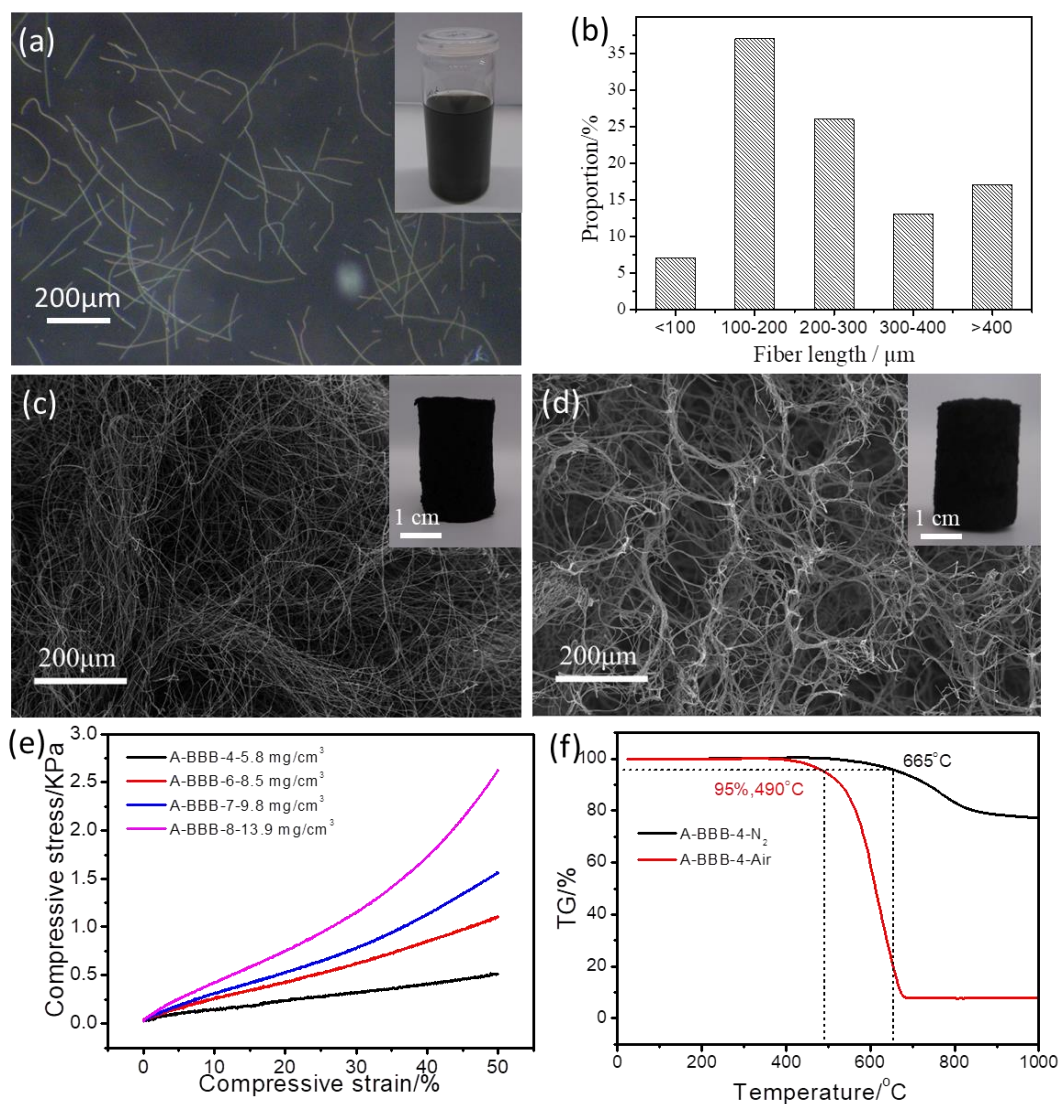


Figure 2-5. (a) Microphotograph of BBB short fibres. (b) Length distribution of BBB short fibres. (c) SEM images and photos of BBB sponge from pure water dispersion and (d) BBB sponge from PVA glue after annealing treatment. (e) Compression test of BBB sponge from PVA glue with different density. (f) TGA curves of BBB sponge in air and N₂ condition.

The sponges showed very low thermal conductivity ($0.028\text{--}0.038\text{ W mK}^{-1}$) depending upon the sponge density, which was measured by a Hot Disk Thermal Constants Analyzer (**Figure 2-6a, b**). The sponges showed very high sorption capacity (43–159 times their own weight) for organic solvents. The outstanding thermal isolation property of porosity polymer materials is also found identically in BBB sponges (**Figure 2-6c, d**). More importantly, the intrinsic flame-resistant property of BBB sponge was proven when

2. An Overview of The Thesis

neither a real ignition nor flaming combustion was observed when the sponge was placed on a naked flame (Figure 2-7).

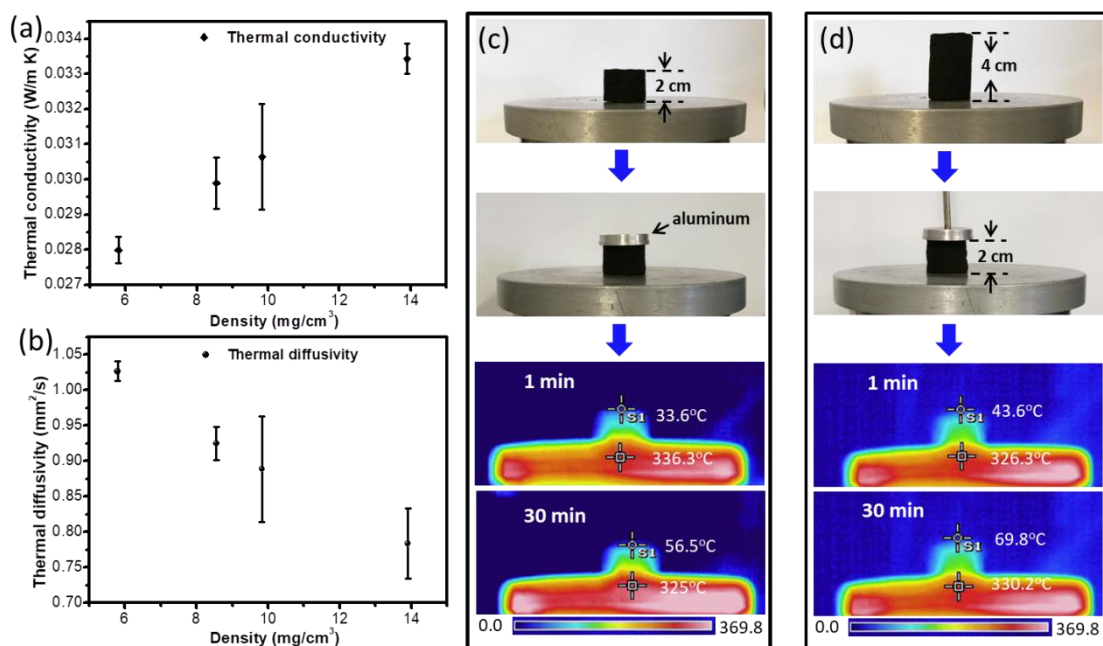


Figure 2-6. (a) Thermal conductivity and (b) thermal diffusivity of BBB sponge changes with density. (c) Digital photos and IR camera photos of BBB sponge and (d) 50 % compressed BBB sponge on a high-temperature plate.

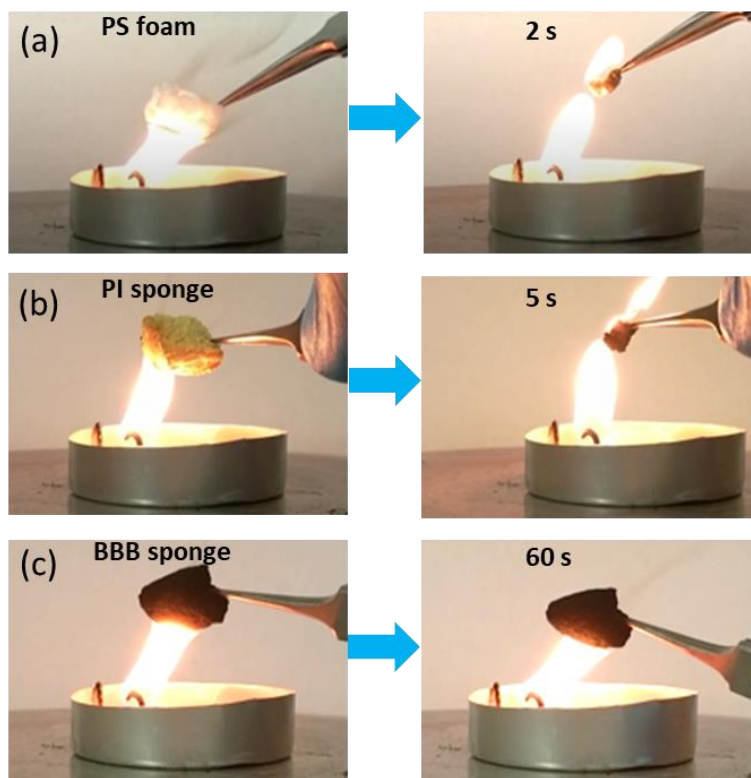


Figure 2-7. Photos of (a) polystyrene sponge, (b) PI sponge and (c) BBB sponge put on a naked

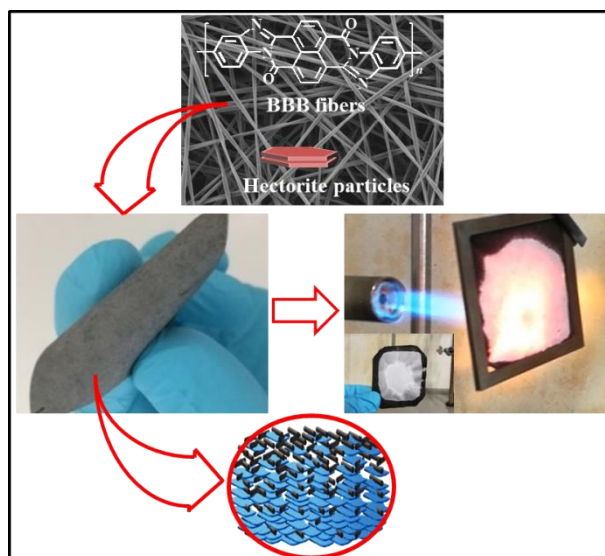
2. An Overview of The Thesis

flame.

In conclusion, BBB low-density ($\leq 13.9 \text{ mg cm}^{-3}$), compressible, elastic, intrinsic flame-retardant, thermally insulated sponges with high-temperature resistance were prepared to extend the application of BBB nanofibres. The sponge preparation required the use of a sacrificial glue, such as PVA, to help disperse the BBB fibres in water, self-assemble the pore structure hierarchically during FD, and finally enhance the mechanical stability. This sponge is quite suitable as insulation material in a harsh environment, such as a high temperature. Furthermore, short BBB fibres were used to make porous membranes by the wet-laid method. In this method, filtration of the short fibre dispersion through a filter leads to the random laying of fibres on top of each other due to percolation and provides a membrane. The BBB membrane prepared by this method was weak. Therefore, the work was continued with BBB/Na-hectorite composite membranes, as described in the next section.

2. An Overview of The Thesis

2.3 Gradient-Structured Non-flammable Flexible Polymer Membranes



Jian Zhu, Josef Breu, Haoqing Hou, Andreas Greiner, Seema Agarwal. Gradient structured non-flammable flexible polymer membranes. *ACS applied materials & interfaces*, **2019**, 11 (12), 11876-11883.

In this part of work, flexible composite membranes comprised of BBB short nanofibres and inorganic Na-hectorite (Hec) were fabricated by using a bottom-up vacuum-assisted self-assembly method with an aqueous dispersion of short BBB fibres and Hec (**Figure 2-8a**). Electrospun TPU was used as a filter. These membranes in addition to showing good mechanical properties, neither sustained flame, burnt with smoke nor showed melt dripping. Inhomogeneous distribution of Hec on the top and bottom of the membranes was observed from the SEM images. The Hec was primarily concentrated on the bottom side as a compact layer with all the fibres interconnected and covered by Hec nanosheets due to the larger density of Hec (**Figure 2-8b, c**). Cross-sectional SEM images and Si atom mapping, obtained by energy-dispersive X-ray spectrometry analysis (**Figures 2-8d, e**), confirmed the gradient distribution of Hec. There was an enhancement in the mechanical properties of the composite membranes due to the connection of BBB fibres through the flexible Hec nanosheets. The size of the Hec platelets ($\approx 20 \mu\text{m}$) is larger than the diameter of BBB fibre (700–800 nm) to cover many BBB fibres simultaneously. A

2. An Overview of The Thesis

detailed study was carried out by changing the ratio of Hec:BBB short fibres on membranes. Interestingly, membranes with a very high Hec content (82 wt.%) showed high modulus (237 ± 22 MPa) and flexibility (did not show cracks even after bending 10,000 times). The composite membranes exhibited a very high decomposition temperature (5 wt.% mass temperature 590–724 °C) and large residual mass at 800 °C (80–94 %), which confirmed the good stability. The thermal conductivities of the composite membranes studied were 15–51 mW m⁻¹K⁻¹, depending on the content of Hec.

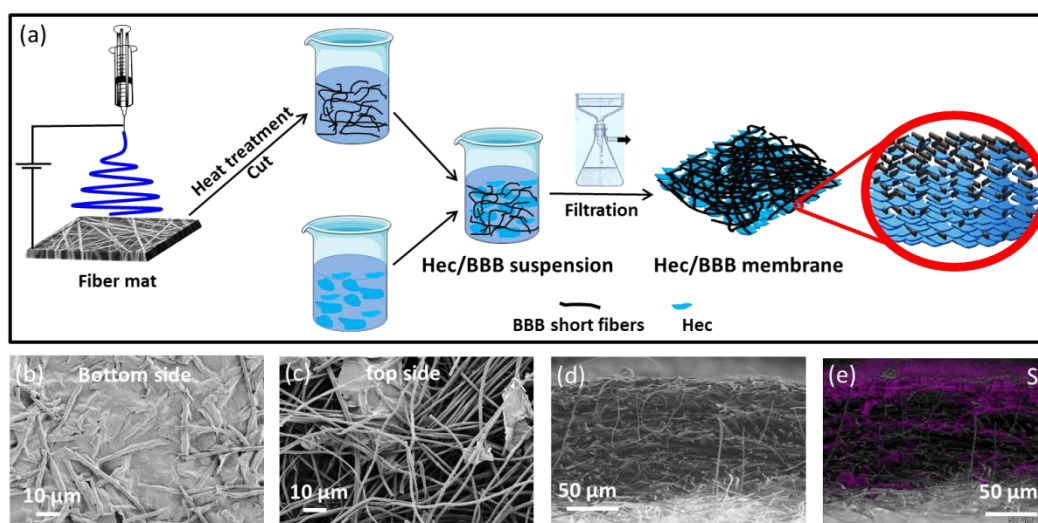


Figure 2-8. (a) Preparation process for the Hec/BBB membranes. SEM images of bottom (b) and top (c) side of the membrane of H-61/B-36 (61 and 36 is the percentage of Hec and BBB fibres). (d) SEM image of cross-section and (d) Si atom mapping obtained from energy-dispersive X-ray spectrometry of the H-61/B-36 membrane.

More importantly, the compact Hec layer at the bottom side avoids the hole formation of the composite membrane upon being subjected to the high-temperature flame (800 °C) (**Figure 2-9a**), thus, shielding the flame and protecting the cotton from burning (**Figure 2-9b**) even after a long period of heating (a minimum of 30 min). The flame was strengthened by using a high-temperature Campingaz burner (around 1400 °C) and still could not break the composite membrane to form a hole (**Figure 2-9c**). In addition, no sustained combustion of the Hec/BBB membranes was observed even when the membranes were ignited in a 100 % O₂ atmosphere (**Figure 2-9d**). No combustion or

2. An Overview of The Thesis

change in the samples before or after the cone calorimeter test was observed, reflecting the excellent flame-retardant properties (**Figure 2-9e**). No melt dripping was observed during any of the tests in this study.

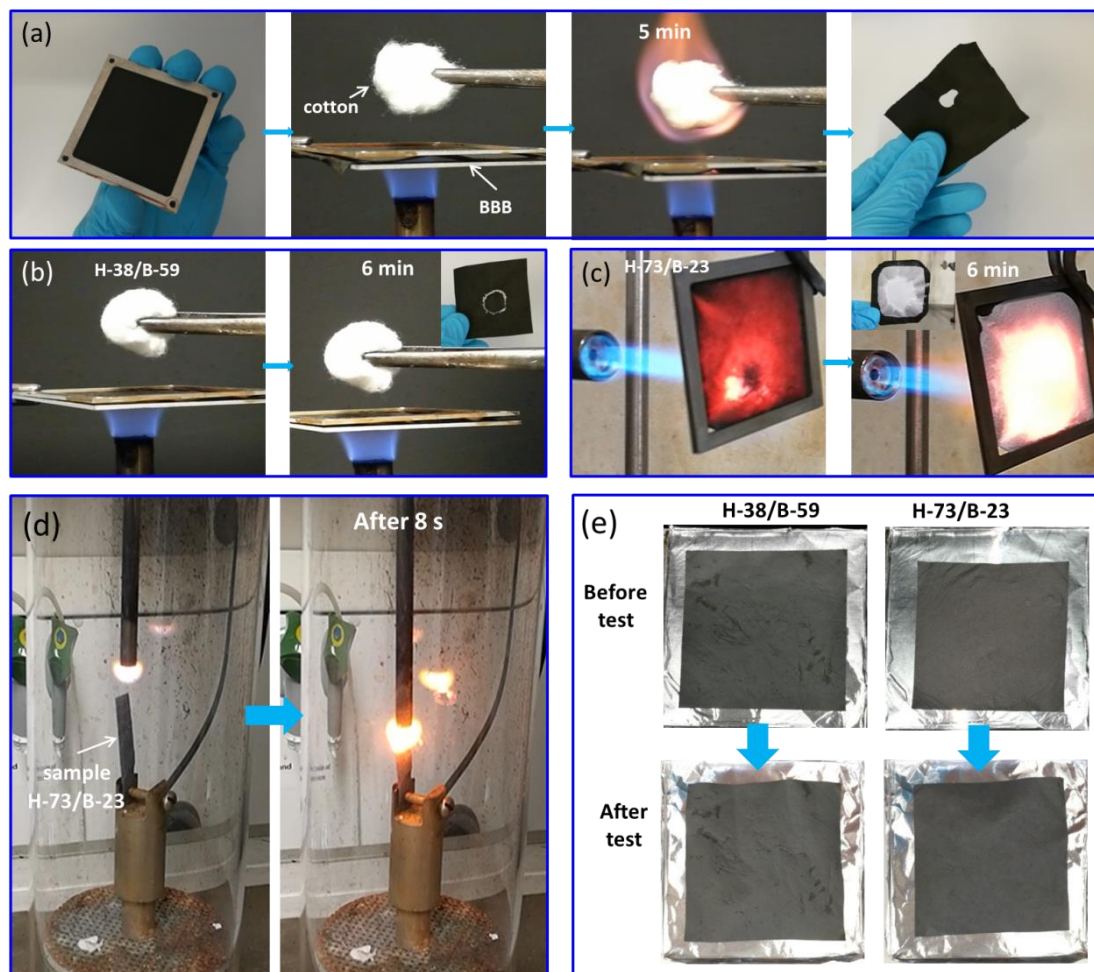


Figure 2-9. (a) Pure BBB fibre membrane fixed on a steel frame to shield the flame. (b) Cotton ball protected with the Hec/BBB composite membranes. Inset shows photos of the Hec/BBB membrane after the test. (c) Photos of the Hec/BBB membrane (H-73/B-23, 73 and 23 is the percentage of Hec and BBB fibres) placed on the flame of a Campingaz burner (1400 °C). (d) Ignition process for the Hec/BBB (H-73/B-23) membranes in a 100 % O₂ atmosphere. (e) Photos of the Hec/BBB membranes before and after the cone calorimeter test.

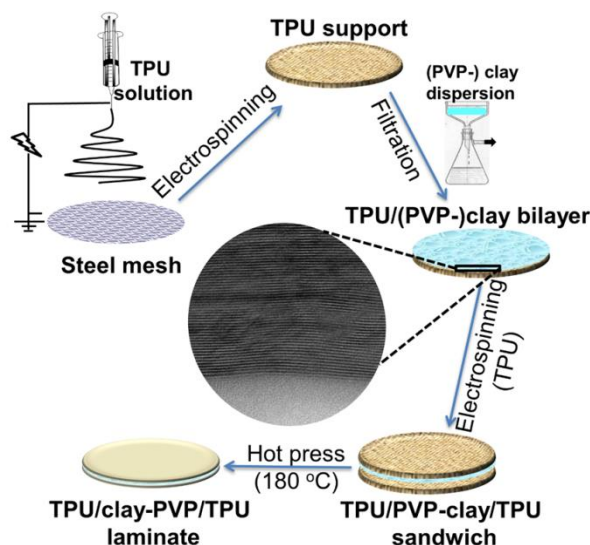
In conclusion, non-flammable gradient-structured composite membranes combining the advantages of BBB nanofibres and large aspect ratio Hec with a synergistic effect were prepared via an upscalable vacuum-assisted filtration process. Such low-density, flexible,

2. An Overview of The Thesis

mechanically strong, flame-retardant membranes are highly promising for use as lightweight construction materials and protective clothing. In the last part of the work, another method was established for making polymer-Hectorite composite membranes in a layer-by-layer structure. The studies related to it are detailed in the next section. The studies were carried out using TPU and layered silicates as model materials and can be extended easily to other high-performance polymers in the future.

2. An Overview of The Thesis

2.4 Filter-Through Method of Making Highly Efficient Polymer-Clay Nanocomposite Membranes



Jian Zhu, Christoph Habel, Theresa Schilling, Andreas Greiner, Josef Breu, Seema Agarwal. Filter-Through Method of Making Highly Efficient Polymer-Clay Nanocomposite Membranes, *Macromolecular Materials and Engineering*, **2019**, 1800779.

This part of the work deals with polymer-clay composite membranes of layer-by-layer type made by sandwiching layered silicates between two polymer membranes. Electrospun membranes with a hierarchical pore structure and variable pore diameter are used as filters for vacuum-assisted filtration of large aspect ratio layered silicate. In this work, layered structure, flexible, strong polymer films with enhanced gas-barrier properties were fabricated through coating clay-based nanocomposite (PVP-Hec) ultrathin layer on an electrospun thermoplastic porous support (a TPU mat) with the filtration method, followed by a hot press process (**Figure 2-10**). After filtration of PVP-Hec dispersion with a TPU mat as a filter, the PVP-Hec was coated on the surface of the TPU mat homogeneously (**Figure 2-11a, b**). The thickness of the coating layer can be controlled easily via changing the concentration of the dispersion. A sandwich-like transparent film was prepared by covering another TPU mat upon the coated mat and

2. An Overview of The Thesis

followed by a hot press to avoid the damage of the high content Hec nanocomposite layer and make it fit for the packaging application (**Figure 2-10c, d**).

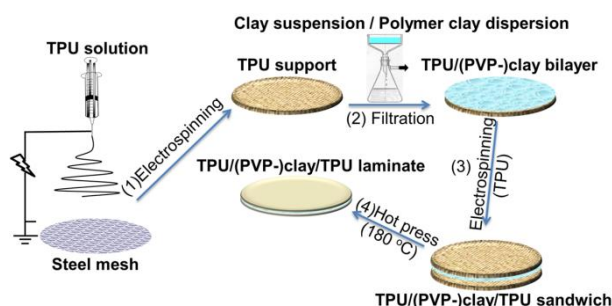


Figure 2-10. Fabrication procedure of TPU/PVP-Hec/TPU films.

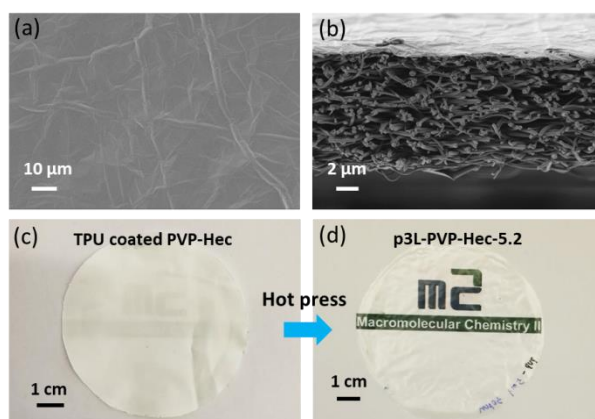


Figure 2-11. SEM images of the surface (a) and cross-section (b) of a PVP-Hec coated TPU mat.

Photos of the PVP-Hec coated with TPU mat (c) and three-layered film (d) after hot press.

The transmittance of the final films with a different thickness of the PVP-Hec layer inside is in the range of 60–80 % (**Figure 2-12a**). The Hec nanosheets with a highly aligned arrangement were confirmed by the X-ray diffraction (**Figure 2-12b**) patterns and transmission electron microscopy image (**Figure 2-12c**). An independent PVP-Hec nanocomposite layer embedded inside thin TPU films increases the elasticity modulus dramatically but does not lessen the strength much (**Figure 2-12d**). The thickness of the PVP-Hec layer is a prominent influence on the modulus (**Figure 2-12e**). Finally and most importantly, the O₂ barrier properties are greatly improved with the PVP-Hec nanocomposite layer inside compared to the pure TPU film due to the elongation of the

2. An Overview of The Thesis

tortuous path in the interlayer (**Figure 2-12f**).

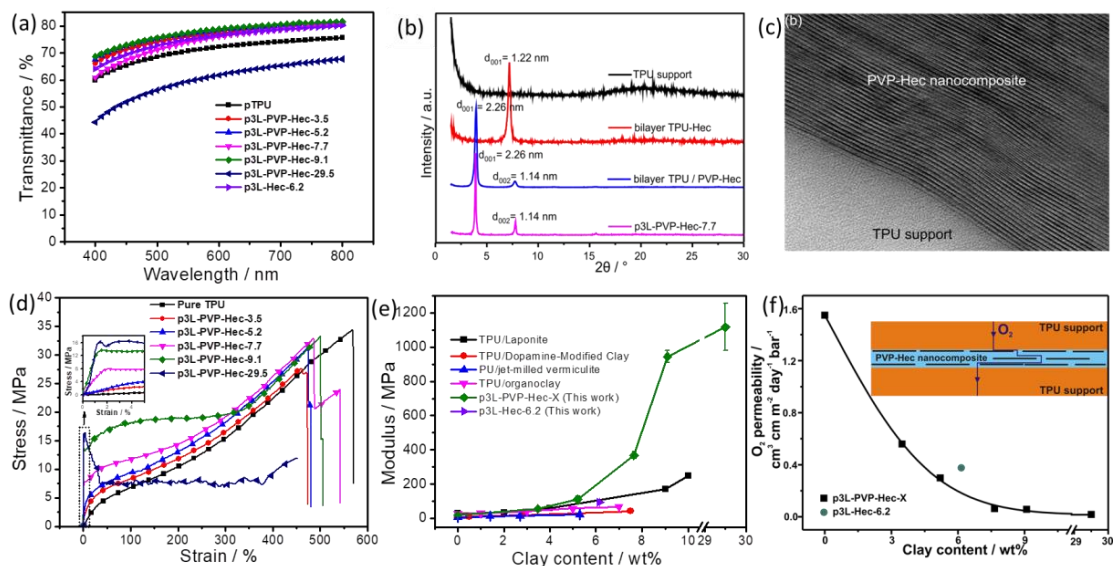


Figure 2-12. (a) The transmittances of the final laminate. (b) X-ray diffraction patterns of the neat pressed TPU support, Hec and PVP-Hec coated with TPU support, and the final hot-pressed laminate. (c) Transmission electron microscopy image of the alignment of the clay nanoplatelets in the interlayer PVP-Hec nanocomposite. (d) Stress-strain curves of final hot-pressed laminate. (e) Comparison of the elasticity modulus of the laminates of clay of this work and the TPU nanocomposites of other publications. (f) Oxygen permeability of final laminate membranes changes with amounts of Hec at 50 % RH. The “tortuous pathway” created by incorporation of delaminated Hec nanosheets into a PVP matrix is also illustrated.

In conclusion, we propose a scalable, fast and simple processing method here of coating a nanosheets layer on an electrospun support by filtration which enables the fabrication of lightweight barrier membranes. Depending on the variation of electrospun porous supports and diversity of the functional modification of coated nanosheets layer, this method offers flexibility regarding the overall performance of the resulting barrier membranes. The resulting flexible composite membranes are strong, transparent and show enhanced gas-barrier properties.

3. Outlook

3. Outlook

High-strength, high modulus, high-temperature stable, and flame-resistance polymer films, fibres and composite materials are always greatly required in the fields of the aerospace industry, electronic engineering, protective clothing and the automobile industry. Many polymers possessing this unique performance are limited in real application because of their processing problems. In this thesis, we show for the first time a new procedure of preparation of an insoluble and infusible conjugated polymer, such as BBB nanofibres, using electrospinning. Subsequently, these fibres were used for the preparation of sponges and composite membranes. In the future, the preparation and application of high-performance nanofibres and composite materials by electrospinning require more investigations in different aspects.

Firstly, regarding the method of preparation, conjugated fibres through monomers polycondensation in solid-state are highly limited by the solubility of the monomers.

Secondly, some more complicated structures such as porosity or doped BBB nanofibres with additively functions are also an interesting direction. Composite nanofibers, for example, can be obtained without further treatment by using the higher residual polymers instead of PVP as the sacrifice polymer or using additives.

Thirdly, the formation of films based upon the same solution system is still a challenge. Why is the fibre formation smooth but the film problematic? Theoretical and experimental research is required.

Furthermore, the applications of BBB nanofibres are not confined to fire prevention. The applications of BBB nanofibres in the fields of photoelectric, energy filed, high-temperature catalysis and absorption are highly interesting for future research. Large-scale electrospinning is still not trivial and upscaling needs to be tried in the future.

4. Acknowledgments

4. Acknowledgments

Herein I have to give my sincerely appreciation to all the people around and thank for their warmly help and support for my life during my PhD period.

Firstly, I give my deeply appreciate to my supervisor Prof. Dr. Seema Agarwal for the opportunity and financial support to work in this great group and also thank for her kindly supervision of my research work. With her patient and endless guidance and help, she brings me not only the scientific knowledge in this filed but also a lot of useful suggestions which could be great helpful in my future life and work. Then I want to thank Prof. Dr. Andreas Greiner for his useful suggestions and discussions on my projects. It is really a pleasure to work in this group.

I would like to present my thanks to Prof. Dr. Haoqing Hou in College of Chemistry and Chemical Engineering, Jiangxi Normal University, for recommending me to Prof. Greiner's group.

Many thanks to the colleagues and cooperators who give me a lot of help for discussion during my PhD work: Dr. Shaohua Jiang, Prof. Dr. Josef Breu, Dr. Christoph Habel, Dr. Holger Schmalz, Dr. Li Liu, Dr. Xiaojian Liao and Dr. Qiang Gao.

In particular, I want to thank Annette Krökel, Rika Schneider, Bianca Uch, Lothar Benker and Martina Heider for their technical supports. And also thanks to Mrs. Gaby Rösner-Oliver and Mr. Niko Plocher for making the administrative much easier.

Many thanks to my colleagues, who provided nice atmosphere around me for my life and study, Dr. Matthias Burgard, Dr. Steffen Reich, Dr. Judith Schöbel, Dr. Hui Wang, Dr. Markus Langner, Dr. Hadi Bakhshi, Dr. Florian Käfer, Dr. Oliver Hauenstein, Dr. Tobias Moss, Dr. Ling Peng, Martin Pretscher, Amir Reza Bagheri, Lu Chen, Stefan Feth, Marius Feldmann, Julia Kronawitt, Michael Mader, Pin Hu, Mina Heidari, Christian Hils, Chen Liang, Anne Lorenz, Mahsa Mafi, Ann-Kathrin Müller, Simon Neumann, Thomas Schmitt, Adrian Wambach, Chengzhang Xu, Yuanhu Zhang, Anil Kumar, Nikola Majstorovic, Sören Schumacher, Elmar Sehl and all the visiting scholar.

4. Acknowledgments

Further, special thanks give to Welcome Center and International Office of Bayreuth University, they gave many of guidance when I come here in 2015.

Last but not least, I would like to deeply thank my family for the endless help and encourages for my life and my study during my PhD studies.

5. Appendix

5. Appendix

5.1 Nanofibre Preparation of Non-Processable Polymers by Solid-State Polymerization of Molecularly Self-Assembled Monomers

Jian Zhu, Yichun Ding, Seema Agarwal, Andreas Greiner, Hean Zhang and Haoqing Hou. Nanofibre preparation of non-processable polymers by solid-state polymerization of molecularly self-assembled monomers. *Nanoscale*, **2017**, 9(46), 18169-18174.



Cite this: *Nanoscale*, 2017, **9**, 18169
Received 26th September 2017,
Accepted 27th October 2017
DOI: 10.1039/c7nr07159k
rsc.li/nanoscale

Nanofibre preparation of non-processable polymers by solid-state polymerization of molecularly self-assembled monomers†

Jian Zhu,^{a,b} Yichun Ding,^a Seema Agarwal,^b Andreas Greiner,^{a,b} Hean Zhang^c and Haoqing Hou^{*,a}

Polybisbenzimidazobenzophenanthroline-dione (BBB) is a high-performance polymer which is characterized by very high mechanical strength in combination with exceptional thermal stability, but it cannot be processed to electrospun fibres for any useful applications due to its insolubility and infusibility. We overcame all obstacles in the electrospinning of BBB by a new bottom-up, and facile approach for the solid-state polymerization of self-assembled monomer precursors. Key to this new strategy is the incorporation of a high molecular weight sacrificial polymer to aid in fibre formation. The resulting electrospun BBB fibres and belts prepared thereof according to this new approach are very strong and show excellent thermal stability. We envisage that this procedure could be applied to other classes of non-processable high-performance polymers for the preparation of electrospun fibres for applications such as filtration, sound insulation, battery separation, electrodes, fire protection, and reaction engineering under demanding conditions.

Polybisbenzimidazobenzophenanthroline-dione (BBB) (Scheme S1†) is an example of a heterocyclic rigid-rod polymer.¹ The rigid-rod ladder structure of BBB makes it robust with outstanding heat resistance and mechanical properties.^{1–4} Moreover, BBB showed no softening at temperatures up to 425 °C (the thermal limit of the testing apparatus), no weight loss up to 600 °C in nitrogen, and less than 10% weight loss at 315 °C after 1500 h in air.^{1,2,5} In contrast, polyimide which is an industrially used high performance polymer degrades in air after 1000 h at 300 °C with more than 5% weight loss.⁶ BBB exhibits interesting electronic, optical and optoelectronic properties due to its conjugated structure,⁷ and this has led to recent research and development of BBB-con-

taining photovoltaic devices, transistors and batteries.⁸ We expect that the significantly higher electrical and electrochemical behaviour of BBB fibres will outperform other conjugated polymers due to their extreme molecular rigidity in combination with their outstanding thermal stability.

BB polymers (including BBB and BBL, Scheme S2†) are conventionally synthesized by the polycondensation of 1,4,5,8-naphthalene tetracarboxylic acid (NTCA) and either 3,3'-diaminobenzidine (DAB) or 1,2,4,5-tetraaminobenzene (TAB) in polyphosphoric acid (PPA) at a high temperature (~200 °C). However, there has not been a major breakthrough in the preparation of BBB fibres since the 1960s, as their insolubility in common solvents has prevented the establishment of fibre processing and film formation techniques and therefore has been a bottleneck to progress. The new possibility of processing of BBB would enable their integration in demanding systems which are otherwise not accessible for polymer materials due to their limited thermal stability. This insolubility also means that BBB-based high-performance nanofibres cannot be prepared by electrospinning, a fibre production method that has attracted worldwide interest over the past two decades.^{9–12} Electrospinning has been established as the state-of-the-art method for the coating of substrates with nanofibre-based nonwovens. Nearly any soluble, dispersible or fusible polymer as well as mixtures with other compounds like pigments, clays, catalysts, dyes, drugs, enzymes, microbes, and cells could be electrospun. A particular advantage of electrospinning is that it represents a roll-to-roll technique for nanomaterials which enabled its technical translation. With a few exceptions, high-performance polymers cannot be electrospun to nanofibre nonwovens. For example, polyimides (PIs) are such an exception. They can be processed from polyamic acid (PAA), a soluble intermediate during the synthesis of PIs, followed by thermal imidization, a process known as the precursor route^{13–16} even on an industrial scale.^{17,18} However, this route is not applicable for the preparation of BBB nanofibres, because the precursor spinning solution forms an insoluble and non-processable gel owing to the reaction of the four amino groups in the

^aDepartment of Chemistry and Chemical Engineering Jiangxi Normal University, Nanchang, 330022, China. E-mail: haoqing@jxnu.edu.cn

^bMacromolecular Chemistry II and Bayreuth Center for Colloids and Interfaces University of Bayreuth, Universitätsstrasse 30, 95440 Bayreuth, Germany. E-mail: greiner@uni-bayreuth.de

^cDepartment of Chemistry Nanchang University, Nanchang, 330006, China

† Electronic supplementary information (ESI) available. See DOI: 10.1039/c7nr07159k

monomer DAB with 1,4,5,8-naphthalenetetracarboxylic dianhydride (NTDA).

Therefore, a completely new concept was required which we developed based on a *bottom-up* approach. The idea was to self-assemble the monomers 1,4,5,8-naphthalene tetracarboxylic acid and DAB in dimethylacetamide (DMAc) during electrospinning with poly(vinyl pyrrolidone) (PVP) as a sacrificial template. As a result PNDS/PVP composite fibres were obtained.¹⁹ In the second step, heating the PNDS/PVP composite fibres above 460 °C polymerized the self-assembled monomers in the solid state to form the BBB polymer nanofibres and simultaneously removed the sacrificial PVP by thermal decomposition. Note that any kinds of spinnable polymers could be used as a template for assisting the formation of BBB nanofibres; herein PVP was selected as an example for the preparation of BBB nanofibres because it is not only a linear polymer with good spinnability but also almost completely decomposes at a high temperature that could give the neat BBB nanofibres. Even though the decomposition of PVP might leave some vacancy defects that will affect the mechanical properties, a small amount (~20 wt%) of PVP was used and the amount of PVP had no significant influence on the mechanical properties of BBB nanofibres (discussed subsequently). On the other hand, un-sacrificial template polymers, such as polyimides, could be applied in the preparation of BBB composite nanofibres in which there are no vacancy defect issues. The fabrication process and chemical conversion are schematically depicted in Fig. 1.

For fibre formation, NTCA and DAB were mixed in DMAc (30 wt%) at a low temperature (−5 °C) for two hours to self-assemble into PNDS *via* hydrogen bond formation between the

two monomers in order to probe and optimize the concept shown in Fig. 1. However, this PNDS solution could not be electrospun into nanofibres: only small particles were obtained, as shown in Fig. S1.† This was likely due to its relatively low viscosity. With the addition of PVP, the PNDS/PVP solution had sufficient viscosity (2.0–4.0 Pa.S) to form continuous, smooth and uniform nanofibres. Nanofibre mats with random fibres (Fig. 2a and a') and nanofibre belts with well-aligned fibres (Fig. 2b and b') were obtained using stationary and high-speed rotating collectors, respectively. Scanning electron microscopy (SEM) (Fig. 2a' and b') and transmission electron microscopy (TEM) (inset in Fig. 2c) images demonstrate that the as-prepared BBB nanofibres have a smooth surface and uniform diameters. Well-stacked lattice fringes along the BBB nanofibre axis were observed at the edge of the nanofibre by high-resolution TEM (Fig. 2c and d). The lattice fringe spacing is approximately 0.35–0.36 nm (Fig. 2d), which could be considered as the stacking space between the planar repeat packing units of aromatic ladder molecules. The selected area electron diffraction (SAED) pattern of the inset in Fig. 2d shows an amorphous nature, revealing that the BBB nanofibre has no crystallites. The amorphous structure is likely caused by the influence of the six possible structural isomers of the BBB molecules in the repeat unit (Fig. S2†), and the loop coil structure of the molecular chain.^{3,20}

Chemical structures and thermally induced chemical functional group conversions during BBB fibre formation were investigated using Fourier transform infrared spectroscopy (FTIR) by a comparison of the FTIR spectra of PVP, as-spun PNDS/PVP nanofibres, and BBB nanofibres obtained after annealing (Fig. 2e). During the heat-treatment process, PVP

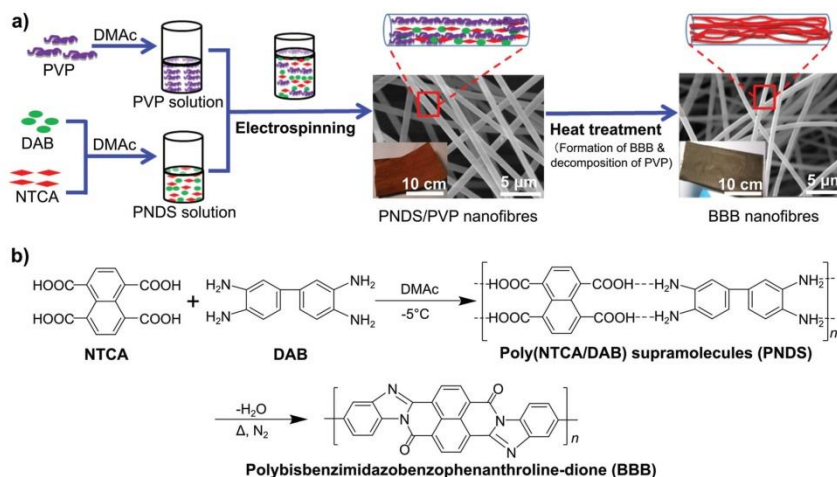


Fig. 1 Schematic illustration of BBB nanofibre preparation: (a) schematic illustration of the preparation of BBB nanofibres by molecular self-assembly and electrospinning; (b) synthesis scheme and chemical structure of the BBB polymer.

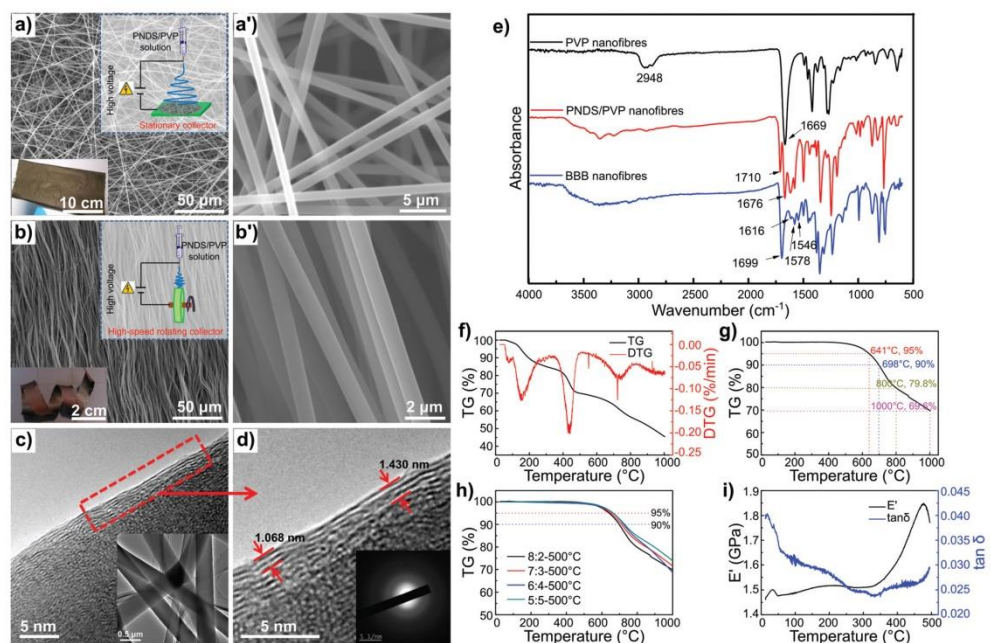


Fig. 2 Morphology, chemical structure and thermal characterization of BBB nanofibres: (a and a') SEM images of BBB nanofibres showing random arrangement and (a') is the magnified SEM image of (a); the top-right inset of (a) is a schematic illustration of the electrospinning set-up for preparing a random BBB nanofibre mat using a stationary collector; the bottom-left inset of (a) is a photograph of the BBB nanofibre mat; (b and b') SEM images of BBB aligned nanofibres and (b') is the magnified SEM image of (b); the top-right inset of (b) is a schematic illustration of the electrospinning set-up for preparing an aligned BBB nanofibre belt using a high-speed rotating collector; the bottom-left inset of (b) is a photograph of the aligned BBB nanofibre belt; (c) high-resolution TEM image of a single BBB nanofibre; the inset of (c) is a transmission electron microscopy (TEM) image of BBB nanofibres; (d) the magnified TEM image of (c), and the inset is a selected area electron diffraction pattern; (e) FT-IR spectra of PVP, PNDS/PVP and BBB nanofibres. (f) TGA and DTG curves of the PNDS/PVP composite nanofibres (8 : 2); (g) TGA curve of BBB nanofibres (prepared from PNDS/PVP (8 : 2) at 500 °C) under nitrogen; (h) TGA curve of BBB nanofibres prepared from PNDS/PVP precursors with different weight ratios (8 : 2, 7 : 3, 6 : 4, and 5 : 5) followed by heating at 500 °C; (i) storage modulus (E') and $\tan \delta$ of the aligned BBB nanofibre belt (prepared from PNDS/PVP (8 : 2) at 500 °C).

decomposes at temperatures above 400 °C, as shown by the thermogravimetric analysis (TGA) curve of PVP (Fig. S3†), and the disappearance of characteristic PVP peaks at 1669 cm^{-1} (C=O stretching vibrations) and 2948 cm^{-1} (C-H stretching vibrations) (Fig. 2e). The peaks at 3300 cm^{-1} and 1710 cm^{-1} were attributed to PNDS and the characteristic absorptions of $-\text{NH}_2$ and stretching vibrations of C=O in $-\text{COOH}$. All these peaks disappeared in the spectrum of the BBB nanofibres, while new peaks appeared at 1699, 1616, 1578 and 1547 cm^{-1} (Fig. 2e), corresponding to the C=O, C=C, C=N and C-N vibrations of aromatic imide and benzimidazole structures, respectively, confirming the formation of the BBB polymer structure.^{21–23}

Due to the multifunctional nature of NTCA and DAB, the formation of the BBB polymer is a complicated process. Therefore, in a separate experiment, we studied the development of various chemical structures during polymer formation

by performing FTIR upon the application of a heating program to the starting monomer mixture (Fig. S4†). The formation of the BBB polymer occurred through the condensation of intermediate structures with amide, imide and benzimidazole units. The TGA curve of the PNDS/PVP (8 : 2 weight ratio) nanofibres (Fig. 2f) shows the formation process of the BBB nanofibres. As shown in Fig. 2f by the DTG curve, the first stage at 100–250 °C shows PNDS dehydration to form amide, imide and benzimidazole structures (Fig. S4†), along with H_2O evaporation; the second stage at 350–500 °C is due to the decomposition of PVP and the conversion of amide, imide and benzimidazole structures into BBB; and the third stage at temperatures above 600 °C shows the degradation of the BBB polymer.

Thermogravimetric analysis (TGA) shows that BBB nanofibres are heat resistant with a degradation onset temperature above 600 °C, and 5% ($T_{5\%}$) and 10% ($T_{10\%}$) weight loss temperatures of 641 °C and 698 °C, respectively (Fig. 2g and h), as

5. Appendix

View Article Online

Communication

Nanoscale

measured under a nitrogen atmosphere. Dynamic mechanical analysis (DMA) measurements of the BBB nanofibres did not show a clear glass transition up to 500 °C but did show a $\tan \delta$ less than 0.040 (approximately 0.025 at 350 °C), and the storage modulus (E') increased with an increase in the temperature which could be of significance in demanding applications as in the aerospace industry (Fig. 2i). The TMA test shows that the BBB nanofibres had negligible shrinkage even when heated to 450 °C (Fig. S5†). These results indicate that the BBB nanofibres exhibit outstanding heat resistance and thermal mechanical performance.

Next, mechanical characterization techniques were used to investigate the influence of the PNDS/PVP weight ratio, and the heat-treatment temperature profile, on the mechanical performance of the as-prepared BBB nanofibre belts. The PNDS/PVP (8:2) composite nanofibre belt shows a stress of ~50 MPa and a strain of 4% (Fig. S6†). After high-temperature annealing, PNDS is converted to the BBB polymer, and the PVP viscosity modifier thermally decomposes. The as-formed BBB polymers had very rigid structures, leading to a significant increase in mechanical properties. Fig. 3a shows the typical stress-strain curves, and Fig. 3b shows the relationship

between the heat-treatment temperature and the mechanical properties of the BBB nanofibre belts. The highest tensile strength was 365 ± 5 MPa, which was achieved for the BBB nanofibres formed using the precursor PNDS/PVP (8:2) with heat treatment at 500 °C. Notably, the heat-treatment temperature affects the mechanical properties of the BBB polymer to a much greater extent than the amount of PVP in the precursor (see Table S2†).

The mechanical properties of polymer films and fibres can be further improved using a variety of techniques, of which the most common one is known as hot stretching and has also been used successfully with nanofibre mats. Here, we also prepared BBB nanofibre belts with hot stretching during thermal annealing. The mechanical strength increased from 364 ± 4 MPa to approximately 450 ± 8 MPa (Fig. 3c) for a BBB nanofibre belt fabricated under a tensile force of 5 N during the heat-treatment process.

Tensile testing of individual nanofibres was performed to obtain a better understanding of the mechanical properties of the BBB nanofibre mats. A single BBB nanofibre was extracted from a fluffy non-oriented nanofibre mat and fixed to a laboratory-made paper framework (Fig. 3d). Part of the paper support

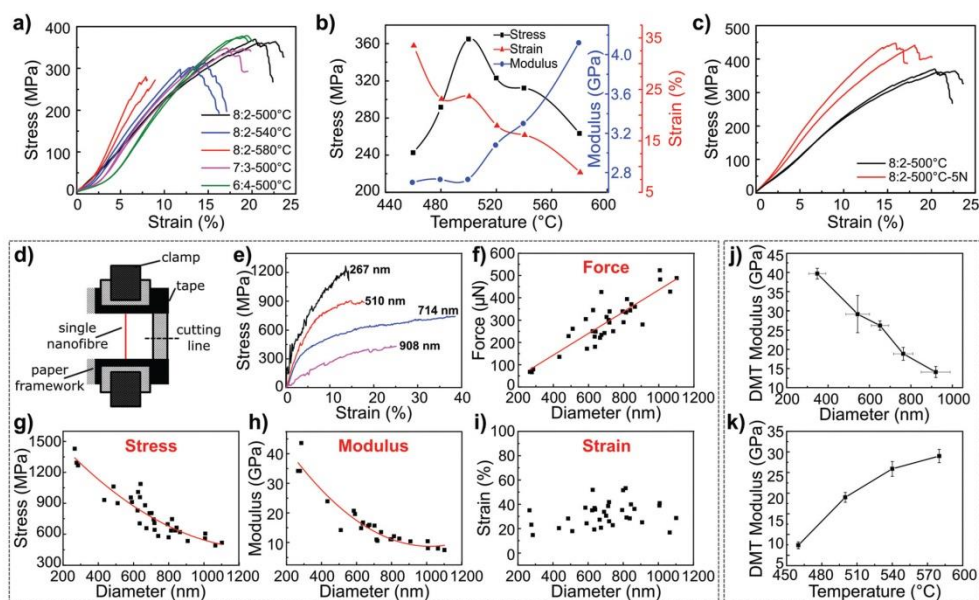


Fig. 3 Mechanical characterization of electrospun BBB aligned nanofibre belt and single nanofibres: (a) stress-strain curves of different types of BBB nanofibre belts made by changing either the PNDS : PVP ratio or the annealing temperature; (b) the relationship between mechanical properties and the BBB nanofibre belt annealing temperature; (c) stress-strain curves of the BBB nanofibre belt prepared without hot stretching and with hot stretching at 5 N; (d–i) mechanical characterization of an individual BBB nanofibre: (d) schematic of the method, (e) stress-strain curves, (f) load force, (g) stress, (h) modulus, (i) strain of individual BBB nanofibres with different diameters, (j) relationship between the DMT modulus of individual nanofibres and the fibre diameter; the tested nanofibres underwent heat treatment at 500 °C, and (k) relationship between the DMT modulus of individual nanofibres and the annealing temperature.

is then cut to allow the tensile testing of a single isolated BBB nanofibre. The BBB nanofibre diameter was modulated by adjusting the concentration of the electrospinning solution. The tensile testing of individual BBB nanofibres with different diameters was performed as reported previously (Fig. S7†).²⁵ Fig. 3e shows typical stress–strain curves of single nanofibres and correlations between the fibre diameter and the maximum force at break, stress, modulus, and strain at break (Fig. 3f–i). We found that the BBB fibre diameter was strongly correlated with the mechanical properties and the stress and modulus of nanofibres increased with the decrease of the fibre diameter, similar to the observations in previous reports on other fibres.^{24–26} The maximum tensile strength and modulus are 1.43 ± 0.26 GPa and 34.16 ± 1.82 GPa, respectively, for the BBB nanofibre with a diameter of 226 nm. The dramatic increases in strength and modulus are due to well-known size effects, which could be attributed to the molecular orientation and the crystallinity of the polymer fibre, which increase with a decrease in the fibre diameter.^{27,28}

To gain further understanding of the nanomechanical properties of individual nanofibres, the modulus of individual BBB nanofibres was also explored by using the peak force (PF) quantitative nanoscale mechanical (QNM) characterisation mode of scanning probe microscopy (SPM), which enables the quantitative measurement of nanomechanical properties (such as modulus, deformation and dissipation) at the nanoscale on a material's surface.^{29,30} Fig. S8† shows the typical mapping of the height, peak force error and DMT modulus of a single BBB nanofibre. The average DMT modulus of the BBB nanofibres is plotted *versus* the fibre diameter in Fig. 3j. SPM exhibits a DMT modulus of approximately 40 GPa for the BBB fibre with a diameter of 350 nm and approximately 14 GPa for a 920 nm diameter BBB fibre (Fig. 3j). The trend in DMT modulus *versus* BBB nanofibre diameter is consistent with the tensile modulus determined by individual nanofibre tensile testing (Fig. 3h). Fig. 3k shows that the BBB nanofibre DMT modulus increases with an increase in the heat-treatment temperature. This trend is consistent with the tensile test results of the aligned nanofibre belts as discussed previously (Fig. 3b).

Conclusions

In summary, we report a novel bottom-up strategy for producing high-performance BBB nanofibres by electrospinning a molecularly self-assembled solution of the corresponding monomers NTCA and DAB, together with PVP as a sacrificial viscosity-modifier, followed by solid-state thermal polymerization to BBB. The as-prepared BBB nanofibre belts show excellent mechanical properties, with the highest tensile strength of 364.75 ± 4.76 MPa achieved for the nanofibre belt. The strength increased to 450 MPa upon stretching the belt with 5 N tension at 500 °C. The mechanical properties of the individual BBB nanofibres were diameter-dependent. For a single BBB nanofibre with a diameter of approximately 226 nm we found the tensile strength and the modulus to be as high

as 1.43 ± 0.26 GPa and 34.16 ± 1.82 GPa, respectively. The BBB nanofibres show excellent heat resistance with a 5% weight loss temperature of 641 °C. The dynamic mechanical analysis showed that the nanofibres exhibited no glass transition until 500 °C, and an aligned BBB nanofibre belt showed negligible thermal shrinkage. Importantly, the novel method presented in this paper could readily be applied for preparing other high-performance nanofibres that cannot be directly made by electrospinning due to their poor solubility.

Experimental

Materials

3,3'-Diaminobenzidine (DAB) was purchased from Changzhou Sunlight Pharmaceutical Co., Ltd (Changzhou, China). 1,4,5,8-Naphthalene tetracarboxylic acid (NTCA) was purchased from Zhengzhou Alfa Chemical Co., Ltd (Zhengzhou, China). Poly(vinyl pyrrolidone) (PVP, M_w : 1 300 000) was purchased from Aladdin Reagent Co., Ltd (Shanghai, China). Dimethylacetamide (DMAc, AR) was purchased from Tianjin Fu Chen Chemicals Reagent Factory (Tianjin, China) and used after distillation. All other chemicals were used without further purification.

Preparation of BBB nanofibres

First, a poly(NTCA/DAB)/supramolecular PNDS solution was prepared by dissolving equimolar amounts of DAB and NTCA in DMAc at -5 °C and stirred for 2 h. The solid content in the PNDS solution was 30 wt%. PVP was dissolved in DMAc to form a 20 wt% solution. Then, PNDS/PVP solutions with various solid mass ratios (8:2, 7:3, 6:4 and 5:5) were prepared by mixing specific volumes of PNDS and PVP solutions. The electrospinning process was performed at an applied voltage of 15 kV with a collecting distance of 15 cm and a feeding rate of 1.0 mL h^{-1} . Two types of nanofibres were collected: (1) aligned nanofibre belts were collected on a laboratory-built rotating disc (aluminium) collector at a linear speed of 24 m s^{-1} and (2) random nanofibre mats were collected on grounded aluminium foil. The PNDS/PVP composite nanofibres were dried under vacuum at 40 °C for 2 h. The heat-treatment process used to form BBB nanofibres by solid-state polymerization was performed in a high-temperature furnace under a nitrogen atmosphere and at a heating rate of 10 °C min^{-1} , in three stages as follows: (1) heating to 150 °C with 1 h annealing; (2) heating to 250 °C with 1 h annealing; and (3) heating to 460, 480, 500, 520, 540 or 580 °C for different samples and annealing for 1 h.

Characterization

FT-IR (Bruker Tensor 27) was used to identify the chemical structures. Scanning electron microscopy (SEM) (FEI Quanta 200, USA) and transmission electron microscopy (TEM) (JEM-3010, Japan) were employed to observe the morphologies of the BBB nanofibres and their internal structures. The mechanical properties of the aligned nanofibre belts were

measured using an electromechanical universal testing machine (SANS, Shenzhen, China) at a tensile speed of 5 mm min⁻¹ with a sample dimension of 4 mm by 50 mm. The thicknesses of the samples were calculated based on the density of the corresponding BBB film (1.62 g cm⁻³).⁴ Atomic force microscopy (AFM) (Shanghai, China) was, in a tapping mode, used to measure the diameters of the single fibres. The mechanical properties of individual electrospun BBB nanofibres were determined using a microtensile testing machine (JQ03, Power-Reach Digital Equipment Ltd, Shanghai, China) using a previously reported method,²⁴ and the details are described in the ESI (Fig. S7†). The DMT modulus of a single BBB nanofibre was measured using scanning probe microscopy (SPM) (Bruker MultiMode8). The samples were prepared by adhering an individual BBB nanofibre on a mica sheet with A-B resin glue with a curing temperature of 60 °C for 6 h and with a glue thickness less than the fibre diameter. The modulus was calculated using the NanoScope software and the Derjaguin–Muller–Toropov model (referred to as the DMT modulus). Thermogravimetric analysis (Beijing Henven Scientific Instrument Factory, China) was carried out under a nitrogen atmosphere at a heating rate of 10 °C min⁻¹. Dynamic mechanical analysis (DMA) was performed on a PerkinElmer diamond analyser in the tensile mode under a nitrogen atmosphere at a heating rate of 3 °C min⁻¹ over a range of 30–500 °C.

Conflicts of interest

There are no conflicts to declare.

Acknowledgements

This research was supported by the National Natural Science Foundation of China (Grant No. 21564008).

Notes and references

- W. E. Gibbs, *J. Macromol. Sci., Part A: Pure Appl. Chem.*, 1968, **2**, 1291–1302.
- F. E. Arnold and R. L. Van Deusen, *Macromolecules*, 1969, **2**, 497–502.
- R. L. Van Deusen, *J. Polym. Sci., Part B: Polym. Lett.*, 1966, **4**, 211–214.
- G. C. Berry, *J. Polym. Sci., Polym. Phys. Ed.*, 1976, **14**, 451–478.
- R. L. Van Deusen, O. K. Goins and A. J. Sicree, *J. Polym. Sci., Part A1*, 1968, **6**, 1777–1793.
- X. Wu, Y. Ding, S. Chen, M. Lu, G. Ling, T. Shen and S. Li, *J. East China Inst. Chem. Technol.*, 1981, **3**, 67–76.
- O.-K. Kim, *J. Polym. Sci., Polym. Lett. Ed.*, 1982, **20**, 663–666.
- A. G. Manoj and K. S. Narayan, *Opt. Mater.*, 2003, **21**, 417–420.
- H. R. Darrell and C. Iksoo, *Nanotechnology*, 1996, **7**, 216.
- S. Agarwal, A. Greiner and J. H. Wendorff, *Prog. Polym. Sci.*, 2013, **38**, 963–991.
- Y. Dzenis, *Science*, 2004, **304**, 1917–1919.
- A. Greiner and J. H. Wendorff, *Angew. Chem., Int. Ed.*, 2007, **46**, 5670–5703.
- C. Nah, S. H. Han, M.-H. Lee, J. S. Kim and D. S. Lee, *Polym. Int.*, 2003, **52**, 429–432.
- C. Huang, S. Chen, D. H. Reneker, C. Lai and H. Hou, *Adv. Mater.*, 2006, **18**, 668–671.
- S. Chen, P. Hu, G. Andreas, C. Cheng, H. Cheng, F. Chen and H. Hou, *Nanotechnology*, 2008, **19**, 015604.
- Y. Ding, H. Hou, Y. Zhao, Z. Zhu and H. Fong, *Prog. Polym. Sci.*, 2016, **61**, 67–103.
- Y.-E. Miao, G.-N. Zhu, H. Hou, Y.-Y. Xia and T. Liu, *J. Power Sources*, 2013, **226**, 82–86.
- H. Hou, C. Cheng, S. Chen, X. Zhou, X. Lv, P. He, X. Kuang and J. Ren, US9209444B2, 2015.
- A. Stoilkovic, M. Ishaque, U. Justus, L. Hamel, E. Klimov, W. Heckmann, B. Eckhardt, J. H. Wendorff and A. Greiner, *Polymer*, 2007, **48**, 3974–3981.
- G. C. Berry and T. G. Fox, *J. Macromol. Sci., Part A: Pure Appl. Chem.*, 1969, **3**, 1125–1146.
- S. A. Jenekhe and P. O. Johnson, *Macromolecules*, 1990, **23**, 4419–4429.
- M. F. Roberts and S. A. Jenekhe, *Polymer*, 1994, **35**, 4313–4325.
- V. G. Ammons and G. C. Berry, *J. Polym. Sci., Part A2*, 1972, **10**, 449–471.
- F. Chen, X. Peng, T. Li, S. Chen, X.-F. Wu, D. Reneker and H. Hou, *J. Phys. D: Appl. Phys.*, 2008, **41**, 025308.
- S. Jiang, G. Duan, E. Zussman, A. Greiner and S. Agarwal, *ACS Appl. Mater. Interfaces*, 2014, **6**, 5918–5923.
- L. Chen, S. Jiang, J. Chen, F. Chen, Y. He, Y. Zhu and H. Hou, *New J. Chem.*, 2015, **39**, 8956–8963.
- D. Papkov, Y. Zou, M. N. Andalib, A. Goponenko, S. Z. D. Cheng and Y. A. Dzenis, *ACS Nano*, 2013, **7**, 3324–3331.
- A. Arinstein, M. Burman, O. Gendelman and E. Zussman, *Nat. Nanotechnol.*, 2007, **2**, 59–62.
- A. N. Frone, S. Berlioz, J.-F. Chailan and D. M. Panaiteescu, *Carbohydr. Polym.*, 2013, **91**, 377–384.
- D. M. Panaiteescu, A. N. Frone and C. Nicolae, *Eur. Polym. J.*, 2013, **49**, 3857–3866.

5. Appendix

Electronic Supplementary Material (ESI) for Nanoscale.
This journal is © The Royal Society of Chemistry 2017

Supporting Information

Nanofibre Preparation of Non-processable Polymers by Solid-state

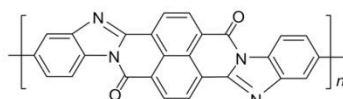
Polymerization of Molecularly Self-assembled Monomers

Jian Zhu^{a,b}, Yichun Ding^a, Seema Agarwal^b, Andreas Greiner^{b*}, Hean Zhang^c, and Haoqing Hou^{a*}

^a Department of Chemistry and Chemical Engineering, Jiangxi Normal University, Nanchang, 330022, China. E-mail: haoqing@jxnu.edu.cn

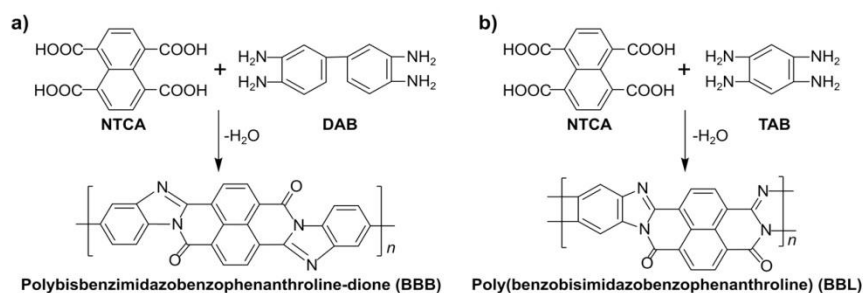
^b Macromolecular Chemistry II and Bayreuth Center for Colloids and Interfaces, University of Bayreuth, Universitätsstrasse 30, 95440, Bayreuth, Germany. E-mail: greiner@uni-bayreuth.de

^c Department of Chemistry, Nanchang University, Nanchang, 330006, China



Polybisbenzimidazobenzophenanthroline-dione (BBB)

Scheme S1. Chemical structure of the BBB polymer.



Scheme S2. Synthesis and chemical structures of (a) BBB and (b) BBL polymers.

5. Appendix

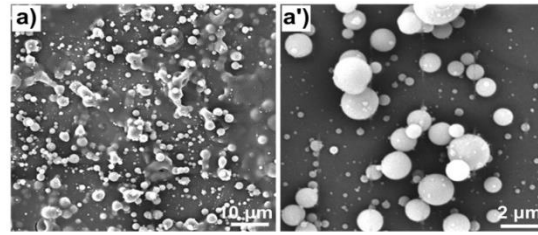


Figure S1. SEM images showing particle formation by the electrospinning of PNDS.

5. Appendix

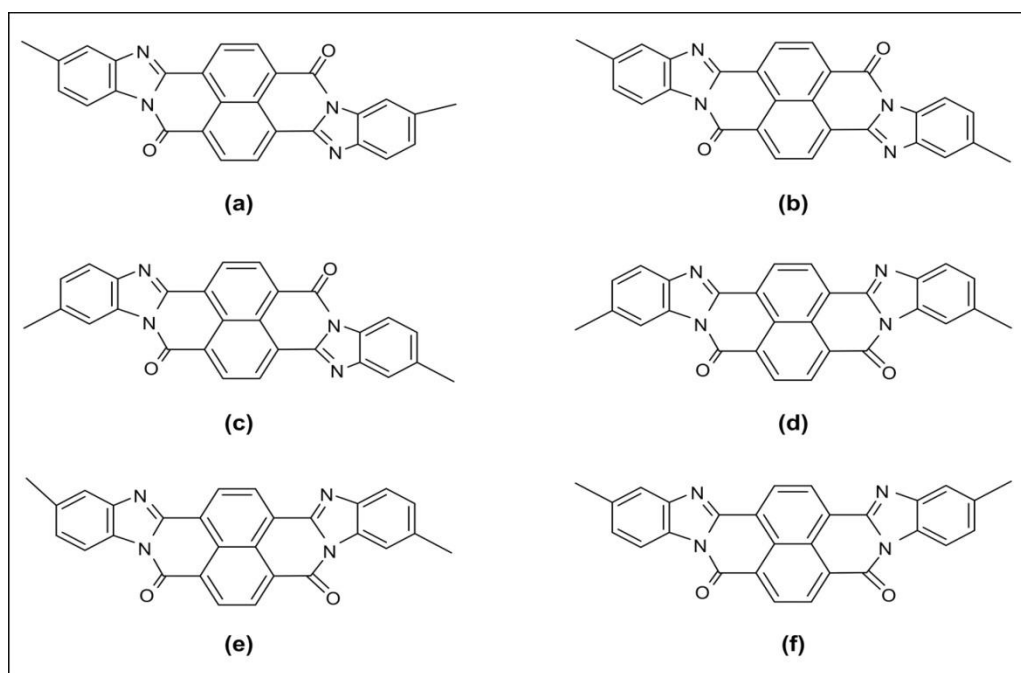


Figure S2. Schematic representation of the repeat unit of BBB isomers¹.

5. Appendix

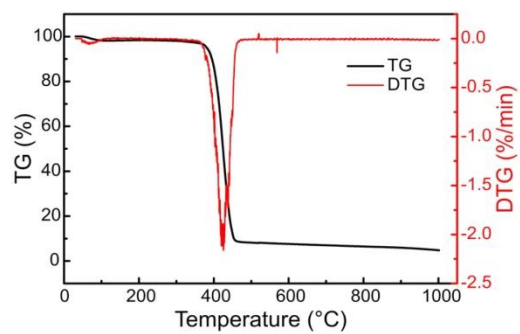


Figure S3. Thermogravimetric analysis (TGA) and DTG curves show the decomposition of neat PVP nanofibres.

5. Appendix

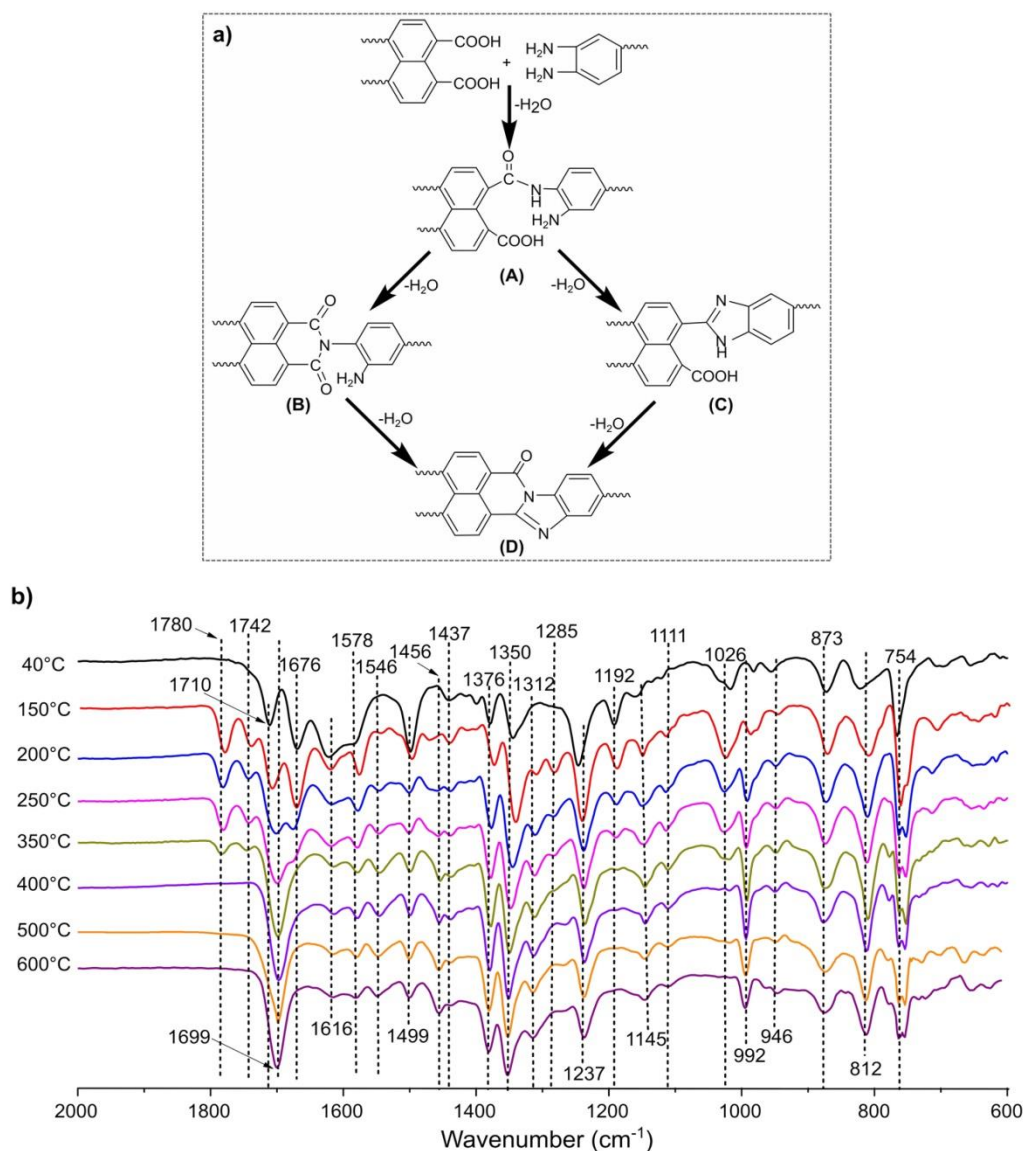
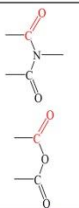


Figure S4. Investigation of BBB polymer formation: a) possible routes for the polymerization of 1,4,5,8-naphthalene tetracarboxylic acid (NTCA) and 3,3'-diaminobenzidine (DAB) to BBB, where possible intermediates include amide (A), imide (B) and benzimidazole (C) structures. b) FTIR spectra of the products formed by heating a 1:1 comonomer mixture of NTCA and DAB at different temperatures.

5. Appendix

Table S1. Compilation of results from FT-IR (Figure S4b) regarding the presence of different peaks, signifying different chemical structures at various temperatures.

Absorption	Assignment	40°C	150°C	200°C	250°C	350°C	400°C	500°C	600°C
1780 cm ⁻¹	 $\nu_{(C=O)}$ imide carbonyl carbon-oxygen asymmetric stretching ² ; or $\nu_{(C=O)}$ anhydride carbonyl carbon-oxygen asymmetric stretching ^{3,4}	✓	✓	✓	✓	✓	✗	✗	✗
1742 cm ⁻¹	 $\nu_{(C=O)}$ anhydride carbonyl carbon-oxygen symmetric stretching ³	✗	✓	✓	✓	✓	✗	✗	✗
1710 cm ⁻¹	 $\nu_{(C=O)}$ in carboxyl group	✓ ₁₇₁₀	✓ ₁₇₀₅	✗	✗	✗	✗	✗	✗
1676 cm ⁻¹	 $\nu_{(C=O)}$, in amide carbonyl	✓	✓	✓	✓	✗	✗	✗	✗
1699 cm ⁻¹	 $\nu_{(C=O)}$, imide carbonyl carbon-oxygen stretching in BBB structure ⁵	✗	✗	✓	✓	✓	✓	✓	✓
1578 cm ⁻¹	 $\nu_{(C=N)}$, imine C=N stretching ⁵	✗	✓	✓	✓	✓	✓	✓	✓
1616 cm ⁻¹ 1499 cm ⁻¹	 aromatic C-C and C-N skeletal modes ⁵	✓ ₁₆₂₂ ✓	✓ ₁₆₂₂ ✓	✓ ₁₆₁₉ ✓	✓ ₁₆₁₉ ✓	✓ ₁₆₁₆ ✓	✓ ₁₆₁₆ ✓	✓ ₁₆₁₆ ✓	✓ ₁₆₁₆ ✓
1546 cm ⁻¹ 1312 cm ⁻¹	 C-N skeletal vibrations ⁵	✗ ✗	✓ ✓						
1456 cm ⁻¹ 1437 cm ⁻¹	 $\nu_{(C-N)}$, amide C-N stretching ⁵	✓ ₁₄₄ 2	✓ ₁₄₄ 3	✓ ✓	✓ ✓	✓ ✓	✓ ✓	✓ ✓	✓ ✓
1376 cm ⁻¹ 1350 cm ⁻¹	 $\nu_{(C-N)}$ of carbon-nitrogen single bonds ⁵	✓ ✓ ₁₃₄₄	✓ ✓ ₁₃₄₄	✓ ✓ ₁₃₄₄	✓ ✓ ₁₃₄₈	✓ ✓ ₁₃₅₀	✓ ✓ ₁₃₅₁	✓ ✓ ₁₃₅₂	✓ ✓ ₁₃₅₂
1285 cm ⁻¹	 breathing vibration of the imidazole ring (C-N-H) ⁶	✓	✓	✓	✓	✗	✗	✗	✗
1192 cm ⁻¹	 $\nu_{(C-O)}$ in carboxyl group	✓	✓	✓	✓	✗	✗	✗	✗
1026 cm ⁻¹	 $\nu_{(C-N)}$, C-N stretching of C-NH ₂	✓	✓	✓	✓	✓	✗	✗	✗
1237 cm ⁻¹ 992 cm ⁻¹	 aromatic skeletal vibrations ⁵	✓ ₁₂₄₇ ✗	✓ ₁₂₄₃ ✓	✓ ₁₂₃₈ ✓	✓ ₁₂₃₇ ✓	✗ ₁₂₃₆ ✓	✗ ₁₂₃₆ ✓	✗ ₁₂₃₆ ✓	✗ ₁₂₃₆ ✓
1145 cm ⁻¹ 1111 cm ⁻¹	 in-plane C-H bending ⁵	✓ ₁₁₅₈ ✓ ₁₁₁₆	✓ ₁₁₅₂ ✓ ₁₁₁₆	✓ ₁₁₅₀ ✓ ₁₁₁₃	✓ ₁₁₄₇ ✓ ₁₁₁₁	✓ ₁₁₄₆ ✓ ₁₁₁₁	✓ ₁₁₄₅ ✓ ₁₁₁₁	✓ ₁₁₄₅ ✓ ₁₁₁₁	✓ ₁₁₄₅ ✓ ₁₁₁₁
946 cm ⁻¹ 873 cm ⁻¹ 812 cm ⁻¹	 out-of-plane C-H wagging ⁵	✓ ✓ ✓							

5. Appendix

754 cm ⁻¹		(C-H), out-of-plane wag of naphthalene C-H bonds 5	✓	✓	✓	✓	✓	✓	✓	✓
----------------------	---	--	---	---	---	---	---	---	---	---

*Note: The tick mark indicates absorption, and the x mark indicates no absorption; a small mark indicates low absorption, and large mark indicates high absorption. A mark with a subscript indicates that the absorption has a peak shift.

Investigation of BBB polymer formation: Due to the multi-functionality of NTCA and DAB, the formation of the BBB polymer is a complicated process. The polycondensation between amino and acid groups can occur via several different routes. Typically, it can form an amide structure (structure **A**, **Figure S4a**) by losing one H₂O molecule in each repeat unit and can form an imide structure (structure **B**, **Figure S4a**) or a benzimidazole structure (structure **C**, **Figure S4a**) by losing two H₂O molecules in each repeat unit^{4, 7}. The imide and benzimidazole structures could convert to BBB (structure **D**, **Figure S4a**) by losing an additional H₂O molecule in each repeat unit. To further understand the thermally induced formation of the BBB polymer, we investigated the polycondensation reaction by FTIR. The two monomers were dissolved in dimethylacetamide in equimolar ratios and precipitated in ethanol, and the powder was heated at different temperatures (40, 150, 200, 250, 350, 400, 500, or 600°C) for 1 h at each temperature. The FT-IR spectra of the samples are shown in **Figure S4b**, and the characteristic absorptions are listed in **Table S1**.

At 40°C, the characteristic absorptions of -COOH ($\nu_{\text{C-O}}$ at 1710 cm⁻¹, $\nu_{\text{C-O}}$ at 1192 cm⁻¹) and -C-NH₂ (deformation vibration of -NH₂ at 1026 cm⁻¹) were seen. Absorptions at 1676 and 1437 cm⁻¹ corresponding to the $\nu_{\text{C=O}}$ and the C-N stretching in amides (-C(O)-NH-) were also observed, indicating the formation of an amide structure (structure **B**, **Figure S4a**). The peaks at 1616 and 1499 cm⁻¹ correspond to C=C in the aromatic benzene skeleton, 1376 and 1350 cm⁻¹ correspond to carbon-nitrogen single bonds, and 1237, 946, 873, 812 and 754 cm⁻¹

5. Appendix

correspond to aromatic skeleton vibrations and in-plane and out-of-plane C-H bending modes. When heat treated at 150°C, new absorptions at 1780 cm⁻¹ and 1705 cm⁻¹ (an overlap peak with C=O in -COOH) were observed, which are likely to be due to the asymmetric and symmetric vibrations of C=O in the carbonyl imide ring⁸ indicating the formation of an imide structure (molecule **B**, **Figure S4a**). In addition, new absorptions at 1578 and 1285 cm⁻¹ were also observed, these peaks correspond to C=N and C-N-H in the imidazole ring, respectively⁶, indicating the formation of a benzimidazole structure (molecule **C**, **Figure S4a**). In addition, the formation of end dianhydride groups is indicated by characteristic peaks at 1780 cm⁻¹ (asymmetric vibrations of C=O) and 1742 cm⁻¹ (symmetric vibrations of C=O)³. Hence, the reaction of NTCA and DAB began at 150°C, in which the intermediate is a mixture of amide, imide and benzimidazole structures. With a further increase in the temperature to 200°C, the absorptions at 1710 and 1676 cm⁻¹ began to disappear, and a new signal appeared at 1699 cm⁻¹ ($\nu_{(C=O)}$ in the BBB structure), indicating the formation of the BBB structure. The absorptions at 1710 and 1676 cm⁻¹ almost completely disappeared, and the intensity of the absorption at 1699 cm⁻¹ became strong at temperatures above 250°C. In addition, the characteristic peak of benzimidazole at 1285 cm⁻¹ almost completely disappeared at 250°C. These phenomena demonstrate the conversion of amide, imide and benzimidazole structures into the BBB polymer. In addition, the characteristic peaks of end dianhydride groups at 1780 and 1742 cm⁻¹ continuously weakened with an increase in temperature and finally disappeared at above 400°C (400, 500, and 600°C), indicating an increase in molecular weight with an increase in heat-treatment temperature. Finally, at 350, 400, 500, and 600°C, the absorptions at 1699, 1616, 1578 and 1547 cm⁻¹, corresponding to the C=O, C=C, C=N and C-N, respectively, on aromatic imide and benzimidazole structures, confirm the formation of the BBB polymer.

5. Appendix

Hence, neat BBB nanofibres could be obtained by the heat treatment of PNDS/PVP above 460°C (see experimental details described in the main text) because the NTCA and DAB could be completely converted into BBB at temperatures above 250°C and PVP could be completely decomposed at temperatures above 460°C.

5. Appendix

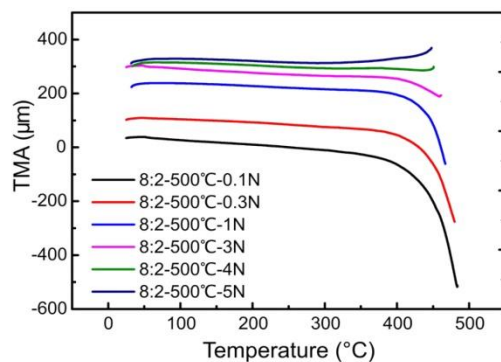


Figure S5. Thermal-shrinkage behaviour of BBB nanofibre belts: BBB nanofibre belts (prepared from PNDS/PVP (8:2); heating at 500°C) with an initial length of 10 mm and a width of 4 mm were fixed on the DMA instrument, and different constant tension forces (*i.e.*, 0.1, 0.3, 1, 3, 4 and 5 N) were applied. The results showed that the shrinkage at 450°C was only 1.16% under 5 N tension force and 4.8% under 0.1 N.

5. Appendix

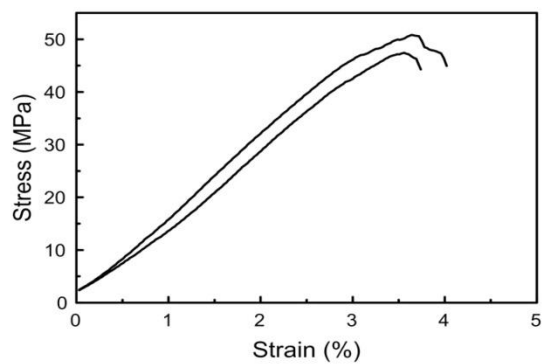


Figure S6. Stress-strain curves of the PNDS/PVP (8:2) composite nanofibre belt.

5. Appendix

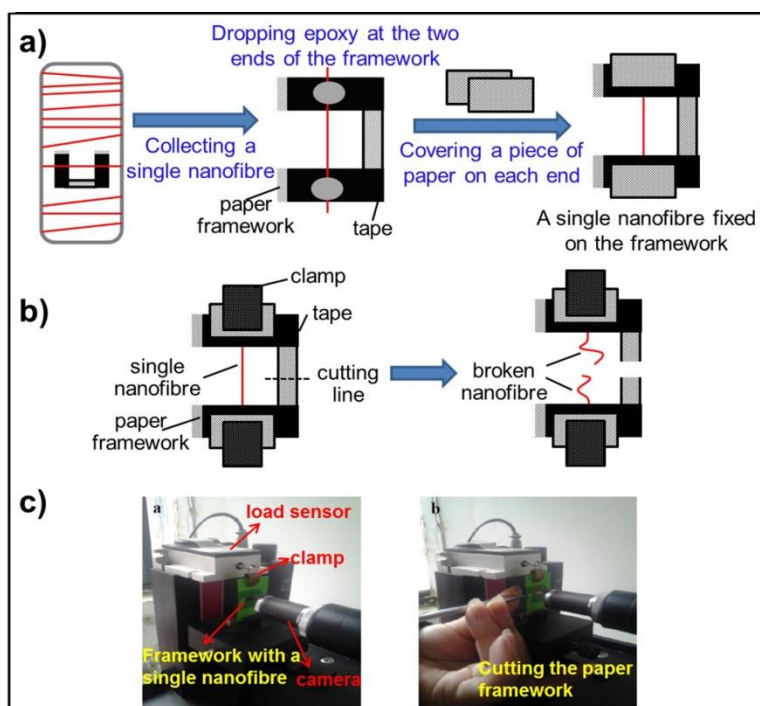


Figure S7. Mechanical characterization of a single BBB nanofibre: a) schematic of picking a single BBB nanofibre and fixing on a paper framework, b) schematic diagram of the paper framework holding a single nanofibre in the clamps for the tension test and cutting the paper frame to perform the tensile test, and c) optical image of the single nanofibre testing machine holding the sample and the process of cutting the paper framework.

Mechanical characterization of a single BBB nanofibre: Tensile tests of single electrospun nanofibres were performed on a microtensile testing machine (JQ03, Power-Reach Digital Equipment Ltd., Shanghai, China). The tensile tester consisted of a 19.6 mN to 0.50 μ N microload sensor (Minebea Co., Ltd, Japan), a high-magnification optical microscope (MS160, WDK, Japan), a digital camera, software for data acquisition and processing and a computerized control system. The test method was the same as that previously reported by

5. Appendix

us⁹⁻¹¹. The testing process consists of five steps: 1) load the single nanofibre sample onto the paper framework (**Figure S7a**), 2) mount the paper framework carrying the single nanofibre sample in the clamps of the microtensile tester, 3) cut the 'rib' of the paper frame (**Figure S7c**), 4) locate the nanofibre sample using the optical microscope to ensure that only one nanofibre sample is present, and 5) load the single nanofibre sample to break with the microtension tester (**Figure S7c**). A constant loading rate of 1 mm/min was utilized over the entire tensile testing process.

5. Appendix

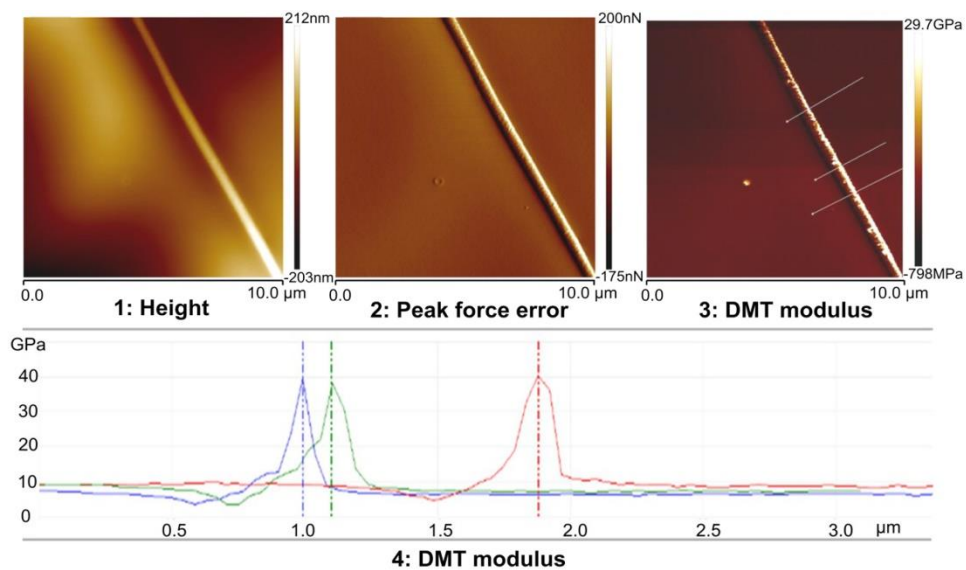


Figure S8. Nanomechanical characterization of BBB single nanofibres using scanning probe microscopy (SPM) and peak force (PF) quantitative nanoscale mechanical (QNM) characterization: maps of the typical height, peak force error and DMT modulus (Derjaguin-Muller-Toropov model) of BBB individual nanofibres.

5. Appendix

Table S2 Summary of mechanical properties of different types of BBB nanofibre belts.

BBB belts*	Stress (MPa)	Strain at break (%)	Modulus (GPa)
8:2-460°C	242.57±10.72	33.49±2.61	2.70±0.48
8:2-480°C	291.73±13.23	23.15±1.48	2.73±0.12
8:2-500°C	364.75±4.76	23.66±3.01	2.73±0.2
8:2-520°C	323.15±16.84	17.95±1.03	3.08±0.26
8:2-540°C	312.26±27.48	16.13±1.67	3.3±0.12
8:2-580°C	263.42±16.89	8.84±1.12	4.12±0.69
6:4-500°C	378.05±3.55	20.1±0.53	3.19±0.18
7:3-500°C	339.45±14.13	19.91±2.32	3.24±0.35

*Sample designation: m:n-y°C, m:n is the weight ratio of NTCA+DAB: PVP, y is the temperature used for heating the PNDS/PVP composite fibres to convert them to BBB nanofibres.

References

1. G. C. Berry and T. G. Fox, *Journal of Macromolecular Science: Part A - Chemistry*, 1969, **3**, 1125-1146.
2. C. A. Pryde, *Journal of Polymer Science Part A: Polymer Chemistry*, 1989, **27**, 711-724.
3. N. Srinate, S. Thongyai, R. A. Weiss and P. Praserttham, *J Polym Res*, 2013, **20**, 138.
4. V. G. Ammons and G. C. Berry, *Journal of Polymer Science Part A-2: Polymer Physics*, 1972, **10**, 449-471.
5. M. F. Roberts and S. A. Jenekhe, *Polymer*, 1994, **35**, 4313-4325.
6. H. Luo, H. Pu, Z. Chang, D. Wan and H. Pan, *Journal of Materials Chemistry*, 2012, **22**, 20696-20705.
7. R. L. Van Deusen, O. K. Goins and A. J. Sicree, *Journal of Polymer Science Part A-1: Polymer Chemistry*, 1968, **6**, 1777-1793.
8. A. Li, Z. Ma, H. Song, N. Li and M. Hou, *RSC Advances*, 2015, **5**, 79565-79571.
9. F. Chen, X. Peng, T. Li, S. Chen, X.-F. Wu, D. Reneker, H. and H. Hou, *Journal of Physics D: Applied Physics*, 2008, **41**, 025308.
10. S. Jiang, G. Duan, E. Zussman, A. Greiner and S. Agarwal, *ACS Applied Materials & Interfaces*, 2014, **6**, 5918-5923.
11. L. Chen, S. Jiang, J. Chen, F. Chen, Y. He, Y. Zhu and H. Hou, *New Journal of Chemistry*, 2015, **39**, 8956-8963.

5. Appendix

5.2 Low Density, Thermally Stable, and Intrinsic Flame Retardant Poly(bis(benzimidazo)Benzophenanthrolinedione) Sponge

Jian Zhu, Shaohua Jiang, Haoqing Hou, Seema Agarwal, Andreas Greiner. Low Density, Thermally Stable, and Intrinsic Flame Retardant Poly (bis (benzimidazo) Benzophenanthroline-dione) Sponge. *Macromolecular Materials and Engineering*, **2018**, 303(4), 1700615.

Low Density, Thermally Stable, and Intrinsic Flame Retardant Poly(bis(benzimidazo)Benzophenanthroline-dione) Sponge

Jian Zhu, Shaohua Jiang, Haoqing Hou,* Seema Agarwal,* and Andreas Greiner*

Low density ($\leq 13.9 \text{ mg cm}^{-3}$), compressible poly(bis(benzimidazo)benzophenanthroline-dione) (BBB) sponges with high temperature resistance are reported. The processing of BBB is limited due to its insolubility in organic solvents and infusibility. Therefore, the sponges are made in two steps: first, the BBB fibers are prepared by electrospinning the starting monomers with a template polymer followed by polycondensation of monomers on solid fibers at high temperature. In the second step, the BBB fibers are mechanically cut and self-assembled from a dispersion during freeze-drying. The use of poly(vinyl alcohol) is critical in getting self-assembled hierarchically double-pore-structured, mechanically stable sponges. The sponges show very high pyrolytic stability, high compressibility (more than 92% recovery after 50% compression), very low thermal conductivity ($0.028\text{--}0.038 \text{ W mK}^{-1}$), and high oil absorption capacity.

1. Introduction

Low density 3D sponges with high porosity, gas permeability, mechanical stability, and special wetting characteristics have attracted great interests in tissue engineering,^[1,2] microbial fuel cells,^[3] oil adsorption,^[4,5] and oil-water separation.^[6,7] Sol-gel process, template growth, self-assembly, and 3D printing are common methods to build open-cell sponges. The fabrication methods, selected properties, and the applications of low density macroporous sponges are recently reviewed.^[8] Large

specific surface area, controllable aspect ratio and morphology, versatility and easy modification endow electrospun fiber unique advantages to fabricate 3D sponge materials, which not only broaden the applications of electrospun nanofibers but also provide varying properties to the sponges. Series of electrospun polymer nanofibers including polyacrylonitrile,^[9] polyimide (PI),^[10,11] and polyacrylate-based polymer^[12–14] has been used to assemble mechanical stable 3D sponges with numerous applications. Biodegradable polymer sponges, poly(lactic acid),^[15] polycaprolactone,^[16] and poly(vinyl alcohol) (PVA),^[17] were also prepared using similar approach, which showed applications in tissue engineering. However, these polymer-based sponges have the common

drawback of poor thermal properties which limits their application in high temperature areas. Therefore, aromatic PI sponges were developed which exhibited superior thermal resistance and showed initial degradation temperature above 400 and 500 °C in air and nitrogen, respectively.^[10,11] In spite of good thermal stability and thermal insulation, the PI sponges are flammable and lose their sponge morphology immediately under flame.

Poly(bis(benzimidazo)benzophenanthroline-dione) (BBB) (refer **Scheme 1** for the structure) is a ladder type rigid-rod polymer with a lot of aromatic and heterocyclic rings in backbone which makes it thermal and chemical resistant robust material.^[18–20] These properties make BBB a strong candidate for preparation of high temperature stable, intrinsic flame retardant sponge. However, the investigation and application of BBB has not moved forward for a long period, due to its insolubility and infusibility. Recently, a new approach for making BBB fibers was reported by electrospinning the corresponding monomers with a template polymer followed by solid-state polymerization at high temperature with simultaneous pyrolysis of the template polymer.^[21]

In the present work, the processing of BBB fibers to the corresponding low density, elastic mechanically stable, and hydrophobic sponges is reported. The BBB sponges are compressible, thermally stable (till about 600 °C in N₂), thermally insulating, and intrinsic flame retardant. In addition, these sponges can absorb huge amounts of organic solvents and oil and can be used for many cycles.

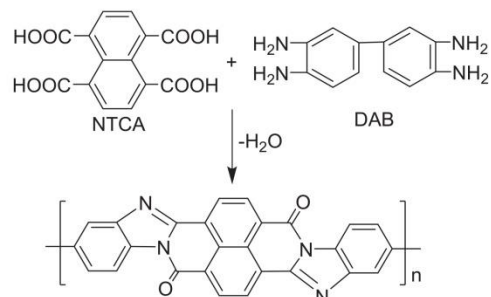
J. Zhu, Prof. S. Agarwal, Prof. A. Greiner
Macromolecular Chemistry II and Bayreuth Center
for Colloids and Interfaces
University of Bayreuth
Universitätsstrasse 30, 95440 Bayreuth, Germany
E-mail: agarwal@uni-bayreuth.de; greiner@uni-bayreuth.de

Prof. S. Jiang
College of Materials Science and Engineering
Nanjing Forestry University
Nanjing 210037, China

Prof. H. Hou
College of Chemistry and Chemical Engineering
Jiangxi Normal University
Nanchang 330022, China
E-mail: haoqing@jxnu.edu.cn

 The ORCID identification number(s) for the author(s) of this article can be found under <https://doi.org/10.1002/mame.201700615>.

DOI: 10.1002/mame.201700615



Poly((benzimidazobenzophenanthroline-dione) (BBB))

Scheme 1. Synthesis and chemical structure of BBB polymer. NTCA = 1,4,5,8-naphthalene tetracarboxylic acid, DAB = 3,3'-diaminobenzidine.

2. Experimental Section

2.1. Materials

3,3'-diaminobenzidine (DAB) (99%, Sigma Aldrich), 1,4,5,8-naphthalene tetracarboxylic acid (NTCA) (98%, Zhengzhou Alfa Chemical Co., China), poly(vinyl pyrrolidone) (PVP, $M_w = 360\,000\text{ g mol}^{-1}$, Carl Roth), poly(vinyl alcohol) (PVA, $M_w = 67\,000\text{ g mol}^{-1}$, Sigma Aldrich), *N,N*-dimethylformamide (DMF, 99.9%, Sigma Aldrich), and 1,4-dioxane (99%, Sigma Aldrich) were used without further purification.

2.2. Preparation of BBB Nanofibers

The BBB nanofibers can be produced by electrospinning as described in the previous literature.^[21] Equimolar amounts of the two monomers, 3,3'-diaminobenzidine (DAB) (2.1427 g, 0.01 mol) and 1,4,5,8-naphthalene tetracarboxylic acid (NTCA) (3.0421 g, 0.01 mol), and 2.22 g PVP was added in 30 g DMF and stirred for 8 h at room temperature to form a homogeneous solution. The total concentration of the solution was about 25 wt% ($m_{\text{DAB+NTCA}}: m_{\text{PVP}} = 7:3$). The electrospinning process was performed with an applied voltage of 15 kV, a collecting distance of 20 cm, and a feeding rate of 1.0 mL h⁻¹. A planar aluminum foil was used to collect the electrospun fibers. The nanofiber mat obtained after electrospinning was dried for 12 h at 40 °C in vacuum oven. The fiber mat was heat treated in argon atmosphere using the following temperature program: (1) heating to 150 °C (10 °C min⁻¹) and annealing for 1 h; (2) heating to 250 °C (10 °C min⁻¹) and annealing for 1 h; (3) heating to 500 °C and annealed at this temperature for 1 h. The heat treatment was performed to condense DAB and NTCA for the formation of BBB polymer on the fiber strand.

2.3. Preparation of BBB Sponges

BBB (2.5 g) fiber mat and 500 mL 1,4-dioxane were put in an electric mixer (Robot Coupe Blixer 4, Rudolf Lange GmbH &

Co. KG) for cutting. The mixer was operated 10 times for 30 s each. The BBB short fibers were collected and freeze-dried for 24 h. Two kinds of BBB sponges were prepared by freeze-drying. A certain amount of BBB short fibers (20–120 mg) were weighed and dispersed in 10 mL deionized water by ultrasonic for 30 min to form a homogeneous BBB short fiber suspension. The short fiber suspensions were freeze-dried in cylindrical glass vials with an inner diameter of 18 mm for 48 h. The sponges were designated as S-BBB. The density of the sponges could be controlled by changing the concentration of the BBB short fibers in the suspensions. The second kind of BBB sponges was made by freeze-drying suspensions of short BBB fibers in dilute PVA solution (0.5–6 mg mL⁻¹) instead of deionized water to form PVA–BBB composite sponge, followed by heat treatment at 500 °C for 30 min. The heating at high temperature pyrolyzed the PVA and the provided BBB sponges were designated as A-BBB sponge. The details about composition of the suspension and corresponding density of the sponges are shown in **Table 1**.

2.4. Characterization

The structural characterization of the BBB fibers and the sponges was done by Fourier transform infrared (FTIR, Digilab Excalibur FTS-3000) spectroscopy. The morphology of the fibers and sponges was observed by scanning electron microscope (SEM, Zeiss Leo 1530). The compression resistance and elasticity of the sponges were detected by mechanical compression machine with a compressing speed of 4 mm min⁻¹ in air at room temperature. Thermogravimetric analysis (TGA) was used to explore the thermal stability of the BBB sponges under nitrogen and air at a heating rate of 10 °C min⁻¹. The hydrophobicity of the sponges was determined by contact angle measurement with 80 µL water drop. Thermal conductivity measurements were carried out using Hot Disk Thermal Constants Analyzer (TPS 2500S).

Table 1. Details about the composition of the suspensions and corresponding density of sponges.

Sample No.	BBB fibers [mg]	PVA [mg mL ⁻¹]	Volume of suspension [mL]	Density [mg cm ⁻³]
S-BBB-1	20	0	10	2.9
S-BBB-2	40	0	10	5.7
S-BBB-3	80	0	10	10.8
S-BBB-4	120	0	10	16.4
A-BBB-1	40	0.5	10	5.5
A-BBB-2	40	1	10	5.7
A-BBB-3	40	2	10	5.2
A-BBB-4	40	4	10	5.8
A-BBB-5	40	6	10	6.9
A-BBB-6	60	4	10	8.5
A-BBB-7	80	4	10	9.8
A-BBB-8	120	4	10	13.9

3. Results and Discussion

It has been shown in the past that large aspect ratio electrospun polymer short fibers can form ultralow density 3D porous sponges by percolation and self-assembly of short fibers in the suspension during freeze-drying.^[9–17] The present work aimed at making high temperature stable and intrinsic flame retardant sponges. BBB is one of the interesting polymers fulfilling these requirements. It is a thermal resistance robust ladder type rigid-rod polymer with many aromatic and heterocyclic rings in backbone. Since it is insoluble and infusible polymer, the processing of this polymer requires special procedures. Recently, a new approach of making BBB fibers by electrospinning of the corresponding monomers and subsequent polymerization in the solid-state was reported.^[21] The BBB fibers made by this procedure have a smooth surface and uniform diameter in range of 700–800 nm as shown in **Figure 1a,b**. After mechanical cutting, the obtained short BBB fibers possessed a length distribution in the range of 50–500 μm (**Figure 1c,d**).

The sponges (S-BBB) made by simply freeze-drying of BBB short fiber dispersions (insert in 1c) were fragile and were easy to break. **Figure 2a,b** shows the SEM images of S-BBB sponge in which the BBB short fibers were stacked randomly without any 3D self-assembled order. S-BBB sponges were unstable and could be redispersed in organic solvents. To solve this problem, water-soluble polymer PVA was chosen as a template polymer that directed the self-assembly of BBB fibers to a highly stable nonfragile 3D sponge structure. The sponges were further annealed at 500 $^{\circ}\text{C}$ for pyrolysis of the template polymer (PVA) and to get template-free BBB sponges. Although, PVA was used in this work as the template polymer, but other water-soluble

polymers, such as PVP and poly(ethylene oxide) should work equally well. The annealing temperature is chosen in a way that the template polymer is completely removed by degradation. The sponges before and after annealing were named as PVA-BBB and A-BBB sponge, respectively. **Figure 2c–f** shows the SEM images of PVA-BBB-4 sponge and A-BBB-4 sponge, as well as photos of these sponges. A hierarchical ordered dual pore structure was very obvious from these pictures which were maintained even after annealing. The sponges had large pores (more than 100 μm) and small pores <5–10 μm .

The chemical structures of the BBB nanofibers and PVA-BBB sponge, as well as A-BBB sponge after heat treatment, were determined by FTIR spectra (**Figure 3a**). Comparing the characteristic absorptions at 1698, 1547, and 992 cm^{-1} with previous report, the formation of BBB polymer and the retained molecular structure even after heat treatment were proved.^[21] The characteristic absorptions of PVA at 3313 and 2917 cm^{-1} belonging to $-\text{OH}$ and $\text{C}-\text{H}$ disappeared after heat treatment at 500 $^{\circ}\text{C}$, signifying successful removal of PVA by pyrolysis. TGA (**Figure 3b**) of PVA powder also showed more than 95% degradation of PVA at 500 $^{\circ}\text{C}$. TGA showed very high thermal stability of BBB sponge (**Figure 3c**): the temperature at which there was a mass loss of 5 wt% was 655 $^{\circ}\text{C}$ in N_2 atmosphere and 490 $^{\circ}\text{C}$ in air. Pyrolysis of BBB led to very high char of more than 80%.

Figure 4a,b and Videos S1 and S2 in the Supporting Information show the qualitative compression test of S-BBB sponge and A-BBB sponge with similar density of nearly 5.8 mg cm^{-3} (S-BBB-2 and A-BBB-4). S-BBB sponge only reverts to 69% after maximum compression of 80% and loss elasticity after compressing for 3 times. In contrast, the final A-BBB sponge was compressively highly stable; more than 95% size recovery was

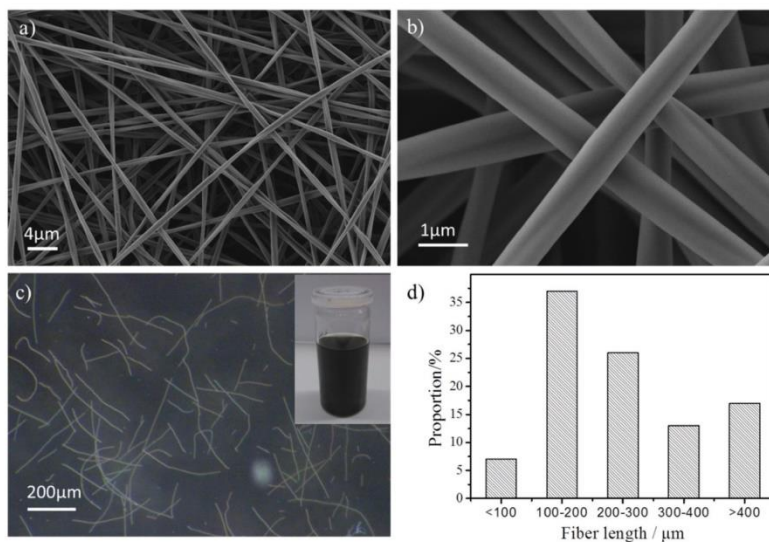


Figure 1. SEM images of a,b) electrospun BBB fibers, c) microphotograph of BBB short fibers, and length distribution of BBB short fibers.

5. Appendix

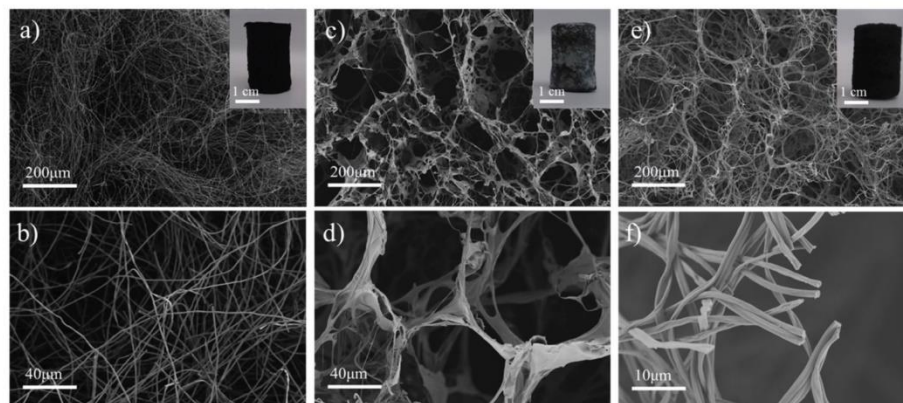


Figure 2. SEM images and photos of a,b) S-BBB sponge (sample S-BBB-2, Table 1), c,d) PVA-BBB sponge (sample PVA-BBB-4, Table 1), and e,f) A-BBB sponge (sample A-BBB-4, Table 1).

there after a very high compression of 80%, and after 50 cycles, the recovery was more than 90%. Compressive strength at different strain rates is shown in Figure 4c–e. Some important conclusions can be drawn from this data: (1) the compressive strength increased with increase in the density; the sponges with densities as low as 10–17 mg cm⁻³ showed good compressibility, (2) use of PVA during sponge preparation had a significant influence on sponge stability and compressibility,

even if density of the sponge was not changed significantly, (3) optimum amount of PVA was required to get stable sponges (4 mg mL⁻¹), and (4) increase in the concentration of PVA during sponge preparation could enhance the compression strength of final A-BBB sponges. The compressive strength at 50% compression of A-BBB sponge was 2.6 times more compared to that of S-BBB sponge with similar density nearly 5.8 mg cm⁻³ (compare samples S-BBB-2 and A-BBB-4, Table 1)

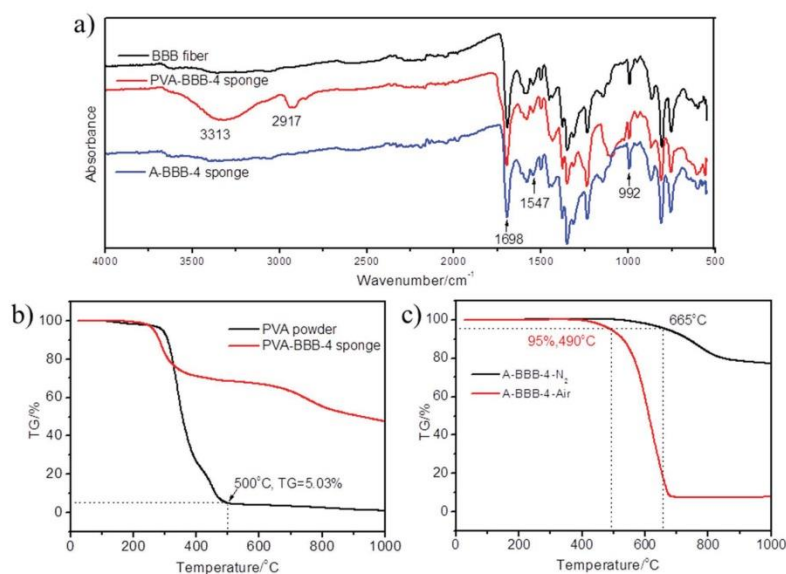


Figure 3. a) FTIR spectra of BBB fiber, PVA-BBB-4 sponge, and A-BBB-4 sponge. b) TGA curves of PVA powder and PVA-BBB-4 sponge in N₂ atmosphere. c) TGA curves of A-BBB-4 sponge in air and N₂ condition.

5. Appendix

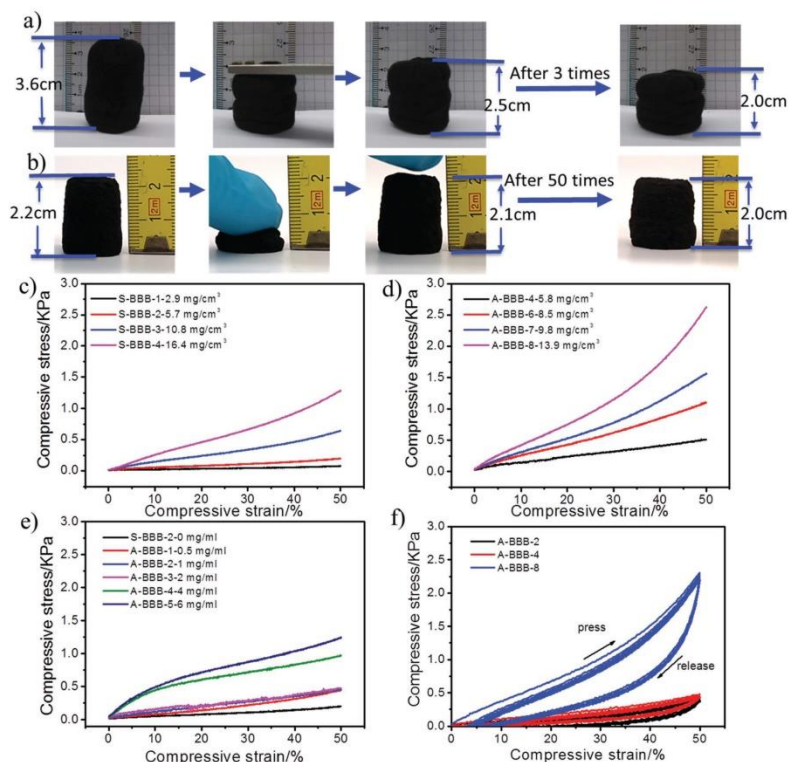


Figure 4. a,b) Qualitative compressive test of S-BBB sponge and A-BBB sponge. c) Compressive curves of S-BBB sponges with different density. d) Compressive curves of A-BBB sponges with different density. e) Compressive curves of A-BBB sponges prepared with different concentration PVA solution (0–6 mg mL⁻¹). f) Cycle compressive measurement of A-BBB sponges.

when 4 mg mL⁻¹ PVA solution was used. This shows the effect of bimodal porous sponge structure generated due to PVA in providing stability to the sponges.

In order to investigate the elasticity of the A-BBB sponges, 6 loading–unloading cycles to a maximum compression of 50% were tested. The results (Figure 4f) show that the elasticity improves with increase in density of the A-BBB sponge, which was changed by the concentration of short BBB fibers in the suspension or increasing the concentration of PVA solution for A-BBB sponges. The A-BBB-2 sponge with a density of 5.7 mg cm⁻³ and prepared with 1 mg mL⁻¹ PVA solution recovers to 80% after 6 times test. When PVA concentration was increased to 4 mg mL⁻¹ (sample A-BBB-4, density 5.8 mg cm⁻³), the sponge recovers to 92%. Further increase in the density to 13.9 mg cm⁻³ by keeping the amount of PVA same but by increasing the amount of short fibers in the dispersion (sample A-BBB-8), the recovery reaches to 95% after 6 cycles. Consequently, the stable and elastic A-BBB sponges are more suitable for practical applications and further investigated for thermal conductivity, isolation, and solvent uptake property.

The thermal conductivity of stable A-BBB sponges was measured in Hot Disk Thermal Constants Analyzer under air, and the results were shown in Figure 5a,b. The A-BBB sponges showed very low thermal conductivity in the range of 0.028–0.038 W mK⁻¹. With increase in density, the thermal conductivity increased from 0.028 to 0.038 W mK⁻¹. This is very close to the value of air (0.025 W mK⁻¹) at room temperature (20 °C). This is because of very high porosity of the 3D sponge (more than 99% is air). Thermal diffusivity α was calculated from Equation (1)

$$\alpha = \frac{\lambda}{\rho c} \quad (1)$$

λ , ρ , and c are thermal conductivity, density, and specific heat capacity of the material. There was a sharp increase in ρc of the sponge on increasing the density because of superior specific heat capacity of BBB fibers, which means more thermal heat was absorbed by the sponge thus hinder the heat diffusion on temperature rise. So even though the thermal conductivity of the A-BBB sponge increased slightly, but the thermal

5. Appendix

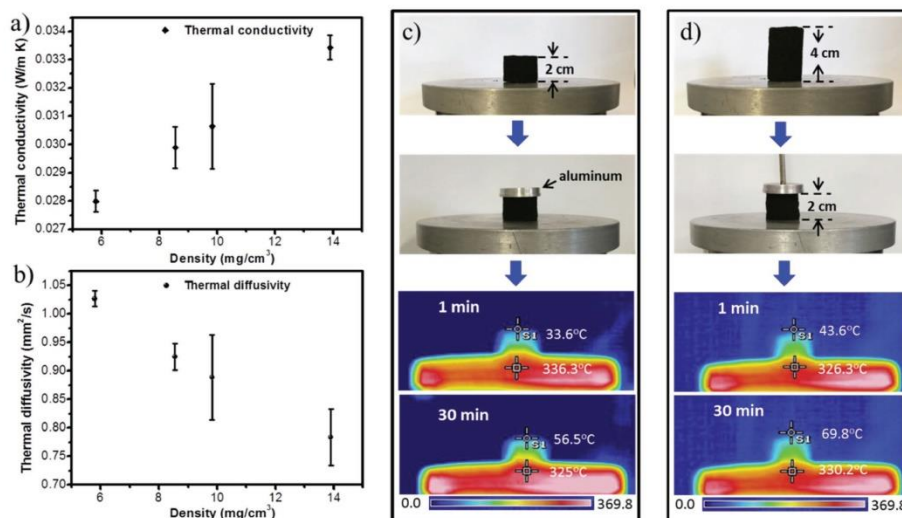


Figure 5. a) Thermal conductivity and b) thermal diffusivity of A-BBB sponge changes with density. The samples were prepared with 4 mg mL⁻¹ PVA solution. c,d are digital photos and IR camera photos of A-BBB-7 sponge and 50% compressed A-BBB-7 sponge at high temperature plate.

diffusivity decreased with the increase in density (Figure 5b). In order to investigate the thermal insulation property of the A-BBB sponge, A-BBB-7 sponge in cylindrical form (diameter 2.4 cm and height 2 cm) with density of about 10 mg cm⁻³ was put on a hot plate heated to ≈330 °C (Figure 5c). A 12 g aluminum plate was put on the top of the sponge. The actual temperature was detected on top of the aluminum plate with a Thermal Infrared Camera. The temperature of the aluminum plate was only 56 °C after heated through the A-BBB sponge for 30 min, which demonstrated the outstanding thermal insulation property and further proved the low thermal conductivity. On the other hand, the compressed A-BBB-7 sponge showed larger thermal conductivity, and result in the slight increase in the temperature of the aluminum plate to 70 °C after 30 min (Figure 5d). The thermal insulation property and thermal stability of A-BBB sponges are very similar to that of the PI sponge recently reported.^[10]

In a previous study, the PI nanofiber membrane showed neither a real ignition nor flaming combustion but rather a thermo-oxidative decomposition process. The surface of the nanofiber fabrics exhibited only small surface flames and glowing until the nanofibers were completely consumed and no residue remained.^[22] In the present work, the prechecking with a tealight showed superior flame retardant property of A-BBB sponge in comparison to the commercially available polystyrene (PS) and nanofibrous PI sponge (Figure 6). The PS sponge sustained flame and immediately lost its form. The PI nanofibrous sponge also ignite fast in tealight as shown in Figure 5b, sustained flame and lost shape. In comparison, the A-BBB sponge did not show any sustained ignition, negligible shrinkage, or smoke release.

Contact angle measurement was adopted to investigate the hydrophobicity and lipophilicity of BBB sponges. A-BBB

sponges were hydrophobic with contact angle larger than 135° as shown in Figure 7a because of the porous structure. Due to crosslinked network structure and intrinsic ultrastrong solvent resistance property of BBB polymer, A-BBB sponges are stable in water and a series of organic solvents (Figure 7b,c). A-BBB sponges float on the surface of the water on account of low density and hydrophobicity.

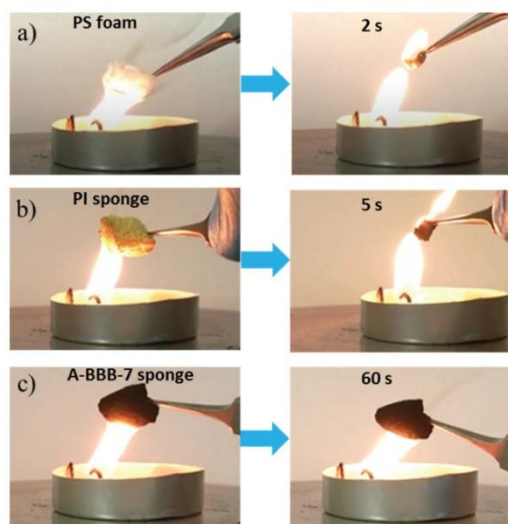


Figure 6. Photos of a) PS sponge, b) PI sponge, and c) A-BBB-7 sponge put on the fire.

5. Appendix

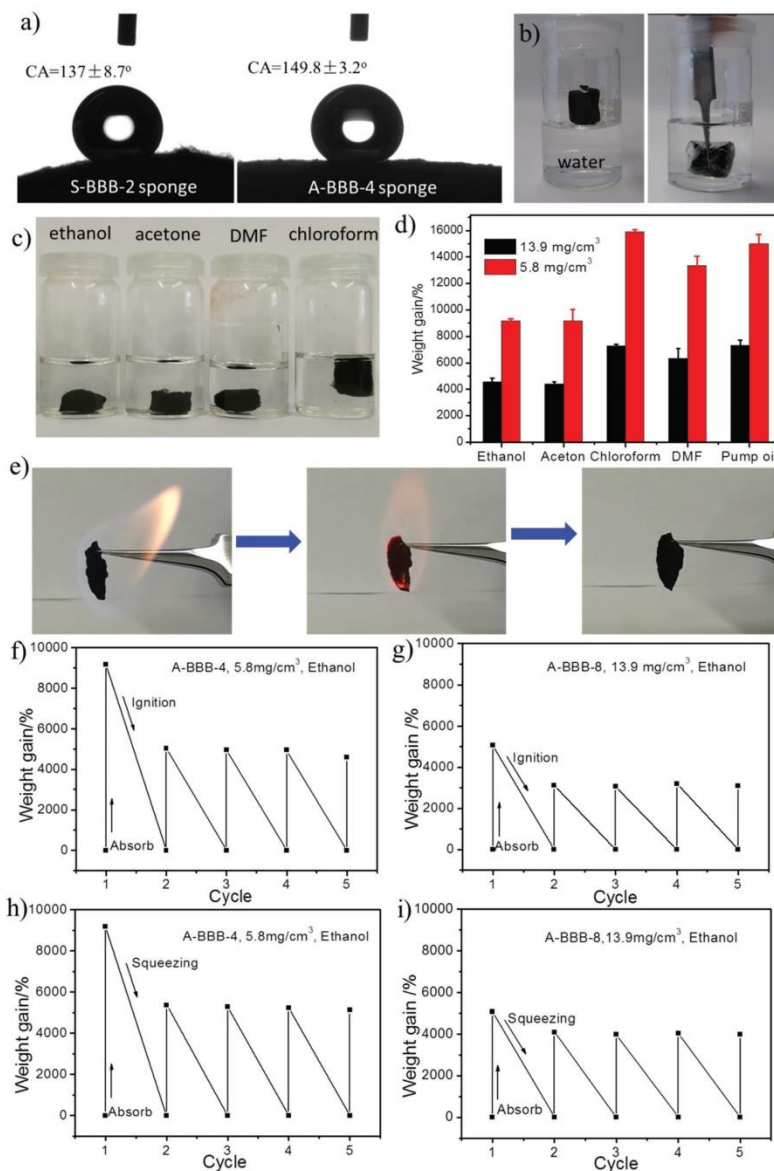


Figure 7. a) Contact angle measurement of S-BBB-2 sponge and A-BBB-4 sponge. b) Photos of A-BBB-4 sponge in the surface and interior of water. c) Photos of A-BBB-4 sponge in series organic solvent. d) Organic solvent uptake efficiency for the first time of A-BBB-4 and A-BBB-8 sponges for various organic liquids. Weight gain here is defined as the weight ratio of the absorbate to the dried A-BBB sponge. e) Photographs showing the process of recycling A-BBB sponge via ignition. f–i) Recyclability study of A-BBB sponges for sorption capacity of ethanol. f, g) Ignition applied to remove ethanol absorbed in A-BBB sponge, h, i) squeezing was used to remove ethanol absorbed in A-BBB sponge.

The 3D porous open-cell structure, good mechanical property, and lipophilicity of A-BBB sponge make it an ideal candidate for absorption of organic solvents. The absorption capacity of A-BBB

sponge is reflected in the weight gain (wt%) which is defined as the weight of absorbed substance per unit weight of the dried A-BBB sponge. Various kinds of organic solvent (ethanol,

acetone, chloroform, and DMF) and pump oil were studied in this research. A-BBB sponge reveals a high sorption capacity for the first time up to 43–159 times its own weight of abovementioned solvents (Figure 7d). This sorption capacity is higher than many previously reported materials such as wool-based nonwoven (9–15 times),^[23] microporous polymer (5–25 times),^[24] nanowire membrane (4–20 times),^[25] magnetic exfoliated graphite (30–50 times),^[26] spongy graphene (20–86 times),^[27] even bear comparison with some carbon nanotubes sponge (25–125 times),^[28] and carbon fiber aerogel (50–192 times),^[29] although still lower than part of nitrogen-doped graphene foam,^[30] ultra-lightweight aerogels.^[5] Sponges with lower densities usually have higher liquid sorption capacity because of the larger pore volume. The intrinsic chemical stability, thermal stability, and intrinsic flame retardancy of the sponges make it possible to remove the up taken solvent by ignition and reuse the sponge for sorption of solvent again. The sorption capacities were maintained at 54.6% and 61.5% in subsequent cycles, i.e., on reuse after solvent removal by ignition for 5.8 and 13.9 mg cm⁻³ A-BBB sponges, respectively (Figure 7e–g, Video S3, Supporting Information). During ignition, A-BBB sponge shrunk slightly which could be the reason for the decreasing sorption capacity after first cycle. Simple squeezing is another effective way to remove the up taken solvent. The 58.6% and 78.5% solvents were recovered from sponges with densities 5.8 and 13.9 mg cm⁻³ (Figure 7h–i), respectively, which are higher than ignition method.

4. Conclusions

BBB low density (≤ 13.9 mg cm⁻³), compressible, intrinsic flame retardant, thermal insulating sponges with high temperature resistance are reported. BBB processing is not straightforward due to its insolubility and infusibility. We presented the preparation method of BBB sponges using two-step process. The sponge preparation required use of a sacrificial glue, such as PVA. It helped in getting self-assembled hierarchically double-pore-structured, mechanically stable sponges. The sponges were thermally stable with more than 80% char formation. They were compressible (sponge with density of 5.8 mg cm⁻³ showed more than 92% recovery after 50% compression for 6 cycles). The thermal conductivity was in the range of 0.028–0.038 W mK⁻¹ and oil absorption capacity as high as 159 times of its own mass depending upon the density.

Supporting Information

Supporting Information is available from the Wiley Online Library or from the author.

Acknowledgements

The authors acknowledge DFG (SFB840) for financial support.

Conflict of Interest

The authors declare no conflict of interest.

Keywords

flame retarded, polybisbenzimidazobenzophenanthroline-dione, sponge, thermal resistance

Received: December 1, 2017

Revised: January 27, 2018

Published online:

- [1] G. Zhao, X. Zhang, T. J. Lu, F. Xu, *Adv. Funct. Mater.* **2015**, *25*, 5726.
- [2] W. Cui, Y. Zhou, J. Chang, *Sci. Technol. Adv. Mater.* **2010**, *11*, 014108.
- [3] S. Chen, H. Hou, F. Harnisch, S. A. Patil, A. A. Carmona-Martinez, S. Agarwal, Y. Zhang, S. Sinha-Ray, A. L. Yarin, A. Greiner, *Energy Environ. Sci.* **2011**, *4*, 1417.
- [4] S. Huang, X. Li, Y. Jiao, J. Shi, *Ind. Eng. Chem. Res.* **2015**, *54*, 1842.
- [5] H. Sun, Z. Xu, C. Gao, *Adv. Mater.* **2013**, *25*, 2554.
- [6] H. Wang, E. Wang, Z. Liu, D. Gao, R. Yuan, L. Sun, Y. Zhu, *J. Mater. Chem. A* **2015**, *3*, 266.
- [7] Y. Gao, Y. S. Zhou, W. Xiong, M. Wang, L. Fan, H. Rabiee-Golgir, L. Jiang, W. Hou, X. Huang, L. Jiang, *ACS Appl. Mater. Interfaces* **2014**, *6*, 5924.
- [8] S. Jiang, S. Agarwal, A. Greiner, *Angew. Chem., Int. Ed.* **2017**, *56*, 15520.
- [9] Y. Si, J. Yu, X. Tang, J. Ge, B. Ding, *Nat. Commun.* **2014**, *5*, 5802.
- [10] S. Jiang, B. Uch, S. Agarwal, A. Greiner, *ACS Appl. Mater. Interfaces* **2017**, *9*, 32308.
- [11] S. Jiang, S. Reich, B. Uch, P. Hu, S. Agarwal, A. Greiner, *ACS Appl. Mater. Interfaces* **2017**, *9*, 34286.
- [12] G. Duan, S. Jiang, V. Jérôme, J. H. Wendorff, A. Fathi, J. Uhm, V. Altstädt, M. Herling, J. Breu, R. Freitag, *Adv. Funct. Mater.* **2015**, *25*, 2850.
- [13] G. Duan, S. Jiang, T. Moss, S. Agarwal, A. Greiner, *Polym. Chem.* **2016**, *7*, 2759.
- [14] S. Jiang, G. Duan, U. Kuhn, M. Mörl, V. Altstädt, A. L. Yarin, A. Greiner, *Angew. Chem.* **2017**, *129*, 3333.
- [15] W. Chen, J. Ma, L. Zhu, Y. Morsi, E.-H. Hany, S. S. Al-Deyab, X. Mo, *Colloids Surf., B* **2016**, *142*, 165.
- [16] T. Xu, J. M. Miszuk, Y. Zhao, H. Sun, H. Fong, *Adv. Healthcare Mater.* **2015**, *4*, 2238.
- [17] F. Deuber, S. Mousavi, M. Hofer, C. Adlhart, *ChemistrySelect* **2016**, *1*, 5595.
- [18] R. Van Deusen, *J. Polym. Sci., Part C* **1966**, *4*, 211.
- [19] F. Arnold, R. Van Deusen, *Macromolecules* **1969**, *2*, 497.
- [20] G. Berry, *J. Polym. Sci., Part B* **1976**, *14*, 451.
- [21] J. Zhu, Y. Ding, S. Agarwal, A. Greiner, H. Zhang, H. Hou, *Nanoscale* **2017**, *9*, 18169.
- [22] E. Gallo, Z. Fan, B. Schartel, A. Greiner, *Polym. Adv. Technol.* **2011**, *22*, 1205.
- [23] M. M. Radetic, D. M. Jovic, P. M. Jovancic, Z. L. Petrovic, H. F. Thomas, *Environ. Sci. Technol.* **2003**, *37*, 1008.
- [24] A. Li, H.-X. Sun, D.-Z. Tan, W.-J. Fan, S.-H. Wen, X.-J. Qing, G.-X. Li, S.-Y. Li, W.-Q. Deng, *Energy Environ. Sci.* **2011**, *4*, 2062.
- [25] J. Yuan, X. Liu, O. Akbulut, J. Hu, S. L. Suib, J. Kong, F. Stellacci, *Nat. Nanotechnol.* **2008**, *3*, 332.
- [26] M. O. Adebajo, R. L. Frost, J. T. Klopogge, O. Carmody, S. Kokot, *J. Porous Mater.* **2003**, *10*, 159.
- [27] G. Wang, Q. Sun, Y. Zhang, J. Fan, L. Ma, *Desalination* **2010**, *263*, 183.
- [28] D. P. Hashim, N. T. Narayanan, J. M. Romo-Herrera, D. A. Cullen, M. G. Hahm, P. Lezzi, J. R. Suttle, D. Kelkhoff, E. Munoz-Sandoval, S. Ganguli, *Sci. Rep.* **2012**, *2*, 363.
- [29] H. Bi, Z. Yin, X. Cao, X. Xie, C. Tan, X. Huang, B. Chen, F. Chen, Q. Yang, X. Bu, *Adv. Mater.* **2013**, *25*, 5916.
- [30] Y. Zhao, C. Hu, Y. Hu, H. Cheng, G. Shi, L. Qu, *Angew. Chem.* **2012**, *124*, 11533.

5. Appendix

5.3 Gradient-Structured Nonflammable Flexible Polymer Membranes

Jian Zhu, Josef Breu, Haoqing Hou, Andreas Greiner, Seema Agarwal. Gradient structured nonflammable flexible polymer membranes. *ACS applied materials & interfaces*, **2019**, 11 (12), 11876-11883.

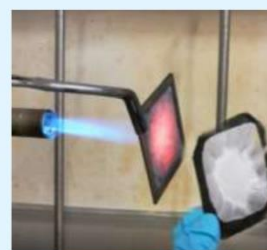
Gradient-Structured Nonflammable Flexible Polymer Membranes

Jian Zhu,[†] Josef Breu,[‡] Haoqing Hou,[§] Andreas Greiner,[†] and Seema Agarwal^{*,†}[†]Macromolecular Chemistry and Bavarian Polymer Institute and [‡]Inorganic Chemistry and Bavarian Polymer Institute, University of Bayreuth, Universitätsstraße 30, Bayreuth 95447, Germany[§]College of Chemistry and Chemical Engineering, Jiangxi Normal University, Nanchang 330022, China

Supporting Information

ABSTRACT: Herein, we report the formation and properties of a rare example of high-performance composite membranes from polybisbenzimidazobenzophenanthroline-dione (BBB) that do not sustain a flame or burn with smoke nor show melt dripping. In addition, this material possesses a low density and very high thermal stability (char yield as high as 80–94%), strength, and flexibility. Such membranes are highly desirable for battery separators, protective clothing, construction, and automobiles. Because BBB is an insoluble and infusible polymer, the composite membranes were made using a bottom-up vacuum-assisted self-assembly method with an aqueous dispersion of short BBB fibers and Hec. The use of water as the solvent, upscalability, and excellent flame retardancy in combination with low density, flexibility, and low thermal conductivity of the composite membranes make the preparation method and membranes highly promising for future use in real applications.

KEYWORDS: nonflammable, polybisbenzimidazobenzophenanthroline-dione, hectorite, gradient structure, electrospinning, short fibers



INTRODUCTION

The flammability of polymers is one of the limitations with regard to their use in several applications, ranging from day-to-day use in furniture and households to other demanding applications (i.e., automobile, aircraft, construction, and protective clothing).^{1,2} In the past, several innovative solutions have been reported to address this challenge and improve the heat and flame resistance of polymers.^{3–5} Copolymers with flame-retardant units,^{6,7} organic additives,^{8–10} and inorganic fillers^{11–14} are the most commonly used materials for improving the flame-retardant characteristics of polymers. Using these measures, the fire retardancy can be improved to varying extents depending on the amount, type, and method of application of additives and fillers. Several new questions have arisen regarding the toxicity, leaching, and efficiency of the additives.^{15–18}

Layered silicate–polymer composites have been extensively studied with a focus on improved fire retardancy with superior mechanical properties without the toxicity and leaching issues.^{3,19–23}

Despite the large number of studies, Papaspyrides concluded in a recent review that the composites do not outperform matrix polymers in some flammability tests (UL94V and the limiting oxygen index (LOI)).¹⁹ There is a need of additional flame-retardant additives for thermoplastic polymer–layered silicate composites. The mechanism for flame retardancy in the composites is primarily because of the continuous crust and barrier formation by layered silicates, and therefore, the process of polymer mass loss slows down but does not stop completely.^{24–26} The same is true for the total heat release

which does not decrease but rather is spread out over a longer time with a concomitant reduction of the peak of heat release rate. Therefore, the material burns less intensely over a longer period of time.

Another approach for making polymers intrinsically fire-resistant by introducing aromatic units, heterocyclic rings, and phosphorous units also works but to a limited extent.¹⁰ These materials have self-extinguishing properties with an LOI higher than 21 vol % but require additional flame retardants to improve flame retardancy in several cases.^{5,27,28} High-performance polymers (HPPs), such as polyamides,²⁹ polybenzimidazole (PBI),³⁰ and polyimide,^{28,31} have high degradation temperatures and self-extinguishing properties because of their highly rigid backbones and strong chain-to-chain interactions. Poly-(PBO) (trade name Zylon) is a highly thermally stable polymer in air with excellent flame-resistant properties, high LOI of 68 vol %, longer ignition time, low rate of heat release, and less smoke.^{32,33} In addition, PBIs are thermally stable polymers (degradation temperature 580 °C in air; LOI 41 vol %) with very high glass transition temperatures (450 °C) that are prepared by the condensation of aromatic bis-*o*-diamines and dicarboxylates.³⁴ These polymers exhibit a negligible heat release rate on burning and release little smoke prior to decomposition with the release of water, carbon oxides, and traces of hydrogen cyanide.^{34,35} Other rigid rod polymers, such as poly(2,6-

Received: December 19, 2018

Accepted: February 28, 2019

Published: February 28, 2019

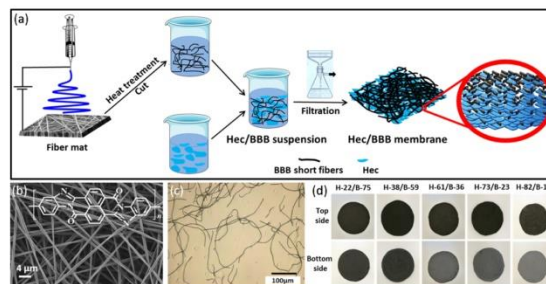


Figure 1. (a) Preparation process for the Hec/BBB membranes. (b) SEM image of the BBB fiber mat. Inset shows the repeat unit structure of the BBB macromolecule. (c) Microscope image of BBB short fibers. (d) Digital photos of the Hec/BBB membranes with different weight ratios.

diimidazo(4,5-*b*:4',5'-*e*)pyridinylene-1,4(2,5-dihydroxyphenylene), also exhibit very good fire-resistant properties.^{34,36}

Insolubility in common organic solvents and very high softening points hinder the processing of all HPPs and their use. Therefore, novel approaches are required to utilize the intrinsic properties of HPPs by eliminating the use of leachable, toxic organic additives for fire retardancy. Poly(bisbenzimidazobenzophenanthroline) (BBB) is a heterocyclic rigid polymer that is synthesized via the polycondensation of 1,4,5,8-naphthalene tetracarboxylic acid (NTCA) and 3,3'-diaminobenzidine (DAB) in polyphosphoric acid at a high temperature (~ 200 °C).^{37,38} Despite the high thermal stability that is similar to all other HPPs, processing is the bottleneck for the use of BBB in any application. The initial challenge for taking advantage of the high heat stability and superior flame resistance of HPPs, such as BBB, is to provide a simple, upscalable, and a low-cost route for processing. Recently, we reported a bottom-up approach for making BBB fibers via solid-state polymerization on a template sacrificial fiber and the corresponding sponges.^{39–41} The method is very simple and involves electrospinning^{42–44} of the initial BBB monomers with a sacrificial low thermally stable polymer, followed by BBB polymerization and removal of the template polymer by annealing at a high temperature.

Herein, we report the formation and properties of a rare example of a high-performance membrane from a layered silicate (sodium hectorite (Hec))⁴⁵ and BBB electrospun short fibers. The membranes were prepared using a wet-laid process^{46,47} with an aqueous dispersion of BBB fibers and Hec. In general, in a wet-laid process, an aqueous dispersion of fibers is deposited by vacuum filtration on a porous substrate and drained to form a network of randomly laid fibers which can be detached from the substrate in the form of a porous fibrous membrane.^{46,47} Our approach that synergistically combined the properties of BBB and Hec in the composite membrane, which is nonflammable, does not sustain flame or burn with smoke. In addition, no melt dripping was observed for this material which possesses a low density and very high thermal stability, flexibility, and strength. The porous fibrous BBB membranes made by the wet-laid process are mechanically weak. The high-aspect ratio of the layered silicate (sodium Hec) sheet was expected to provide efficient physical entanglements of BBB fibers in the composite membranes. Therefore, sodium Hec–BBB composite membranes were studied incorporating the advantageous properties of sodium Hec in improving the mechanical properties and

flammability behavior. Such membranes are highly desirable for demanding applications, such as protective lightweight clothing, automobiles, and construction.

EXPERIMENTAL SECTION

Materials. DAB (99%, Sigma-Aldrich), NTCA (98%, Zhengzhou Alfa Chemical Co., China), and poly(vinyl pyrrolidone) (PVP, $M_w = 360\ 000$, Carl Roth) were used as purchased. Thermoplastic polyurethane (TPU, Desmopan DP 2590, $M_w = 88\ 900$) was a gift from Bayer Materials Science Company. *N,N*-Dimethylformamide (DMF, 99.9%), tetrahydrofuran (THF, $\geq 99.9\%$), and 1,4-dioxane (99%) were purchased from Sigma-Aldrich and used as received. Na Hec with typical diameters of ≈ 20 μm was synthesized from the melt as previously published.¹⁵

Preparation of Electrospun BBB Short Fibers. BBB short fibers were obtained by the mechanical cutting of continuous BBB fibers that were prepared by electrospinning. The direct processing of the BBB polymer into fibers was not possible. Therefore, these fibers were prepared using an indirect method according to our previously published protocol (Figure 1a).^{39,41} Equimolar amounts of DAB (2.1427 g, 0.01 mol) and NTCA (3.0421 g, 0.01 mol) were dissolved in 12 g of DMF at -5 °C and then mixed for 2 h to form a 30 wt % solution. In a separate flask, 2.22 g of PVP was dissolved in 10.6 g of DMF at room temperature. The two solutions were mixed together and stirred for 2 h. Electrospinning was performed at 15 kV, and the solution feed rate was 1.0 mL h^{-1} . The precursor nanofiber mat was collected on a planar aluminum foil at a distance of 20 cm, followed by drying at 40 °C under vacuum for 12 h. A three-step annealing program was used to transform the precursor fibers into BBB fibers under an argon atmosphere. First, the sample was heated to 150 °C (10 °C min^{-1}) and maintained at this temperature for 1 h. In the next step, the temperature was increased to 250 °C (10 °C min^{-1}) and annealed at this temperature for an additional 1 h. Finally, the temperature was increased to 500 °C, and the sample was annealed for 1 h. The heat treatment resulted in the solid-state condensation polymerization of DAB and NTCA on the precursor fiber (Scheme S1). To obtain BBB short fibers, a 2.5 g BBB fiber mat was cut in 500 mL of 1,4-dioxane in an electric mixer (Robot Coupe Blixer 4, Rudolf Lange GmbH & Co. KG) by running the mixer 10 times for 30 s each time. The cut fibers were separated and freeze-dried.

Preparation of Hec/BBB Membranes. A 1 wt % Hec suspension was prepared by dispersing 10 g of Na Hec in 990 mL of deionized water, followed by vigorous stirring for 3 days to form a homogeneous suspension. A representative example of the preparation procedure for a Hec/BBB composite membrane is as follows: 100 mg of BBB short fibers was placed in 90 mL of deionized water and ultrasonicated for 1 h to form a fiber dispersion. To this solution, 10 g of the 1 wt % Hec suspension was added, followed by vigorous shaking for 5 min to obtain a homogeneous suspension. The volume of the final suspension was

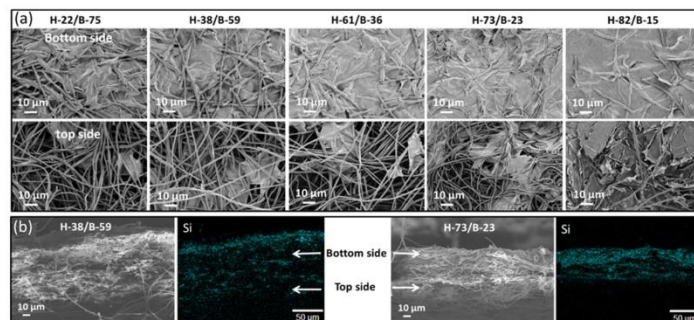


Figure 2. (a) SEM images of the top and bottom sides of the Hec/BBB composite membranes. (b) SEM images and Si atom mapping as obtained by EDXS for a cross section of the Hec/BBB membranes.

controlled to 100 mL. The TPU fiber mats, which were coated onto a circular 325-mesh stainless steel wire (diameter 7.4 cm, area 43 cm²) that was fabricated by electrospinning of 0.4 mL of a 16 wt % TPU solution (DMF/THF 8:2), were used as filters. The diameter of the electrospun TPU fibers ranged from 500 to 1000 nm, and the pore size distribution of the fiber mat was 1–3.8 μm, as shown in the Supporting Information (Figure S1). After filtration, the Hec and BBB short fibers were deposited on the TPU fiber mat to form the composite membrane. After removal of the steel mesh and TPU filter, a self-supported Hec/BBB membrane was obtained and dried at room temperature for 24 h, followed by drying at 60 °C for 6 h. The samples were heated to 800 °C in an air atmosphere in a thermogravimetric analyzer. The remaining mass at 700 °C was taken as the mass of Hec in the composite membrane, and the mass of BBB fibers was obtained from subtracting this mass from the original mass used for the analysis. The resulting membranes are referred to as H-*x*/B-*y*, where H and B represent the Hec and BBB short fibers in the composite membranes, respectively, and *x* and *y* are the mass ratios of the Hec and BBB fibers as determined by TGA. The detailed compositions are given in the Supporting Information (Table S1).

Self-Reinforced Composites. To enhance the stability of the Hec/BBB membrane, in another series of samples, the BBB precursor monomer (DAB + NTCA) solutions with different concentrations (i.e., 1.4, 3.5, and 5.6 wt % in DMF) were coated on the surface of the membrane and then heat-treated at 500 °C. This process ensures an additional coating of BBB on the Hec/BBB fibrous membrane.

Characterization. The morphologies of the Hec/BBB fibrous membranes were observed using a scanning electron microscope (SEM, Zeiss Leo 1530). Energy-dispersive X-ray spectrometry (EDXS) of the Si element was employed to detect the distribution of Hec in the membranes. The studies of the mechanical properties and bending were performed using an electromechanical universal testing machine (Zwick/Roell, BT1-FR0.5TN.D14). The sample dimension for the tensile test was 30 mm in length by 3 mm in width. The tensile speed applied to the samples was 5 mm min⁻¹, and the pristine effective tensile length was 10 mm. The precise contents of Hec and BBB in the composite membranes as well as their thermal stability were determined by thermogravimetric analysis (TGA, TG 209 F1 Libra) at a heating rate of 10 °C min⁻¹. A hot disk thermal constants analyzer (TPS 2500S) with a sensor diameter of 10.48 mm was used to perform the thermal conductivity measurements. The testing time was 20 s at a power of 500 mW. The sensor was sandwiched between two sample pieces that were 40 mm × 40 mm in size and pressed with a 2.49 kg weight. Oxygen Index (Fire Testing Technology, UK) and UL 94 (Fire Testing Technology, UK) were used to test the ignition and flame-shielding properties of the Hec/BBB composite membranes. Cone calorimeter (i Cone, Fire Testing Technology, UK) tests were performed using a power of 35 kW, and the specimens were placed

in an aluminum tray that was located 60 mm from the cone heater. The test time was 5 min for each sample.

Powder X-ray diffraction (XRD) patterns were obtained using nickel-filtered Cu Kα radiation ($\lambda = 1.54187 \text{ \AA}$) on a Bragg–Brentano-type diffractometer (XPRT-PRO, PANalytical B.V.).

RESULTS AND DISCUSSION

A series of Hec/BBB composite membranes containing different mass ratios of Hec and BBB short fibers were fabricated using a vacuum filtration method, as shown in Figure 1a. BBB short fibers with diameters of 700–800 nm (Figure 1b) and lengths ranging from 50 to 500 μm (Figure 1c) were prepared by the mechanical cutting of long fibers that were prepared by template-assisted electrospinning of the starting monomers followed by solid-state polymerization on fiber templates and pyrolysis.^{39,41} Hec/BBB composite fibrous membranes with a thickness of 72–120 μm (Figure 1d) were produced by a wet-laid process (i.e., filtration of the corresponding suspension of the Hec and short BBB fibers in the specified ratios through an electrospun polymeric filter composed of TPU and the membrane detachment from the filter). The Hec/BBB membranes were porous, with the porosity ranging from 81 to 69% depending on the Hec content (Table S1). The composite membranes were lightweight with densities of 0.36–0.8 g cm⁻³ depending on the Hec and BBB ratios (Table S1).

The scanning electron microscopy (SEM) images of the two sides of the composite membranes are shown in Figure 2a. These images show the inhomogeneous distribution of Hec on the top and bottom of the membranes. Hec was primarily concentrated on the bottom side as a compact layer with all the fibers interconnected and covered by Hec nanosheets. In contrast, the top side exhibited inhomogeneous patches of free fibers and some Hec nanosheets interdispersed and covering several fibers in the network. The gradient in the Hec distribution across the membrane may be related to the significant density difference between the Hec and BBB short fibers (2.8 and 1.62 g cm⁻³, respectively). The high-density Hec settled more at the bottom during the filtration of Hec/BBB dispersion in the wet-laid process. The large aspect ratio Hec sheets laid on the electrospun TPU filter at the beginning of the filtration process make the filtration process slow (a 100 mL suspension needed 30–60 min based on the amount of Hec) and the concentration of Hec more and more at the bottom.

5. Appendix

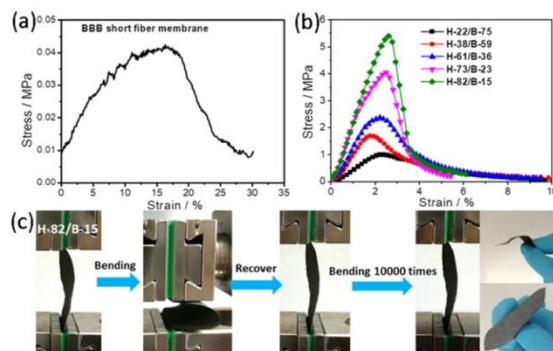


Figure 3. (a) Stress–strain curves of a BBB short fiber membrane and (b) Hec/BBB composite membranes. (c) Bending and recovery processes for the Hec/BBB membrane (H-82/B-15).

Cross-sectional SEM images and Si atom mapping, as obtained by EDXS analysis (Figures 2b and S2), confirm the gradient distribution of Hec.

Tensile testing was carried out to analyze the mechanical properties. The pure BBB membrane that was prepared by random wet-laying of BBB short fibers was very weak as it lacks effective connections between the short fibers (Figure 3a). When Hec was mixed with BBB short fibers to prepare membranes by filtration, the flexible Hec nanosheets connected the BBB fibers in the network, enhancing the mechanical properties. The size of the Hec platelets ($\approx 20 \mu\text{m}$) is larger than the diameter of BBB fiber ($700\text{--}800 \text{ nm}$) to cover many several BBB fibers simultaneously. Membranes with different ratios of BBB and Hec could be prepared. Interestingly, stable flexible membranes with very high Hec content (as high as 82 wt %) were also possible, which showed high modulus ($237 \pm 22 \text{ MPa}$). Both the strength and modulus increased with the Hec content in the composite membranes, as shown in Figure 3b, and the detailed results are listed in Table 1. Interdispersion of

Table 1. Mechanical Properties of the Hec/BBB Composite Membranes

samples	thickness (μm)	strength (MPa)	modulus (MPa)	strain start break (%)
BBB	95	0.04 ± 0.01	0.7 ± 0.2	17 ± 2.1
H-22/B-75	120	0.8 ± 0.1	38 ± 6	3.4 ± 0.6
H-38/B-59	95	1.6 ± 0.1	86 ± 18	2.6 ± 0.2
H-61/B-36	90	2.3 ± 0.1	125 ± 18	2.3 ± 0.1
H-73/B-23	82	3.8 ± 0.3	237 ± 22	2.6 ± 0.3
H-82/B-15	72	5.0 ± 0.5	189 ± 22	3.0 ± 0.2

BBB fibers by Hec nanosheets afforded flexibility to the Hec/BBB composite membranes. The H-82/B-15 sample with the Hec content as high as 82 wt % exhibited no cracks even after bending 10 000 times, as shown in Figure 3c, whereas a pure Hec membrane is brittle with a lot of cracks.

The extremely high thermal stability of the BBB fibers and Hec endowed the same extremely high thermal stability to the Hec/BBB composite membranes. Figure 4a,b shows the TGA curves for the Hec/BBB composite membranes under N_2 and air conditions, respectively. The composite membranes exhibited a

very high $T_{5\%}$ (temperature at which a 5 wt % mass loss occurs). H-22/B-75, which contains the highest amount of BBB, exhibited a $T_{5\%}$ of $590 \text{ }^\circ\text{C}$, which increased to $724 \text{ }^\circ\text{C}$ as the Hec content increased. The better thermal stability is also reflected in the large residual mass (char yield) at $800 \text{ }^\circ\text{C}$ (94–80%), as listed in Table S1. In addition, in air, the composites exhibited high thermal stability. $T_{5\%}$ lies between 518 and $587 \text{ }^\circ\text{C}$ depending on the Hec to BBB fiber ratio. The BBB fibers began oxidizing with a mass loss in air when the temperature was higher than $500 \text{ }^\circ\text{C}$ (Figure 4b).

The pure BBB membrane (thickness of $95 \mu\text{m}$) neither ignited nor produced smoke or flame within 5 min of heating in a high-temperature flame ($800 \text{ }^\circ\text{C}$) (Figure 5a, Supporting Information Video S1). When in contact with a flame for a longer period of time, pyrolysis of the BBB polymer at the point of contact occurred, resulting in a hole in the membrane. This result was observed by burning a cotton ball with flames held on top of a BBB porous membrane after 5 min of heating (Figure 5a). In contrast, the Hec/BBB composite membranes (Figure 5b,c) could sustain contact with a flame without the appearance of a hole even when using a high-temperature Campingaz burner (highest temperature was $1400 \text{ }^\circ\text{C}$). The effective blocking of the flame protected the cotton ball above the flame from burning even after a long period of heating (a minimum of 30 min). The BBB fibers in the composite membrane decomposed, but the thermally stable, nonflammable Hec layer prevented the hole formation, which shielded the cotton ball from the direct flame (Figures 5b,c and S3, Video S2).

In the same way, a wooden block protected by the Hec/BBB composite membrane did not catch fire but started smoking on prolonged exposure to fire for 150 s (Figure S4, Video S3). Without the membrane, the wooden block would burn with the flame within a few seconds. The heat transfer to the other side of the membrane led to smoking of the wooden piece (Figure S4b), but no ignition was triggered. The temperature of the membrane on the opposite side of the flame was measured throughout the experiment by an infrared (IR) camera, as shown in Figure 6a. The highest temperature was detected at approximately $520 \text{ }^\circ\text{C}$. The thermal conductivities of the studied Hec/BBB membranes were $28\text{--}51 \text{ mW m}^{-1} \text{ K}^{-1}$ depending on the Hec content, as shown in Figure 6b.

5. Appendix

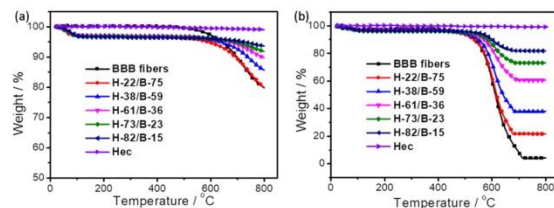


Figure 4. TGA curves of Hec/BBB membranes in N₂ (a) and air atmosphere (b).

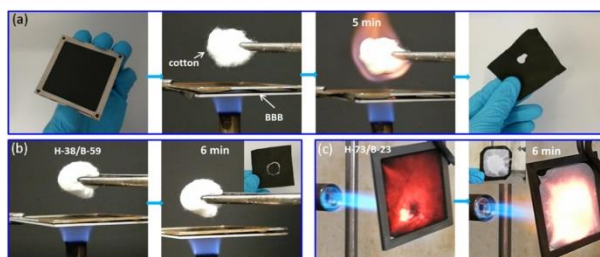


Figure 5. (a) Pure BBB fiber membrane fixed on a steel frame to shield the flame. (b) Cotton ball protected with the Hec/BBB composite membranes. Inset shows photos of the Hec/BBB membrane after the test. (c) Photos of Hec/BBB membrane (H-73/B-23) placed on the flame of a Campingaz burner (1400 °C).

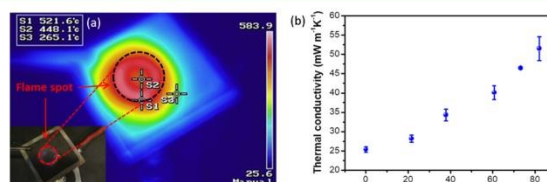


Figure 6. (a) Temperature detected by IR camera for the H-73/B-23 sample placed on flame for 9 min. Inset shows a photo of the sample upon the flame. (b) Changes in the thermal conductivity of the Hec/BBB membranes as a function of the Hec content.

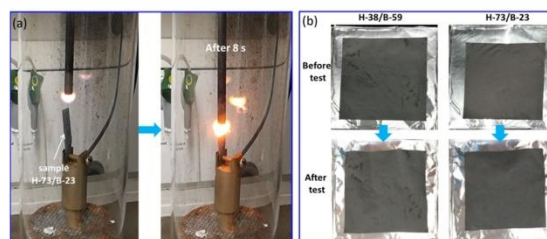


Figure 7. (a) Ignition process for the Hec/BBB (H-73/B-23) membranes in a 100% O₂ atmosphere. (b) Photos of the Hec/BBB membranes before and after the cone calorimeter test.

A condensed phase mechanism could be responsible for the effective protection of Hec/BBB membranes.⁵ The parallel-arranged Hec nanosheets in the composite membranes form a compact layer, which effectively hindered most of the volatiles

produced by pyrolysis from passing through the membrane, whereas heat is dissipated in-plane, and transfer across the membrane to the overlaying materials is retarded. With the dried nanocomposite films, a basal spacing of 0.94 nm was observed by

5. Appendix

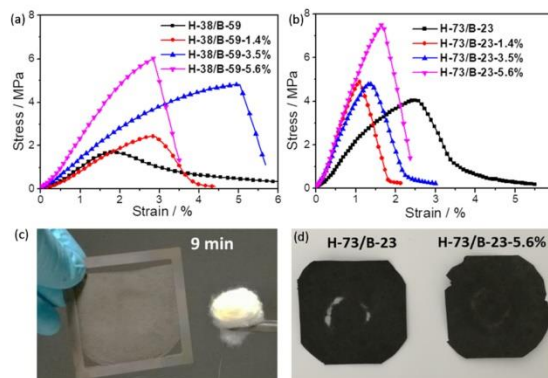


Figure 8. Stress–strain curves of the glued Hec/BBB membrane from (a) H-38/B-59 and (b) H-73/B-23. (c) Glued Hec/BBB membrane (H-73/B-23-5.6%) as a fire shield to protect a cotton ball after testing for 9 min. (d) Comparison of the original and glued samples after burning test for 9 min.

XRD (Figure S5), which corresponds well with the basal spacing of collapsed, nonhydrated Na Hec.⁴⁸ As the thickness of the silicate layer itself amounts to 0.96 nm, this observation implies that the layers are stacked into continuous films with no gap between the adjacent silicate layers.

In addition, no sustained combustion of the Hec/BBB membranes was observed even when the membranes were ignited in a 100% O₂ atmosphere (Figure 7a, Video S4). No combustion or change in the samples before or after the cone calorimeter test was observed, reflecting the excellent flame-retardant properties (Figure 7b, Video S5).

The current preparation procedure for the Hec/BBB composite membranes allows for additional property modifications in a simple fashion. For example, the strength and flame stability were further improved by making the composite membranes compact by self-gluing of the BBB fibers with a BBB polymer. The BBB/composite membranes were soaked in the precursor monomer solution (DAB + NTCA) followed by heat treatment for solid-state polymerization on the composite membranes to afford glued junctions between the crossing BBB fibers (Figures S6 and S7). The glued samples are referred to as H-*x*/B-*y*-*z*, where *z* is the concentration of the respective monomers in the solution. Enhanced tensile strength (as high as 8 MPa) (Figure 8a,b) and prolonged BBB pyrolysis time (Figure 8c,d, Video S6) were obtained, providing a superior shielding effect. The temperature distribution of the membrane upon exposure to the flame was nearly the same as that of the original specimen, as shown in Figure S8, indicating the similar thermal conductivity properties of the glued samples.

CONCLUSIONS

The high-performance BBB polymer and large aspect ratio sodium Hec were processed to prepare nonflammable hierarchically structured composite membranes via an upscalable vacuum-assisted filtration self-assembly process. The membranes can be easily prepared in any shape or size. The otherwise insoluble and nonprocessable BBB was self-assembled into porous membranes by percolation of the corresponding short fibers from an aqueous dispersion, ensuring the production of composite membranes with low density and mechanical

flexibility. The membranes are nonflammable and do not sustain flame or burn with smoke. In addition, these membranes do not exhibit melt dripping and have a low density and very high thermal stability, flexibility, and strength. Such membranes are highly promising for use as lightweight construction materials and protective clothing.

ASSOCIATED CONTENT

Supporting Information

The Supporting Information is available free of charge on the ACS Publications website at DOI: 10.1021/acsami.8b22154.

Chemical reaction for the formation of BBB; SEM image and pore distribution of electrospinning TPU filter; detail values of the thermal properties, density, and porosity of the resulting membranes; additional photos of membranes as the flame shielder; illustration of self-reinforcement of composites; and the SEM images of membranes after reinforcement (PDF)

Direct flammability test of BBB membrane (MPG)

Direct flammability test of Hec/BBB composite membrane (MPG)

Shielding test of Hec/BBB membrane (MPG)

Ignition test of Hec/BBB membrane (MPG)

Cone calorimeter test of Hec/BBB membrane (MPG)

Direct flammability test of glued Hec/BBB composite membrane (MPG)

AUTHOR INFORMATION

Corresponding Author

*E-mail: agarwal@uni-bayreuth.de.

ORCID

Josef Breu: 0000-0002-2547-3950

Seema Agarwal: 0000-0002-3174-3152

Author Contributions

The manuscript was written through contribution of all authors. The experiments were carried out by J.Z. The concept was designed by A.G., and S.A., and elaborated by all co-authors. All authors have given approval to the final version of the manuscript.

Notes

The authors declare no competing financial interest.

ACKNOWLEDGMENTS

The authors wish to thank Florian Puchtler for preparing the synthetic Hec and helping with cone calorimetric measurements. The work was supported by the German Science Foundation (DFG) within the collaborative research center SFB 840.

REFERENCES

- Hilado, C. J. *Flammability Handbook for Plastics*; CRC Press, 1998.
- Andrady, A. L. *Plastics and the Environment*; John Wiley & Sons, 2003.
- Chen, H.-B.; Schiraldi, D. A. Flammability of Polymer/Clay Aerogel Composites: An Overview. *Polym. Rev.* **2018**, *58*, 1–24.
- Lu, S.-Y.; Hamerton, I. Recent Developments in the Chemistry of Halogen-Free Flame Retardant Polymers. *Prog. Polym. Sci.* **2002**, *27*, 1661–1712.
- Wang, X.; Kalali, E. N.; Wan, J.-T.; Wang, D.-Y. Carbon-Family Materials for Flame Retardant Polymeric Materials. *Prog. Polym. Sci.* **2017**, *69*, 22–46.
- Kumar, R.; Tyagi, R.; Parmar, V. S.; Samuelson, L. A.; Kumar, J.; Schoemann, A.; Westmoreland, P. R.; Watterson, A. C. Biocatalytic Synthesis of Highly Flame Retardant Inorganic-Organic Hybrid Polymers. *Adv. Mater.* **2004**, *16*, 1515–1520.
- Ranganathan, T.; Zilberman, J.; Farris, R. J.; Coughlin, E. B.; Emrick, T. Synthesis and Characterization of Halogen-Free Antiflamable Polyphosphonates Containing 4, 4'-Bishydroxydeoxybenzoin. *Macromolecules* **2006**, *39*, 5974–5975.
- Wagner, J.; Deglmann, P.; Fuchs, S.; Ciesielski, M.; Fleckenstein, C. A.; Döring, M. A Flame Retardant Synergism of Organic Disulfides and Phosphorus Compounds. *Polym. Degrad. Stab.* **2016**, *129*, 63–76.
- Perret, B.; Schartel, B.; Stöb, K.; Ciesielski, M.; Diederichs, J.; Döring, M.; Krämer, J.; Altstädt, V. A New Halogen-Free Flame Retardant Based on 9, 10-Dihydro-9-oxa-10-phosphaphenanthrene-10-oxide for Epoxy Resins and their Carbon Fiber Composites for the Automotive and Aviation Industries. *Macromol. Mater. Eng.* **2011**, *296*, 14–30.
- Bourbigot, S.; Duquesne, S. Fire Retardant Polymers: Recent Developments and Opportunities. *J. Mater. Chem.* **2007**, *17*, 2283–2300.
- Peeterbroeck, S.; Laoutid, F.; Taulemesse, J.-M.; Monteverde, F.; Lopez-Cuesta, J.-M.; Nagy, J. B.; Alexandre, M.; Dubois, P. Mechanical Properties and Flame-Retardant Behavior of Ethylene Vinyl Acetate/High-Density Polyethylene Coated Carbon Nanotube Nanocomposites. *Adv. Funct. Mater.* **2007**, *17*, 2787–2791.
- Zanetti, M.; Camino, G.; Canavese, D.; Morgan, A. B.; Lamelas, F. J.; Wilkie, C. A. Fire Retardant Halogen-Antimony-Clay Synergism in Polypropylene Layered Silicate Nanocomposites. *Chem. Mater.* **2002**, *14*, 189–193.
- Kim, H.; Kim, D. W.; Vasagar, V.; Ha, H.; Nazarenko, S.; Ellison, C. J. Polydopamine-Graphene Oxide Flame Retardant Nanocoatings Applied via an Aqueous Liquid Crystalline Scaffold. *Adv. Funct. Mater.* **2018**, *28*, 1803172.
- Smith, R. J.; Holder, K. M.; Ruiz, S.; Hahn, W.; Song, Y.; Lvov, Y. M.; Grunlan, J. C. Environmentally Benign Halloysite Nanotube Multilayer Assembly Significantly Reduces Polyurethane Flammability. *Adv. Funct. Mater.* **2018**, *28*, 1703289.
- Stieger, G.; Scheringer, M.; Ng, C. A.; Hungerbühler, K. Assessing the Persistence, Bioaccumulation Potential and Toxicity of Brominated Flame Retardants: Data Availability and Quality for 36 Alternative Brominated Flame Retardants. *Chemosphere* **2014**, *116*, 118–123.
- de Wit, C. A. An Overview of Brominated Flame Retardants in the Environment. *Chemosphere* **2002**, *46*, 583–624.
- Pittinger, C. A.; Pecquet, A. M. Review of Historical Aquatic Toxicity and Bioconcentration Data for the Brominated Flame Retardant Tetrabromobisphenol A (TBBPA): Effects to Fish, Invertebrates, Algae, and Microbial Communities. *Environ. Sci. Pollut. Res. Int.* **2018**, *25*, 14361–14372.
- Hermanson, M. H.; Isaksson, E.; Forsström, S.; Teixeira, C.; Muir, D. C. G.; Pohjola, V. A.; van de Wal, R. S. V. Deposition History of Brominated Flame Retardant Compounds in an Ice Core from Holtedahlfonna, Svalbard, Norway. *Environ. Sci. Technol.* **2010**, *44*, 7405–7410.
- Kiliaris, P.; Papaspyrides, C. D. Polymer/Layered Silicate (Clay) Nanocomposites: An Overview of Flame Retardancy. *Prog. Polym. Sci.* **2010**, *35*, 902–958.
- Schütz, M. R.; Kalo, H.; Lunkenbein, T.; Gröschel, A. H.; Müller, A. H. E.; Wilkie, C. A.; Breu, J.; Shear Stiff. Surface Modified, Mica-like Nanoplatelets: a Novel Filler for Polymer Nanocomposites. *J. Mater. Chem.* **2011**, *21*, 12110–12116.
- Hausner, J.; Fischer, B.; Stöter, M.; Edenharter, A.; Schmid, J.; Kunz, R.; Rosenfeldt, S.; Altstädt, V.; Breu, J. Increasing Time of Ignition for PS-Clay Nanocomposites Filled with [Fe(bpy)₃]²⁺-Modified Hectorite. *Polym. Degrad. Stab.* **2016**, *128*, 141–148.
- Holder, K. M.; Smith, R. J.; Grunlan, J. C. A Review of Flame Retardant Nanocoatings Prepared Using Layer-by-Layer Assembly of Polyelectrolytes. *J. Mater. Sci.* **2017**, *52*, 12923–12959.
- Gilman, J.; Kashiwagi, T.; Lichtenhan, J. Nanocomposites: A Revolutionary New Flame Retardant Approach. *SAMPE J.* **1997**, *33*, 40–46.
- Gilman, J. Flammability And Thermal Stability Studies of Polymer Layered-Silicate (Clay) Nanocomposites. *Appl. Clay Sci.* **1999**, *15*, 31–49.
- Wang, J.; Du, J.; Zhu, J.; Wilkie, C. A. An XPS Study of the Thermal Degradation and Flame Retardant Mechanism of Polystyrene-Clay Nanocomposites. *Polym. Degrad. Stab.* **2002**, *77*, 249–252.
- Schartel, B.; Bartholmai, M.; Knoll, U. Some Comments on the Main Fire Retardancy Mechanisms in Polymer Nanocomposites. *Polym. Adv. Technol.* **2006**, *17*, 772–777.
- Yu, Z.-L.; Yang, N.; Apostolopoulou-Kalkavrou, V.; Qin, B.; Ma, Z.-Y.; Xing, W.-Y.; Qiao, C.; Bergström, L.; Antonietti, M.; Yu, S.-H. Fire-Retardant and Thermally Insulating Phenolic-Silica Aerogels. *Angew. Chem., Int. Ed.* **2018**, *57*, 4538–4542.
- Fan, H.; Yang, R. Flame-Retardant Polyimide Cross-Linked with Polyhedral Oligomeric Octa (Aminophenyl) Silsesquioxane. *Ind. Eng. Chem. Res.* **2013**, *52*, 2493–2500.
- García, J. M.; García, F. C.; Serna, F.; de la Peña, J. L. High-Performance Aromatic Polyamides. *Prog. Polym. Sci.* **2010**, *35*, 623–686.
- Seel, D.; Benicewicz, B.; Xiao, L.; Schmidt, T. High-Temperature Polybenzimidazole-Based Membranes. *Handbook of Fuel Cells-Fundamentals, Technology and Applications*; John Wiley & Sons: New York, 2009; Vol. 5, pp 300–312.
- Zuo, L.; Fan, W.; Zhang, Y.; Zhang, L.; Gao, W.; Huang, Y.; Liu, T. Graphene/Montmorillonite Hybrid Synergistically Reinforced Polyimide Composite Aerogels with Enhanced Flame-Retardant Performance. *Compos. Sci. Technol.* **2017**, *139*, 57–63.
- Bourbigot, S.; Flambard, X.; Poutch, F. Study of the Thermal Degradation of High Performance Fibres-Application to Polybenzazole and P-aramid Fibres. *Polym. Degrad. Stab.* **2001**, *74*, 283–290.
- Flambard, X.; Bourbigot, S.; Duquesne, S.; Poutch, F. *ACS Symp. Series No. 797, "Fire and Polymer"*; American Chemical Society, 2001; Chapter 6, pp 63–75.
- Bourbigot, S.; Flambard, X. Heat Resistance and Flammability of High Performance fibers: A Review. *Fire Mater.* **2002**, *26*, 155–168.
- Powers, E.; Serad, G. History and Development of Polybenzimidazoles. *High Performance Polymers: Their Origin and Development*; Springer, 1986; pp 355–373.
- Lammers, M.; Klop, E. A.; Northolt, M. G.; Sikkema, D. J. Mechanical Properties and Structural Transitions in the New Rigid-Rod Polymer Fibre PIPD (M5') during the manufacturing process. *Polymer* **1998**, *39*, 5999–6005.

5. Appendix

- (37) Gibbs, W. E. Some Recent Results on the Synthesis of Certain Aromatic Heterocyclic Polymers. *J. Macromol. Sci., Chem.* **1968**, *2*, 1291–1302.
- (38) Munz, A. W.; Schmeisser, D.; Goepel, W. Structural Precursors and Electronic Structure of the Ladder Type Polymer Poly (bis (benzimidazo) benzophenanthroline) (BBB): A Combined UPS/XPS and STM study. *Chem. Mater.* **1994**, *6*, 2288–2302.
- (39) Zhu, J.; Ding, Y.; Agarwal, S.; Greiner, A.; Zhang, H.; Hou, H. Nanofibre Preparation of Non-Processable Polymers by Solid-State Polymerization of Molecularly Self-Assembled Monomers. *Nanoscale* **2017**, *9*, 18169–18174.
- (40) Zhu, J.; Ding, Y.; Liao, X.; Xu, W.; Zhang, H.; Hou, H. Highly Flexible Electrospun Carbon/Graphite Nanofibers from a Non-Processable Heterocyclic Rigid-Rod Polymer of Polybisbenzimidazo-benzophenanthroline-dione (BBB). *J. Mater. Sci.* **2018**, *53*, 9002–9012.
- (41) Zhu, J.; Jiang, S.; Hou, H.; Agarwal, S.; Greiner, A. Low Density, Thermally Stable, and Intrinsic Flame Retardant Poly (bis (benzimidazo) Benzophenanthroline-dione) Sponge. *Macromol. Mater. Eng.* **2018**, *303*, 1700615.
- (42) Greiner, A.; Wendorff, J. H. Electrospinning: A Fascinating Method for the Preparation of Ultrathin Fibers. *Angew. Chem., Int. Ed.* **2007**, *46*, 5670–5703.
- (43) Agarwal, S.; Greiner, A.; Wendorff, J. H. Functional Materials by Electrospinning of Polymers. *Prog. Polym. Sci.* **2013**, *38*, 963–991.
- (44) Ding, Y.; Hou, H.; Zhao, Y.; Zhu, Z.; Fong, H. Electrospun Polyimide Nanofibers and their Applications. *Prog. Polym. Sci.* **2016**, *61*, 67–103.
- (45) Kalo, H.; Möller, M. W.; Ziadeh, M.; Dolejš, D.; Brey, J. Large Scale Melt Synthesis in an Open Crucible of Na-Fluorohectorite with Superb Charge Homogeneity and Particle Size. *Appl. Clay Sci.* **2010**, *48*, 39–45.
- (46) Langner, M.; Greiner, A. Wet-Laid Meets Electrospinning: Nonwovens for Filtration Applications from Short Electrospun Polymer Nanofiber Dispersions. *Macromol. Rapid Commun.* **2016**, *37*, 351–355.
- (47) Reich, S.; Burgard, M.; Langner, M.; Jiang, S.; Wang, X.; Agarwal, S.; Ding, B.; Yu, J.; Greiner, A. Polymer Nanofiber Composite Nonwovens With Metal-Like Electrical Conductivity. *npj Flex. Electron* **2018**, *2*, 5–10.
- (48) Kalo, H.; Milius, W.; Brey, J. Single Crystal Structure Refinement of One- and Two-Layer Hydrates of Sodium Fluorohectorite. *RSC Adv.* **2012**, *2*, 8452–8459.

Supporting Information

Gradient-structured nonflammable flexible polymer membranes

*Jian Zhu, Josef Breu, Haoqing Hou, and Andreas Greiner, Seema Agarwal**

5. Appendix

The membrane porosity was calculated using equation 1:

$$Porosity(\%) = \left(1 - \frac{\rho_{membrane}}{\rho_{clay} \phi_{clay} + \rho_{BBB} \phi_{BBB}}\right) * 100 \quad (1)$$

where $\rho_{membrane}$, ρ_{Hec} and ρ_{BBB} are the density of composite membrane, Hec (2.7 g cm^{-3}) and BBB (1.62 g cm^{-3}), respectively, and ϕ_{Hec} and ϕ_{BBB} are the weight ratio of the Hec and BBB fibers, respectively. The densities of the Hec/BBB membranes were calculated from the weight and volume. The densities of the final membranes were in the $0.36 \sim 0.8 \text{ g cm}^{-3}$ range, and the corresponding porosity were approximately 69% to 81%, as listed in **Table S1**.

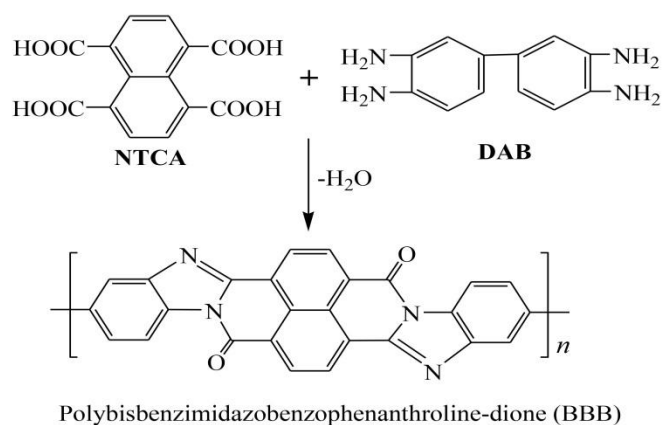
Table S1. Thermal properties, composition, density and porosity of the Hec/BBB membranes.

Samples	Thermal properties			Composition			Density (g/cm ³)	Porosity (%)
	T _{5%} in N ₂ (°C)	Wight loss at 800 °C in N ₂ (%) ^a	T _{5%} in air (°C)	Hec (%)	BBB fibers (%)	Water (%)		
H-22/B-75	590	20 (18)	518	22	75	3	0.36	80.9
H-38/B-59	637	14 (14.8)	534	38	59	3	0.4	80.9
H-61/B-36	668	10 (10.2)	554	61	36	3	0.48	79.9
H-73/B-23	691	8 (8.6)	569	73	23	4	0.55	78.4
H-82/B-15	724	6 (6)	587	82	15	3	0.8	69.5

^a The theoretical values of the weight loss at 800 °C in N₂ are listed in brackets. The

theoretical values are calculated on the basis of the composite composition as determined from TGA in air and the weight loss of pure BBB and clay in nitrogen.

5. Appendix



Scheme S1. Chemical reaction for the formation of BBB.

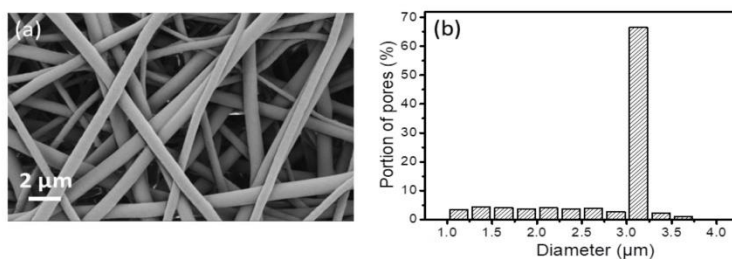


Figure S1. SEM image of electrospun TPU membrane (a) and pore size distribution of TPU fiber membrane (b).

5. Appendix

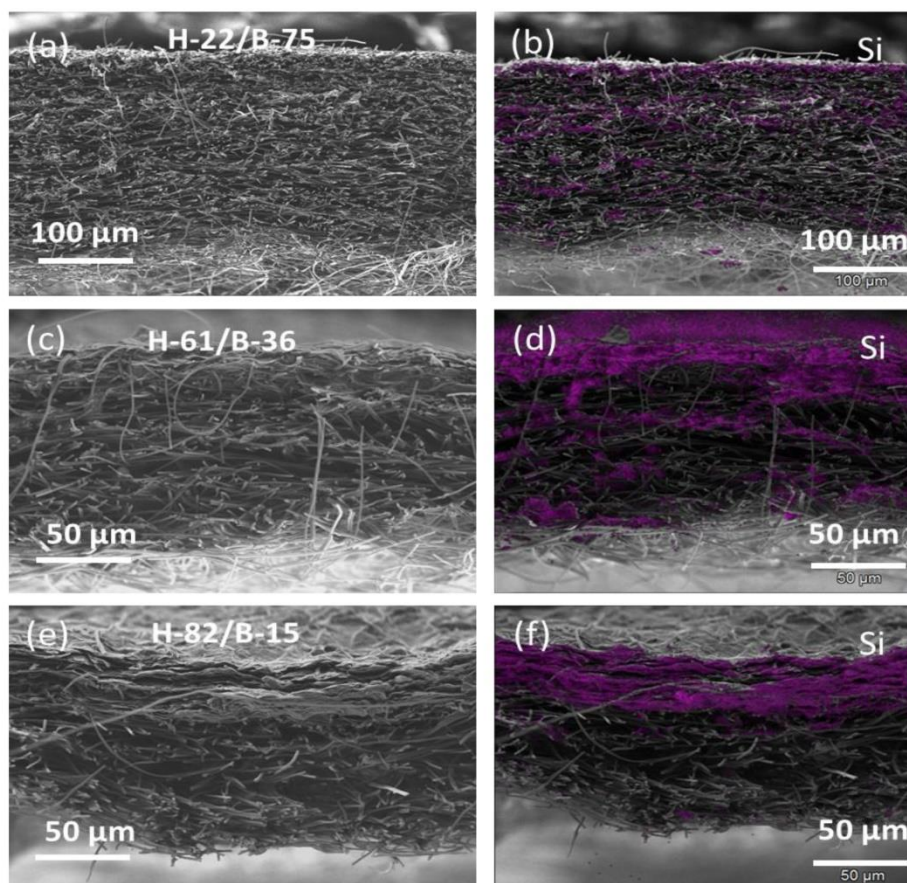


Figure S2. SEM images and Si atom mapping as obtained by EDX for a cross section of H-22/B-75 (a, b), H-61/B-36 (c, d) and H-82/B-15 (e, f).

5. Appendix

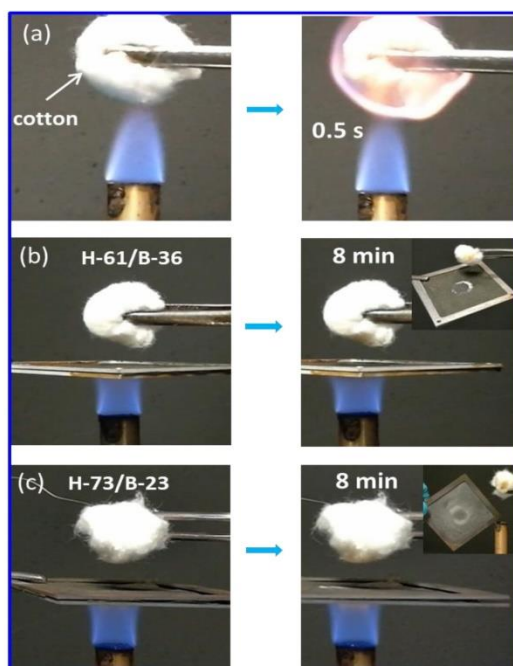


Figure S3. Photos of cotton ball exposed to flame (a) and the cotton ball protected by the Hec/BBB composite membranes (b, c).

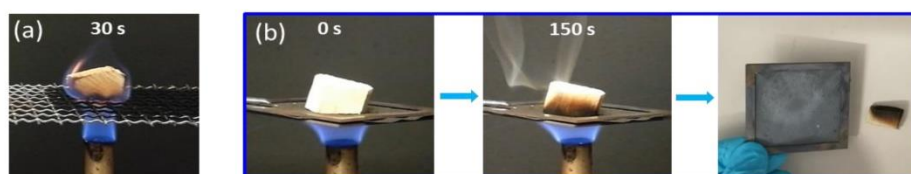


Figure S4. (a) Photo of burning wood with flame when placed directly in contact with the flame. (b) Photos of Hec/BBB (H-73/B-23) acting as a shield to protect the wood piece and nonflammability of the composite membrane.

5. Appendix

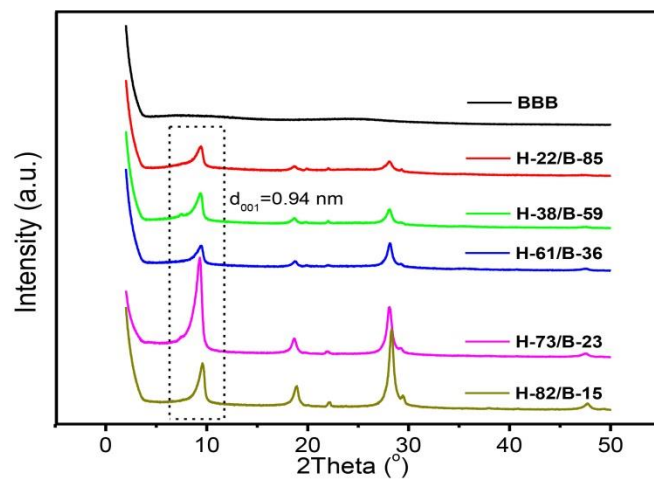


Figure S5. XRD patterns of BBB fibers and Hec/BBB composite membranes.

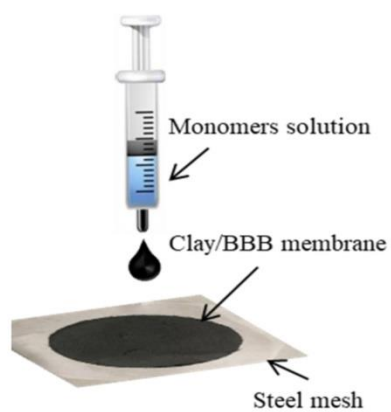


Figure S6. Illustration of coating the monomer solution on the surface of the Hec/BBB membrane. The concentrations of the monomer solutions were 1.4 wt.%, 3.5 wt.% and 5.6 wt.%, respectively.

5. Appendix

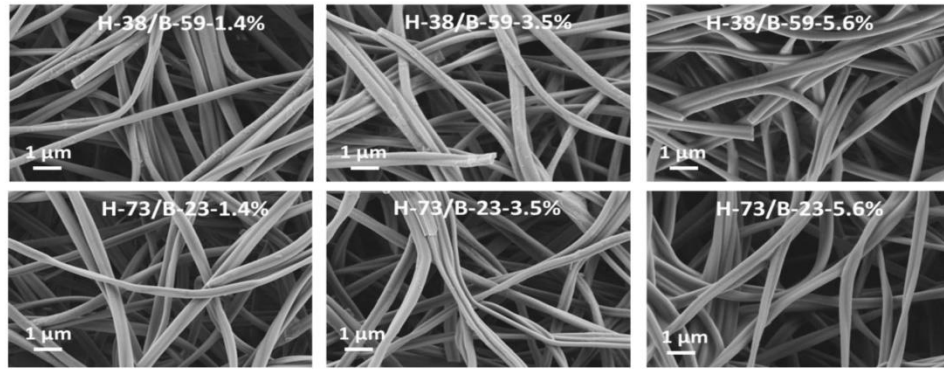


Figure S7. SEM images of glued Hec/BBB composite membranes.

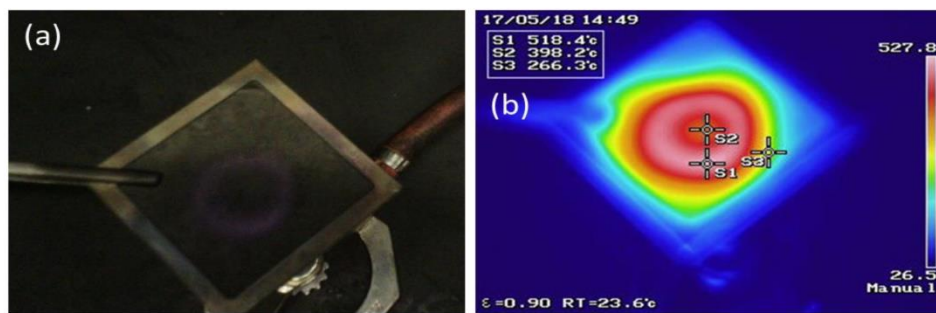


Figure S8. (a) Photo of glued Hec/BBB (H-73/B23-5.6%) membrane after coming into contact with high temperature flame. (b) IR camera image of the glued H-73/B-23-5.6% specimen on the opposite side of the flame for 9 mins.

5. Appendix

5.4 Filter-Through Method of Making Highly Efficient Polymer-Clay Nanocomposite Membranes

Jian Zhu, Christoph Habel, Theresa Schilling, Andreas Greiner, Josef Breu, Seema Agarwal. Filter-Through Method of Making Highly Efficient Polymer-Clay Nanocomposite Membranes, *Macromolecular Materials and Engineering*, **2019**, 1800779.



Filter-Through Method of Making Highly Efficient Polymer-Clay Nanocomposite Membranes

Jian Zhu, Christoph Habel, Theresa Schilling, Andreas Greiner,* Josef Brey,* and Seema Agarwal*

Electrospun filter with hierarchical pore structure and variable pore diameter is used for the first time in making a flexible, strong, and high gas-barrier membrane. A versatile, technical, benign processing method for the fabrication of highly filled (>25 wt%) efficient gas-barrier polymer membrane with perfectly aligned synthetic high-aspect ratio layered silicate (clay) of variable and considerable thickness (up to 5 μm) is presented. This process combines advantageous features of an electrospun substrate like high porosity, variable pore size (typically <5 μm), thermoplasticity and of an aqueous suspension of a synthetic clay consisting of single 1 nm thick layers with a huge median lateral extension (>10 μm) in a layered structure. By simple and fast filtration, a gas-barrier self-assembled layer of variable and appropriate thickness is obtained on a mechanically stable thermoplastic electrospun filter support that subsequently can be laminated adhesively or via hot pressing, even in a multilayer structure, if required. The resulting composite membranes are flexible, strong, transparent, and show enhanced gas-barrier properties.

1. Introduction

Electrospun porous thermoplastic membranes have been extensively studied and used as air (high efficiency particulate air [HEPA], ultra-low particulate air [ULPA]) and for bacterial filtration.^[1–3] The hierarchical porous structure with small and variable pore size and high specific surface area provides efficient filtration. The focus of such studies was purification of air and water by removing particulate living and nonliving impurities. To the best of our knowledge, we show a novel aspect of particulate filtration through electrospun thermoplastic porous

membranes for the first time in making flexible, strong polymer membranes with enhanced gas-barrier properties. The novelty is based on the high-aspect ratio delaminated melt synthesized layered silicate (clay)^[4] that is self-assembled in a polymer matrix as a barrier-layer between two electrospun membranes by filtration (filter-through method) and subsequently hot-pressed^[5] which leads to enhanced gas-barrier properties.

Nanosheets of layered materials like clay (e.g., Na-hectorite [Hec]),^[6–9] or graphene oxide (GO)^[10,11] are the most promising fillers for the fabrication of polymer nanocomposite barrier coatings.^[12–16] Barrier is of prime importance in applications spanning from automotive, furniture, construction, food, or optoelectronic packaging.^[13,14,17–19] According to Cussler, the barrier improvement factor is nonlinearly

dependent on both aspect ratio and filler content. Consequently, it is most efficient and material-saving to apply fillers with the highest aspect ratio accessible and at the maximum filler level that can be processed.^[20] Melt synthesized hectorites come in diameters of up to 20 μm and moreover can be utterly delaminated into 1 nm thick nanosheets by repulsive osmotic swelling simply by immersing them into water.^[4,21–23] The suspensions obtained represent viscous liquid crystalline (nematic) phases because the huge aspect ratio blocks isotropic rotation.^[24–26] The nematic phases can, however, easily be mixed with water-soluble polymers without triggering any reaggregation. As a consequence of the nematic character only dilute polymer/clay suspensions can be applied for coatings. The final filler content of the dried coating is determined by the polymer/clay ratio. Removal of large amounts (>95 vol%) of the dispersion medium (here water), represents a serious challenge. In particular, if the coating is applied on an impermeable substrate, typically a polyethylene terephthalate (PET) foil, evaporation can only occur at the suspension/air interface while concomitantly both filler and polymer are increasingly concentrated. Consequently, a steadily improving barrier to further evaporation is building up with time.

These drying obstacles limit the coating thickness that can be obtained in one coating step to less than 2 μm and the drying moreover has to be conducted very carefully at moderate temperatures (<80 °C) and slowly (typically >48 h). Otherwise suspension medium is getting trapped in the barrier coating

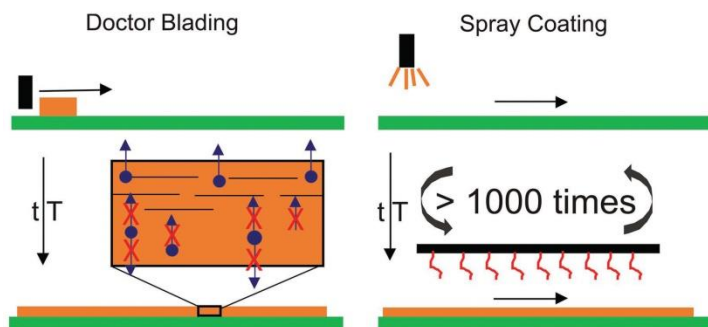
J. Zhu, Prof. A. Greiner, Prof. S. Agarwal
Macromolecular Chemistry II
Bavarian Polymer Institute and Bayreuth Center for
Colloids and Interfaces
University of Bayreuth
Universitätsstraße 30, Bayreuth 95447, Germany
E-mail: greiner@uni-bayreuth.de; agarwal@uni-bayreuth.de

C. Habel, T. Schilling, Prof. J. Brey
Bavarian Polymer Institute and Department of Inorganic Chemistry
University of Bayreuth
Universitätsstraße 30, Bayreuth 95447, Germany
E-mail: Josef.Brey@uni-bayreuth.de

 The ORCID identification number(s) for the author(s) of this article can be found under <https://doi.org/10.1002/mame.201800779>.

DOI: 10.1002/mame.201800779

5. Appendix



Scheme 1. Disadvantages of the two main state-of-the-art solution based processing techniques. Doctor blading suffers of the self-sealing effect that potentially traps suspension medium if not dried slowly at moderate temperatures. Spray coating of multiple layers can be automated but nevertheless is time consuming for coatings of appreciable thickness.

and will eventually trigger blistering that completely ruins barrier.^[27] Alternatively, coatings can be applied by spraying multiple layers with intermediate drying of individual applications. Both processing methods yield polymer/clay nanocomposite coatings showing (ultra-) high gas barriers.^[13,14,17,18,27]

Moreover, the compatibility between the coating dispersion and the substrate is critical.^[28,29] In particular with doctor blading the wettability often poses a problem that requires a primer or additives.^[16] In summary, both doctor blading and spray coating represent rather time-consuming processing methods (**Scheme 1**) retarding mass production and widespread application in particular in low margin (commodity) applications like food packaging.

Here we present a new simple and upscalable, technical benign processing method to fabricate clay self-assembled coatings via filtration of the clay aqueous dispersion on an electrospun, thermoplastic nonwoven support **Scheme 2**, step (1). Electrospinning is a simple and robust processing technique to produce fibers with adjustable diameters that can be deposited to form porous, nonwoven supports.^[30–32] Fabrication of infinite tracks with areas up to 2000 m² day⁻¹ represents no problem.^[33,34] The porosity of the nonwoven substrate can be

tuned to optimize filtration efficiency. Wetting of the porous support represents no problem. The dispersion medium is removed concomitantly by evaporation at the top and filtration at the bottom reducing the drying time drastically (**Scheme 2**, Step (2)).

While in principle any polymer that can be electrospun may be considered as porous support,^[35] here we chose thermoplastic polyurethane (TPU). TPU shows good chemical resistance, abrasion resistance, high elasticity, and great shock absorption. TPU films and coatings are applied in various fields, like automotive, furniture, and construction.^[36–39] For food packaging, however, the stiffness and strength and the gas permeability properties of TPU have to be improved. This is achieved by applying a polyvinylpyrrolidone (PVP)-Hec barrier sandwich layer between the TPU membranes.

For reasons of simplicity we here laminate with a second electrospun TPU nonwoven (**Scheme 2**, Step (3)). The thermoplastic nature of TPU allows lamination of the porous TPU/PVP-Hec sandwich by hot pressing which concomitantly densifies the TPU (**Scheme 2**, Step (4)).

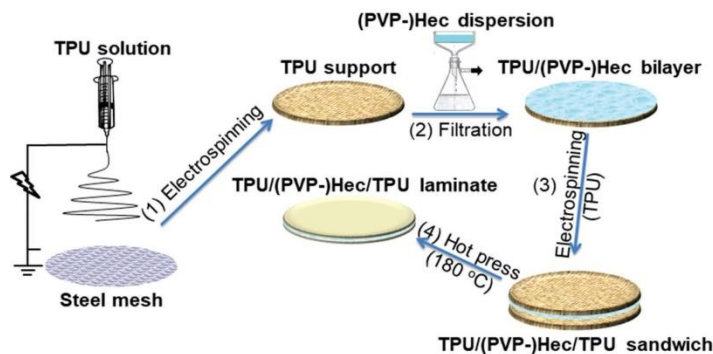
2. Results and Discussion

2.1. Processing Route

Electrospinning of a TPU solution provides fibrous nonwoven supports by random deposition of fibers with an average fiber diameter of 840 nm (**Figure 1a**). The pore diameter is in the range of 0.5–3.5 μm with maximum pore diameters being around 2.4 μm (**Figure 1b**) which is considerably smaller than the typical diameter of Hec nanosheets (≈20 μm) (**Figure S1**, Supporting Information).^[4]

The porosity of the TPU support is ≈66%, which makes TPU electrospun support an excellent candidate for coating with PVP-Hec nanocomposites via filtration. Because of the huge aspect ratio of Hec nanosheets (20000) upon filtration through the pores of the nonwoven TPU support they self-assemble perfectly aligned (textured) to the surface of the support. The sample after filtration is designated as bilayer TPU/PVP-Hec. The PVP fills the gaps between the individual Hec nanosheets. The large absolute diameter of the Hec nanosheets is prerequisite to this coating process. Natural montmorillonite^[40] (diameter <0.3 μm) passes almost completely through the filter and no homogenous continuous layer is built (**Figure S2**, Supporting Information).

Contrary to montmorillonite, with large aspect ratio Hec a homogeneous



Scheme 2. Fabrication procedure of TPU/PVP-Hec/TPU laminates.

5. Appendix

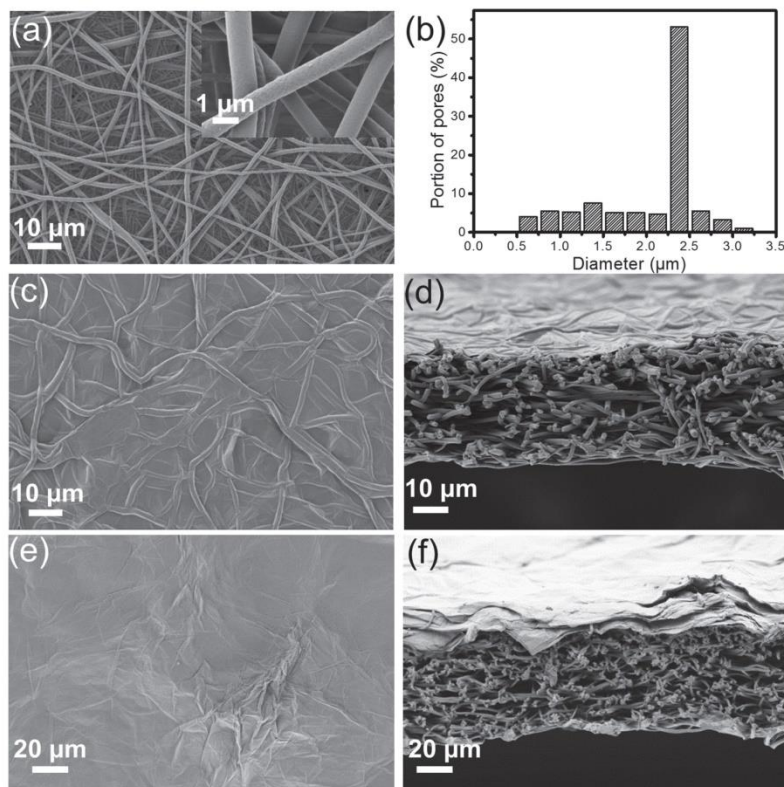


Figure 1. a) Scanning electron microscope (SEM) images and b) pore size distribution of the electrospun TPU support. Dependency of the surface roughness and coating thickness on the Hec content in the filtration suspension (2 mg c,d) and 65 mg e,f) per 100 mL water, respectively.

deposition of the clay nanosheets on the surface of the TPU support is observed (Figure 1c–f). For fabrication of barrier coatings, suspensions having different amounts of PVP-Hec (constant ratio of PVP:Hec/40:60 wt%) were coated on the porous TPU support by filtration. Even low amounts of Hec (as low as 2 mg 100 mL⁻¹ in the filtration dispersion) provide a compact and uniform layer of the Hec nanosheets on the TPU fibrous supports (Figure 1c). The PVP fills the gaps between the individual Hec nanosheets. The surface of the nanocomposite coating becomes smoother with increasing amount of PVP-Hec in the dispersion filtered on the TPU support (Figure S3, Supporting Information).

SEM micrographs of cross sections of the TPU/PVP-Hec bilayer indicate a thickness of the PVP-Hec coatings in the range of around 60 to 5000 nm for the samples prepared by filtration of suspensions with Hec concentrations, 2 to 65 mg 100 mL⁻¹ suspensions, respectively (Figure 1d,f). Clearly, the thickness of the PVP-Hec nanocomposite coating can be adjusted over a wide range by varying the amount of Hec in the suspension deposited on the porous TPU support (Figure S4, Supporting Information). The thickness of the

PVP-Hec layer changes little during the hot press process (Figure 2a,b).

The PVP-Hec nanocomposite coatings supported on TPU non-woven obtained by filtration can subsequently be laminated. For simplicity and as a proof of principle we here laminated with a second nonwoven TPU layer. For this, a second TPU non-woven is casted onto the bilayer via electrospinning. Subsequently the sandwich is laminated by hot pressing at 180 °C for 10 min. This sandwich-like structure could be obtained with almost any other second polymer film. This will allow fabricating barrier membranes meeting mechanical and gas-barrier property requirements in various fields of application. In this proof of principle, the second outer-layer is also TPU. The PVP-Hec nanocomposite coating is opaque due to a certain surface roughness of the highly filled composite resulting in surface scattering. Consequently, after lamination via hot pressing a transparent nanocomposite membrane is obtained (Figure 2c,d). The transmittance was found to be in the range of 60–80% while the thickness of the PVP-Hec coating had a negligible influence on the transmittance (Figure 2e; Table S1, Supporting Information). The dense three-layer laminates obtained

5. Appendix

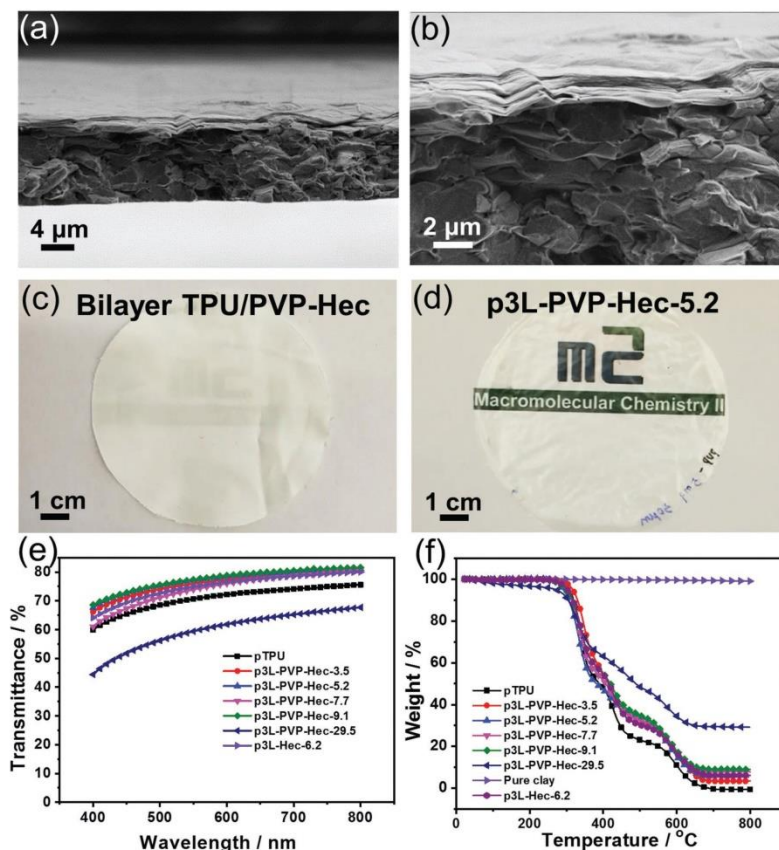


Figure 2. a) and b) show SEM pictures of cross section of bilayer-TPU/PVP-Hec after hot pressing (sample from 20 mg per 100 mL suspension). c) is the photo of TPU/PVP-Hec membrane before hot pressing and d) is the photo of final laminate after hot pressing. e) The transmittances of the final laminate between the wavelengths of 400–800 nm. f) Thermogravimetric analysis (TGA) curves of TPU and composite membrane.

after hot pressing are referred to as p3L-PVP-Hec-X where X gives the Hec content (wt%) in the resulting laminate. The three-layer laminates with Hec content from 3.5 to 29.5 wt% were obtained (Figure 2f; Table S1, Supporting Information).

2.2. Crystallinity of PVP-Hec Coatings

The Hec and PVP-Hec coatings obtained via filtration represent smectic crystals as evidenced by X-ray diffraction (XRD). The neat electrospun TPU support (Scheme 2, after Step (1)) shows an amorphous halo centered at $2\theta = 20^\circ$ (Figure 3a). With pure Hec coatings a sharp diffraction peak was observed at $2\theta_{001} = 7.23^\circ$ (Figure 3a) which corresponds to mono-hydrated sodium cations in the interlayer space with a typical d-spacing of 1.22 nm.^[41] PVP-Hec dispersions filtrated on a nonwoven TPU layer showed a sharp and rational 001-series with the 001 diffraction peak being observed at $2\theta_{001} = 3.96^\circ$. This corresponds to a d-spacing

of 2.26 nm (Figure 3a, Scheme 2 after Step (2)) and indicates that in the nanocomposite coating adjacent Hec nanosheets (0.96 nm) are separated by equivalent volumes (1.3 nm) of PVP.

The rational 001-series with sharp peaks indicates a well ordered smectic crystallinity of the PVP-Hec coatings with translational homogeneity of the nanocomposite. The nearly perfect order of equidistantly arranged Hec nanosheets is furthermore not affected by the final hot pressing step as shown in the transmission electron microscopy (TEM) image of the cross section (Figure 3b).

2.3. Mechanical Properties

Even a pure clay coating sandwiched between two TPU layers (p3L-Hec-6.2) already increased the modulus dramatically without affecting the tensile stress at break significantly as compared to neat hot-pressed TPU support (pTPU) (Table S2,

5. Appendix

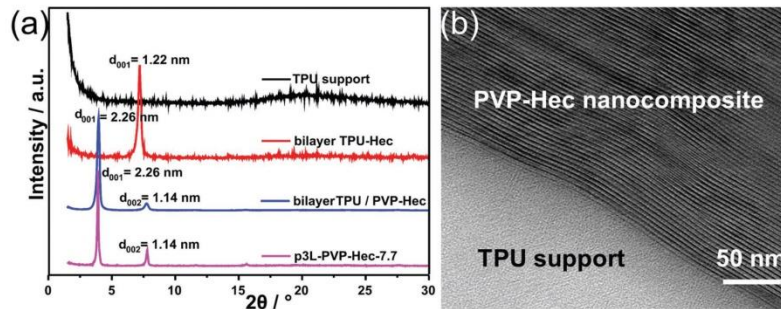


Figure 3. a) XRD patterns of the neat pressed TPU support, Hec coating (bilayer TPU-Hec), and PVP-Hec coating on the TPU support (bilayer TPU / PVP-Hec) and the final hot-pressed laminate after the hot pressing (p3L-PVP-Hec-7.7); b) TEM image of the alignment of the clay nanoplatelets in the interlayer PVP-Hec nanocomposite (p3L-PVP-Hec-9.1).

Supporting Information; **Figure 4a**). Nevertheless, by comparison of pure Hec coatings with PVP-Hec coatings of comparable amount of Hec, it can be seen that the elasticity modulus (E-Modulus) is significantly higher. With increasing Hec content in the laminates, the tensile modulus increases by up to a factor of >60 as compared to the neat TPU (17 MPa). With 29.5 wt% of Hec an E-Modulus of 1117 MPa was observed (p3L-PVP-Hec-29.5, **Figure 4a**). More interestingly, with a polymer matrix separating the adjacent clay nanosheets, the laminates are significantly less brittle than for pure Hec coatings. Without any polymer matrix (p3L-Hec-6.2), there is a huge reduction of the strain at break of about 40% (from 564% to 351%) as compared to the neat TPU matrix (pTPU). For p3L-PVP-Hec-9.1, using PVP-Hec, this is lowered to a 15% reduction.

Furthermore, this modulus is even much higher than other TPU-clay nanocomposites mentioned in literature with comparable clay contents, like TPU/laponite, TPU/dopamine-modified clay, PU/vermiculite, or TPU/organoclay (**Figure 4b**).^[42–45] Moreover, the resulting E-Modulus of samples even outperform low-density polyethylene (LDPE) and rather is found to be in the range of polyamide (PA 6).^[46] With a strain at break of up to 487% (p3L-PVP-Hec-9.1) the sandwich-like nanocomposite laminate combines elastomeric and thermoplastic behavior with much improved moduli while the strength of all

nanocomposite laminates is little affected by the incorporation of the PVP-Hec coating at all filler contents below 10 wt%. The nanocomposite laminate is flexible even with high amount of clay (p3L-PVP-Hec-29.5), as revealed by bending test (**Figure S5**, Supporting Information). The laminate did not develop any cracks even after bending for 10000 times.

2.4. Oxygen and Water Vapor Transmission Rate

In particular for food packaging, the oxygen transmission rate (OTR) is the crucial parameter. As already mentioned, platelet fillers like graphene oxide or layered silicates may be used to improve the barrier properties of polymer matrices against different gases and molecules. According to Cussler the resulting gas barrier of a polymer (permeability nanocomposite: P , neat matrix: permeability P_0 and geometrical factor μ) with layered materials is dependent in a nonlinear manner on the filler content (ϕ , vol% ratio) and the aspect ratio (α) of the filler (Equation (1)).^[47]

$$P_{rel} = \frac{P}{P_0} = \left(1 + \mu \left(\frac{\alpha^2 \phi^2}{1 - \phi} \right) \right)^{-1} \quad (1)$$

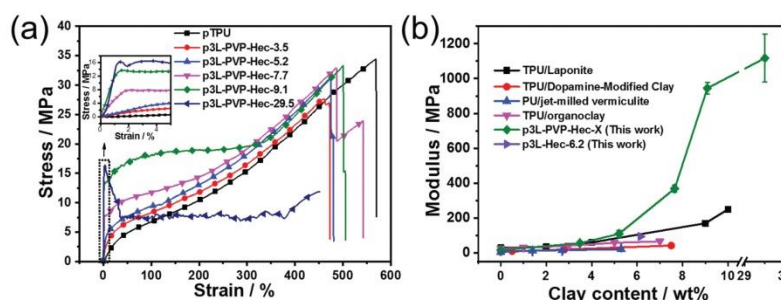


Figure 4. a) Stress–strain curves of the neat hot-pressed TPU (pTPU) compared to the laminates with the nanocomposite interlayer. b) Comparison of the elasticity modulus of the laminates of this work and the TPU nanocomposites of other research groups.

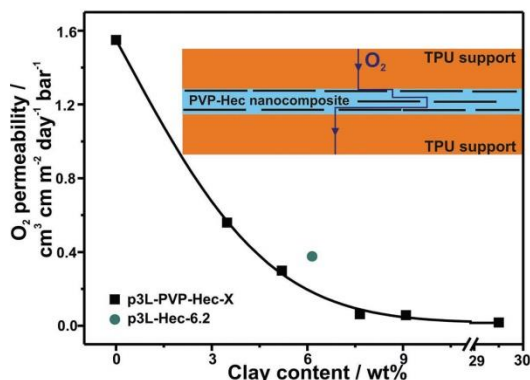


Figure 5. Oxygen permeability of p3L-PVP-Hec-X laminate membranes changes with different amounts of clay (X) at 50% RH. A laminate with a pure clay coating is shown for comparison. The “tortuous pathway” created by incorporation of delaminated Hec nanosheets into a PVP matrix is also illustrated.

The permeability is the measured transmission rate normalized to a certain thickness which allows comparison with other materials of different thicknesses. Herein, the overall laminate thickness (TPU support+ PVP-Hec nanocomposite+ TPU support) is used for this calculation. Caused by the huge aspect ratio of the melt synthesized Hec nanosheets the permeability decreased with incorporation of both, pure Hec coatings and PVP-Hec nanocomposite coatings as interlayer into the laminated membrane (Figure 5). By filling the gaps between the inorganic nanosheets in the filtered interlayer with a polymer matrix, the barrier properties are greatly improved as compared to the pure Hec coating. Moreover, the permeability steadily decreases with increasing amounts of delaminated Hec nanoplatelets in the interlayer nanocomposite (Table S3, Supporting Information; Figure 5). This is due to the elongation of the tortuous path in the interlayer, realized with a homogenous dispersion of the Hec nanoplatelets in the polymer matrix (inset in Figure 5). The increased amount of Hec is realized with the filtration of thicker interlayers, which occurs with filtration of nanocomposite dispersion with an increased overall solid content. A remarkable reduction of the oxygen permeability of 98.8% with a filler content of 29.5 wt% ($0.0185 \text{ cm}^3 \text{ cm m}^{-2} \text{ day}^{-1} \text{ bar}^{-1}$, p3L-PVP-Hec-29.5) for the laminate as compared to the neat TPU matrix ($1.55 \text{ cm}^3 \text{ cm m}^{-2} \text{ day}^{-1} \text{ bar}^{-1}$, pTPU) was observed at 50% RH.

The reduction of the oxygen barrier compared to the neat polymer matrix (up to >80 times) is higher than in other published PU clay nanocomposites and furthermore, the resulting overall permeability rates are much lower (Table S3, Supporting Information).^[48,49] We carried out measurements at 50% RH and even at elevated RH of 75%. Even at 75% RH the permeability of p3L-PVP-Hec-29.5 just slightly increases to $0.024 \text{ cm}^3 \text{ cm m}^{-2} \text{ day}^{-1} \text{ bar}^{-1}$. Moreover, the laminates outperform commercially used packaging materials like polyethylene terephthalate (PET) or low-density polyethylene (LDPE) (Table S2, Supporting Information).^[46,50,51] Furthermore, also the water vapor transmission rate (WVTR) could be reduced

by a factor of >35 to a resulting water vapor permeability of $0.79 \text{ g cm}^{-2} \text{ day}^{-1} \text{ bar}^{-1}$ (50% RH, p3L-PVP-Hec-9.1).

3. Conclusions

The proposed processing method enables fabrication of light weight barrier membranes by a scalable, fast, and simple filtration. Any porous thermoplastic electrospun support can be used. The porosity of the support greatly accelerates fabrication of a barrier coating from a dilute dispersion of delaminated nanosheets mixed with a soluble polymer matrix.

This fast processing technique releases time-constraints encountered by other solution based processing methods of coatings like doctor blading or spray coating. It therefore offers a great potential to deliver highly filled nanocomposite coatings via a mechanically stable support that subsequently may be laminated with a variable third layer. This offers flexibility with respect to the overall performance of the resulting barrier membrane. Hot pressing as used in this work is just one example that may be replaced by any other lamination approach.

The amount of Hec can easily be varied and with increasing Hec content barrier performance (98.8% reduction of oxygen permeability) and tensile moduli (by a factor of >60) of the laminates improve a great deal, while elongation at break is affected little.

4. Experimental Section

Materials: Thermoplastic polyurethane (TPU, Desmopan DP 2590, Bayer Materials Science, M_w : 88 900), polyvinyl pyrrolidone (PVP, M_w : 40 000, Sigma-Aldrich), were used as received. The Na-Hectorite ($[\text{Na}_{0.5}]^{\text{int}} [\text{Mg}_{2.5}\text{Li}_{0.5}]^{\text{oc}} [\text{Si}_4]^{\text{tet}} \text{O}_{10}\text{F}_2$) (Hec) was synthesized via melt synthesis according to an established literature procedure.^[4] The clay platelets show aspect ratios of ≈ 20000 which has been proven by statistic light scattering (SLS) and atomic force microscopy (AFM).^[4] Natural montmorillonite (MMT) was used for comparison (BYK GmbH). *N,N*-Dimethylformamide (DMF, 99.9%), tetrahydrofuran (THF, $\geq 99.9\%$), and *n*-butyl alcohol were purchased from Sigma-Aldrich and used without purification.

Preparation of the TPU/PVP-Hec Composite Membranes: The electrospinning solution was prepared by dissolution of TPU in mixed solvents of DMF and THF (volume ratio 80/20). The concentration of the TPU solution was 16 wt%. A circular 325-mesh stainless steel wire mesh (diameter 6.4 cm, area 43 cm^2) was used as the collector with the distance of 20 cm to the tip of needle for collecting spun fibers. The applied voltage was 16 kV. Electrospun TPU fibrous membrane deposited on the steel mesh obtained from spinning 0.4 mL solution was used as the filter for Hec suspension. Hec suspension was prepared by dispersing 1 g Na-Hectorite (Hec) in 199 mL deionized water and stirring vigorously for 3 days to form a 0.5 wt% suspension. The PVP-Hec dispersion was obtained by adding certain amounts of PVP powder in Hec suspension and stirring for another 12 h. The mass ratio (wt%) of Hec to PVP was controlled to 6:4. The TPU/PVP-Hec/TPU laminates were fabricated by vacuum filtration combined with hot pressing. For example, PVP-Hec dispersion, 100 mL diluted suspension with definite amount of Hec (2, 5, 10, 20, and 65 mg per 100 mL water, PVP:Hec wt% ratio always 4:6) was filtered through an electrospun TPU membrane. The PVP-Hec layer was sandwiched between the TPU fibrous membranes by spinning another 0.4 mL TPU on top of the PVP-Hec layer. At last, the sandwich-like structure was peeled from the mesh and pressed with a load of 15 000 pound at $180 \text{ }^\circ\text{C}$ for 10 min to get transparent p3L-TPU-PVP-Hec-X membranes. X is the amount of Hec in the final composite as determined by TGA. A pure TPU film and a p3L-TPU-Hec film were used for comparison.

Characterization: The pore size distribution of the TPU fibrous membranes was tested with a pore size meter (PSM 165, Topas GmbH). The porosity of the TPU membranes was confirmed by *n*-butyl alcohol absorption method. A TPU membrane with the size of 10 mm × 20 mm was dried completely and weighed. After immersing it in *n*-butyl alcohol for 2 h, the sample was weighed again. The porosity was calculated using the following equation.

$$\text{Porosity} = \frac{W - W_0}{\rho \times V_0} \quad (2)$$

where W_0 , V_0 are the weight and volume of pristine TPU mat and W is the weight after putting in *n*-butyl alcohol, ρ = density *n*-butyl alcohol. Differential scanning calorimetry (DSC) was adopted to measure the thermal transitions of TPU membrane. The morphology of the TPU membrane, PVP-Hec layered on TPU membrane, the cross section of the bilayer-TPU/PVP-Hec membranes, and the diameter of the clay nanosheets were observed by scanning electron microscope (SEM, Zeiss Leo 1530). The macrostructure of the PVP-Hec coated TPU membrane was checked by XRD using nickel filtered Cu K α radiation ($\lambda = 1.54187 \text{ \AA}$) on a Bragg-Brentano-type diffractometer (XPERT-PRO, PANalytical B.V.). The transparency was measured by a UV-vis spectrophotometer (V-630, JASCO). The ordered structure of PVP-Hec layer was observed by transmission electron microscopy (TEM), after preparing the samples via cryo ion-slicing (Cryo Ion Slicer IB-09060CIS (JEOL GmbH, Germany)). The samples for the UV-vis measurement were cut to the size of 1 cm × 4 cm and stuck on a glass plate of the same size. The glass plate without sample was tested as the blank. The precise contents of Hec in the p3L-TPU-PVP-Hec-X membranes were determined via thermogravimetric analysis (TGA, TG 209 F1 Libra) in air at heating rate of 10 °C min⁻¹. Mechanical properties were determined by stress-strain tests on a testing machine (Zwick/Roell, BT1-FR0.5TN. D14). The samples for the tensile measurement were cut to size of 3 mm × 40 mm. The tensile speed applied to the samples was 5 mm min⁻¹ and the pristine effective tensile length is 10 mm. The slope of the linear region of the stress-strain curves was used to determine the elasticity modulus. All the tests for each sample were measured for at least five times and statistically averaged. Flexibility was determined by bending test using Zwick/Roell machine. Oxygen transmission rates (OTRs) of the specimens were determined on a Mocon Ox-Tran 2/21 (Mocon Inc., Minneapolis, USA) at room temperature and 50% and 75% relative humidity (RH). A mixture of 95% N₂ and 5% H₂ (Linde Formigas 95/5) was used as carrier gas and 100% O₂ (Linde Sauerstoff 3.5) as permeant. The effective sample area was controlled to 5 cm² by covering with aluminum masks (type MO025-493, Mocon Inc.). WVTRs were determined on a HiBarSens HBS 2.0 HT (Sempa Systems GmbH, Dresden, Germany). The lower detection limit is 1 × 10⁻⁶ g m⁻² day⁻¹. At 23 °C water vapor partial pressure at 100% RH is 0.02811 bar. Thereby at 50% RH water vapor partial pressure is 0.01405 bar. The partial pressure is needed to convert WVTR into water vapor permeability (WVP).

Supporting Information

Supporting Information is available from the Wiley Online Library or from the author.

Acknowledgements

J.Z. and C.H. contributed equally to this work. The authors thank Florian Puchtler for producing the synthetic hectorite and Marco Schwarzmann for preparing the samples via ion-slicing of the samples and the SEM and TEM measurements. Furthermore, C.H. and T.S. would like to thank the Elite Network Bavaria for financial and other support. The work was supported by the German Science Foundation (DFG) within the collaborative research project SFB 840.

Conflict of Interest

The authors declare no conflict of interest.

Keywords

clays, electrospinning, filter-through, gas barriers, nanocomposites

Received: December 20, 2018

Revised: February 27, 2019

Published online:

- [1] H. Gao, Y. Yang, O. Akampumuza, J. Hou, H. Zhang, X. Qin, *Environ. Sci.: Nano* **2017**, *4*, 864.
- [2] H. Souzandeh, B. Molki, M. Zheng, H. Beyenal, L. Scudiero, Y. Wang, W.-H. Zhong, *ACS Appl. Mater. Interfaces* **2017**, *9*, 22846.
- [3] H. Ma, B. S. Hsiao, B. Chu, *J. Membr. Sci.* **2014**, *452*, 446.
- [4] M. Stöter, D. A. Kunz, M. Schmidt, D. Hirsemann, H. Kalo, B. Putz, J. Senker, J. Breu, *Langmuir* **2013**, *29*, 1280.
- [5] M. Morits, T. Verho, J. Sorvari, V. Liljeström, M. A. Kostianen, A. H. Gröschel, O. Ikkala, *Adv. Funct. Mater.* **2017**, *27*, 1605378.
- [6] M. W. Möller, T. Lunkenbein, D. A. Kunz, H. Kalo, M. Schieder, J. Breu, *Z. Anorg. Allg. Chem.* **2010**, *636*, 2113.
- [7] H. Kalo, M. W. Möller, M. Ziadeh, D. Dolejš, J. Breu, *Appl. Clay Sci.* **2010**, *48*, 39.
- [8] C.-H. Zhou, Z.-F. Shen, L.-H. Liu, S.-M. Liu, *J. Mater. Chem.* **2011**, *21*, 15132.
- [9] C.-W. Chiu, J.-J. Lin, *Prog. Polym. Sci.* **2012**, *37*, 406.
- [10] T. Szabó, A. Szeri, I. Dékány, *Carbon* **2005**, *43*, 87.
- [11] S. Eigler, A. Hirsch, *Angew. Chem., Int. Ed.* **2014**, *53*, 7720.
- [12] Y. Cui, S. Kundalwal, S. Kumar, *Carbon* **2016**, *98*, 313.
- [13] E. Doblhofer, J. Schmid, M. Rieß, M. Daab, M. Suntinger, C. Habel, H. Bargel, C. Hugenschmidt, S. Rosenfeldt, J. Breu, *ACS Appl. Mater. Interfaces* **2016**, *8*, 25535.
- [14] D. A. Kunz, J. Schmid, P. Feicht, J. Erath, A. Fery, J. Breu, *ACS Nano* **2013**, *7*, 4275.
- [15] A. Eckert, T. Rudolph, J. Guo, T. Mang, A. Walther, *Adv. Mater.* **2018**, *30*, 1802477.
- [16] Y. Song, J. Geringer, S. Qin, J. C. Grunlan, *Ind. Eng. Chem. Res.* **2018**, *57*, 6904.
- [17] J. J. Kochumalayil, M. Bergensträhle-Wohlert, S. Utsel, L. Wägberg, Q. Zhou, L. A. Berglund, *Biomacromolecules* **2013**, *14*, 84.
- [18] M. A. Priolo, K. M. Holder, D. Gamboa, J. C. Grunlan, *Langmuir* **2011**, *27*, 12106.
- [19] E. S. Tsurko, P. Feicht, F. Nehm, K. Ament, S. Rosenfeldt, I. Pietsch, K. Roschmann, H. Kalo, J. Breu, *Macromolecules* **2017**, *50*, 4344.
- [20] F. Ding, J. Liu, S. Zeng, Y. Xia, K. M. Wells, M.-P. Nieh, L. Sun, *Sci. Adv.* **2017**, *3*, e1701212.
- [21] S. Rosenfeldt, M. Stöter, M. Schlenk, T. Martin, R. Q. Albuquerque, S. Förster, J. Breu, *Langmuir* **2016**, *32*, 10582.
- [22] M. Daab, N. J. Eichstaedt, C. Habel, S. Rosenfeldt, H. Kalo, H. Schießling, S. Förster, J. Breu, *Langmuir* **2018**, *34*, 8215.
- [23] M. Daab, N. J. Eichstaedt, A. Edenharter, S. Rosenfeldt, J. Breu, *RSC Adv.* **2018**, *8*, 28797.
- [24] L. J. Michot, I. Bihannic, S. Maddi, S. S. Funari, C. Baravian, P. Levitz, P. Davidson, *Proc. Natl. Acad. Sci. U. S. A.* **2006**, *103*, 16101.
- [25] Y. Mori, K. Togashi, K. Nakamura, *Adv. Powder Technol.* **2001**, *12*, 45.
- [26] H. Hemmen, N. I. Ringdal, E. N. De Azevedo, M. Engelsberg, E. L. Hansen, Y. Méheust, J. O. Fossum, K. D. Knudsen, *Langmuir* **2009**, *25*, 12507.

5. Appendix

- [27] M. W. Möller, D. A. Kunz, T. Lunkenbein, S. Sommer, A. Nennemann, J. Breu, *Adv. Mater.* **2012**, *24*, 2142.
- [28] F. Carosio, A. Di Pierro, J. Longi, A. Fina, G. Saracco, *J. Colloid Interface Sci.* **2018**, *510*, 142.
- [29] A. J. Svagan, A. Åkesson, M. Cárdenas, S. Bulut, J. C. Knudsen, J. Risbo, D. Plackett, *Biomacromolecules* **2012**, *13*, 397.
- [30] A. Greiner, J. H. Wendorff, *Angew. Chem., Int. Ed.* **2007**, *46*, 5670.
- [31] S. Jiang, Y. Chen, G. Duan, C. Mei, A. Greiner, S. Agarwal, *Polym. Chem.* **2018**, *9*, 2685.
- [32] S. Agarwal, A. Greiner, J. H. Wendorff, *Prog. Polym. Sci.* **2013**, *38*, 963.
- [33] Y. Ding, H. Hou, Y. Zhao, Z. Zhu, H. Fong, *Prog. Polym. Sci.* **2016**, *61*, 67.
- [34] H. Hou, W. Xu, Y. Ding, *J. Jiangxi Norm. Univ., Nat. Sci.* **2018**, *42*, 551.
- [35] S. Agarwal, M. Burgard, A. Greiner, J. Wendorff, *Electrospinning: A Practical Guide to Nanofibers*, Walter de Gruyter GmbH, Berlin **2016**.
- [36] S. Pandey, K. K. Jana, V. K. Aswal, D. Rana, P. Maiti, *Appl. Clay Sci.* **2017**, *146*, 468.
- [37] H. Kim, Y. Miura, C. W. Macosko, *Chem. Mater.* **2010**, *22*, 3441.
- [38] A. Mishra, B. P. D. Purkayastha, J. K. Roy, V. K. Aswal, P. Maiti, *Macromolecules* **2010**, *43*, 9928.
- [39] M. Joshi, B. Adak, B. Butola, *Prog. Mater. Sci.* **2018**, *97*, 230.
- [40] C. Anthony, S. Durand-Vidal, P. Turq, J. Brendle, *J. Colloid Interface Sci.* **2005**, *285*, 719.
- [41] H. Kalo, W. Milius, J. Breu, *RSC Adv.* **2012**, *2*, 8452.
- [42] S. M. Liff, N. Kumar, G. H. McKinley, *Nat. Mater.* **2007**, *6*, 76.
- [43] S. L. Phua, L. Yang, C. L. Toh, S. Huang, Z. Tsakadze, S. K. Lau, Y.-W. Mai, X. Lu, *ACS Appl. Mater. Interfaces* **2012**, *4*, 4571.
- [44] Y. Qian, C. I. Lindsay, C. Macosko, A. Stein, *ACS Appl. Mater. Interfaces* **2011**, *3*, 3709.
- [45] D. Sheng, J. Tan, X. Liu, P. Wang, Y. Yang, *J. Mater. Sci.* **2011**, *46*, 6508.
- [46] T. R. Crompton, *Physical Testing of Plastics*, Smithers Rapra, Akron, OH **2012**.
- [47] E. Cussler, S. E. Hughes, W. J. Ward III, R. Aris, *J. Membr. Sci.* **1988**, *38*, 161.
- [48] G. L. Yuan, W. M. Li, S. Yin, F. Zou, K. C. Long, Z. F. Yang, *J. Appl. Polym. Sci.* **2009**, *114*, 1964.
- [49] J. M. Herrera-Alonso, E. Marand, J. C. Little, S. S. Cox, *J. Membr. Sci.* **2009**, *337*, 208.
- [50] K. S. Miller, J. Krochta, *Trends Food Sci. Technol.* **1997**, *8*, 228.
- [51] U. Edlund, Y. Z. Ryberg, A.-C. Albertsson, *Biomacromolecules* **2010**, *11*, 2532.

5. Appendix

Copyright WILEY-VCH Verlag GmbH & Co. KGaA, 69469 Weinheim, Germany, 2019.

Supporting Information

Filter-through method of making highly efficient polymer-clay nanocomposite membranes

Jian Zhu, Christoph Habel, Theresa Schilling, Andreas Greiner, Josef Breu*, Seema Agarwal**

J. Zhu, Prof. A. Greiner, Prof. S. Agarwal,
Macromolecular chemistry II, Bavarian Polymer Institute and Bayreuth Center for Colloids and
Interfaces, University of Bayreuth, Universitätsstraße 30, Bayreuth, 95447, Germany
E-mail: greiner@uni-bayreuth.de, agarwal@uni-bayreuth.de

C. Habel, T. Schilling, Prof. J. Breu
Bavarian Polymer Institute and Department of Inorganic Chemistry, University of Bayreuth,
Universitätsstraße 30, Bayreuth, 95447, Germany
E-mail: Josef.Breu@uni-bayreuth.de

† These authors contributed equally to this work.

5. Appendix

Figures and Tables

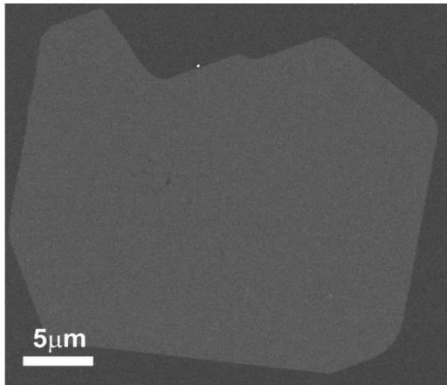


Figure S1. SEM image of a Hec platelet. The diameter is $>20\ \mu\text{m}$.

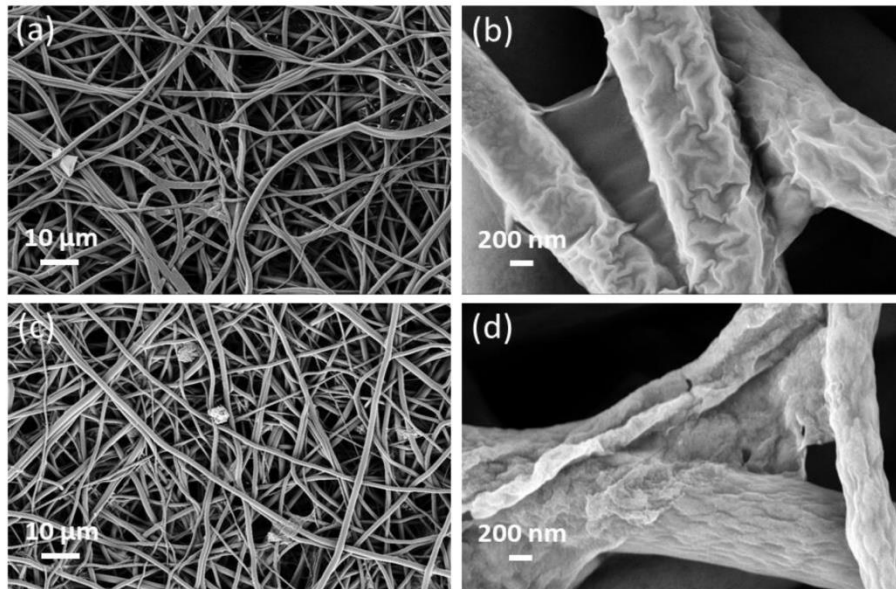


Figure S2. Filtration of MMT with concentration of $0.2\ \text{mg ml}^{-1}$ (a, b) and $0.65\ \text{mg ml}^{-1}$ (c, d) through electrospun TPU non-woven. MMT did not make a layer but seems to either wrap around the TPU fibers or passed through the filter due to its small diameter.

5. Appendix

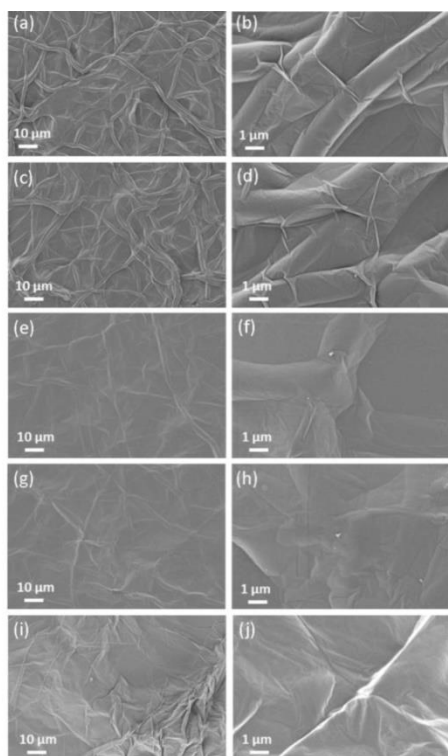


Figure S3. SEM images of PVP-clay deposited on the surface of TPU support. The amount of clay was 2 mg (a, d), 5 mg (c, d), 10 mg (e, f), 20 mg (g, h) and 65 mg (i, j) per 100 ml water in the suspension, respectively.

5. Appendix

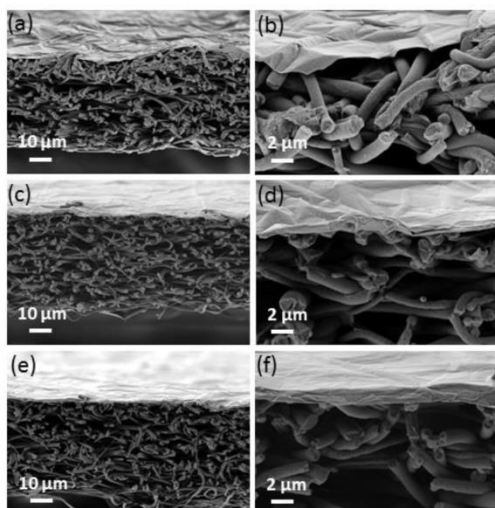


Figure S4. SEM images of cross section of bilayer TPU/PVP-Hec membrane with different amounts of Hec coating. The amount of Hec in the suspension filtered through TPU was 2 mg (**Figure 1**), 5mg (a, b), 10 (c, d), 20 mg (e, f) and 65 mg (**Figure 1**) per 100 ml, corresponding to the average thickness of PVP-Hec layers around 60nm, 160nm, 70nm, 1200nm and 5000 nm, respectively.

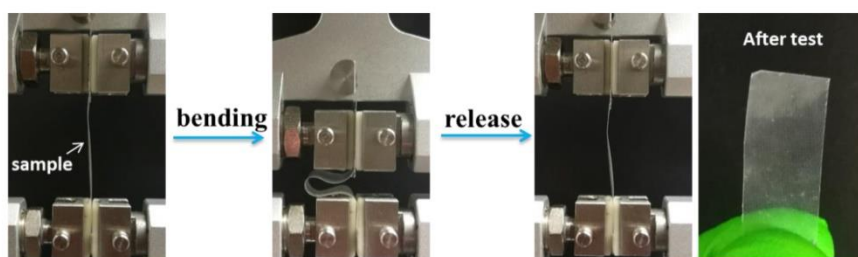


Figure S5. Bending test of p3L-PVP-Hec-29.5 laminate.

5. Appendix

Table S1. Summary of the transparent properties and thermal properties of laminates with different amounts of clay (p3L-PVP-Hec-X, X describes the Hec content).

Samples	Transmittance at 600 nm (%)	Content of Hec from TGA (wt%)
pTPU	72	0
p3L-PVP-Hec-3.5	77	3.5
p3L-PVP-Hec-5.2	79	5.2
p3L-PVP-Hec-7.7	76	7.7
p3L-PVP-Hec-9.1	79	9.1
p3L-PVP-Hec-29.5	62	29.5
p3L-PVP-Hec-6.2	77	6.2

Table S2. Mechanical properties (Strength, E-Modulus, Strain at break) of the neat pressed TPU support (pTPU) in comparison with the laminates with different amounts of clay (p3L-PVP-Hec-X, X describes the Hec content).

Samples	Strength (MPa)	E-modulus (MPa)	Strain at break (%)
pTPU	37±1.6	17±1.6	564±13.7
p3L-PVP-Hec-3.5	28±0.4	56±3.7	474±20.3
p3L-PVP-Hec-5.2	30±2.3	110±19	464±28.8
p3L-PVP-Hec-7.7	29±3.6	369±19.6	464±18.6
p3L-PVP-Hec-9.1	33±3.5	945±34.1	487±21.6
p3L-PVP-Hec-29.5	17±0.7	1117±138	471±21
p3L-PVP-Hec-6.2	27±2.0	17±1.6	564±13.7

5. Appendix

Table S3. OTRs (dry or 50% RH, room temperature) and calculated permeabilities (overall thickness of the laminates) of the neat TPU matrix and the nanocomposite foils in dependency of the Hec content and comparing the Oxygen Permeability (OP) of films reported in literature.¹⁻⁴

Samples	Overall thickness (μm)	OTR ($\text{cm}^3 \text{ m}^{-2} \text{ day}^{-1} \text{ bar}^{-1}$)	OP ($\text{cm}^3 \text{ cm m}^{-2} \text{ day}^{-1} \text{ bar}^{-1}$) ^a
pTPU	35	442.5	1.55
p3L-PVP-Hec-3.5	34	165.1	0.56
p3L-PVP-Hec-5.2	34	106.8	0.299
p3L-PVP-Hec-7.7	30	20.9	0.063
p3L-PVP-Hec-9.1	36	16	0.058
p3L-PVP-Hec-29.5	50	3.7	0.0185
p3L-PVP-Hec-6.2	34	110.5	0.377
PU*	56	753	4.22
PU*+8 wt% MMT	57	166	0.93
PU**	-	-	59.8
PU**+28 wt% Cloisite	-	-	3.3
LDPE	-	-	18.7
PET	38	-	0.146
HDPE	-	-	4.27
Polyester	-	-	0.156

^a In order to assist comparability, some of the values are recalculated to the same unit.

5. Appendix

References

- [1] G. L. Yuan, W. M. Li, S. Yin, F. Zou, K. C. Long, Z. F. Yang, *J. Appl. Polym. Sci.* **2009**, 114, 1964.
- [2] J. M. Herrera-Alonso, E. Marand, J. C. Little, S. S. Cox, *J. Membr. Sci.* **2009**, 337, 208.
- [3] K. S. Miller, J. Krochta, *Trends Food Sci. Tech.* **1997**, 8, 228.
- [4] U. Edlund, Y. Z. Ryberg, A.-C. Albertsson, Barrier films from renewable forestry waste, *Biomacromolecules* **2010**, 11, 2532.

6. List of Publications

6. List of Publications

- (1) **Zhu, J.**, Breu, J., Hou, H., Greiner, A., & Agarwal, S.. Gradient structured nonflammable flexible polymer membranes. *ACS applied materials & interfaces*, **2019**, 11 (12), 11876-11883
- (2) **Zhu, J.**, Habel, C., Schilling, T., Greiner, A., Breu J., Agarwal, S.. Filter-Through Method of Making Highly Efficient Polymer-Clay Nanocomposite Membranes. *Macromolecular Materials and Engineering*, **2019**, DIO: 10.1002/mame.201800779
- (3) **Zhu, J.**, Ding, Y., Agarwal, S., Greiner, A., Zhang, H., Hou, H.. Nanofibre preparation of non-processable polymers by solid-state polymerization of molecularly self-assembled monomers. *Nanoscale*, **2017**, 9(46), 18169-18174.
- (4) **Zhu, J.**, Jiang, S., Hou, H., Agarwal, S., & Greiner, A.. Low Density, Thermally Stable, and Intrinsic Flame Retardant Poly (bis (benzimidazo) Benzophenanthroline - dione) Sponge. *Macromolecular Materials and Engineering*, **2018**, 303(4), 1700615.
- (5) **Zhu, J.**, Ding, Y., Liao, X., Xu, W., Zhang, H., & Hou, H.. Highly flexible electrospun carbon/graphite nanofibers from a non-processable heterocyclic rigid-rod polymer of polybisbenzimidazobenzophenanthroline-dione (BBB). *Journal of materials science*, **2018**, 53(12), 9002-9012.
- (6) Hecht, M., Soberats, B., **Zhu, J.**, Stepanenko, V., Agarwal, S., Greiner, A., Würthner, F.. Anisotropic microfibres of a liquid-crystalline diketopyrrolopyrrole by self-assembly-assisted electrospinning. *Nanoscale Horizons*, **2019**, 4(1), 169-174.
- (7) Peng, L., **Zhu, J.**, & Agarwal, S.. Self - Rolled Porous Hollow Tubes Made up of Biodegradable Polymers. *Macromolecular rapid communications*, **2017**, 38(10), 1700034.
- (8) Ye, W., **Zhu, J.**, Liao, X., Jiang, S., Li, Y., Fang, H., Hou, H.. Hierarchical three-dimensional micro/nano-architecture of polyaniline nanowires wrapped-on polyimide nanofibers for high performance lithium-ion battery separators. *Journal of power sources*, **2015**, 299, 417-424.
- (9) Xu, W., Ding, Y., Jiang, S., **Zhu, J.**, Ye, W., Shen, Y., Hou, H.. Mechanical flexible

6. List of Publications

PI/MWCNTs nanocomposites with high dielectric permittivity by electrospinning.

European Polymer Journal, **2014**, 59, 129-135.

(Eidesstattliche) Versicherungen und Erklärungen

(§ 9 Satz 2 Nr. 3 PromO BayNAT)

Hiermit versichere ich eidesstattlich, dass ich die Arbeit selbstständig verfasst und keine anderen als die von mir angegebenen Quellen und Hilfsmittel benutzt habe (vgl. Art. 64 Abs. 1 Satz 6 BayHSchG).

(§ 9 Satz 2 Nr. 3 PromO BayNAT)

Hiermit erkläre ich, dass ich die Dissertation nicht bereits zur Erlangung eines akademischen Grades eingereicht habe und dass ich nicht bereits diese oder eine gleichartige Doktorprüfung endgültig nicht bestanden habe.

(§ 9 Satz 2 Nr. 4 PromO BayNAT)

Hiermit erkläre ich, dass ich Hilfe von gewerblichen Promotionsberatern bzw. -vermittlern oder ähnlichen Dienstleistern weder bisher in Anspruch genommen habe noch künftig in Anspruch nehmen werde.

(§ 9 Satz 2 Nr. 7 PromO BayNAT)

Hiermit erkläre ich mein Einverständnis, dass die elektronische Fassung meiner Dissertation unter Wahrung meiner Urheberrechte und des Datenschutzes einer gesonderten Überprüfung unterzogen werden kann.

(§ 9 Satz 2 Nr. 8 PromO BayNAT)

Hiermit erkläre ich mein Einverständnis, dass bei Verdacht wissenschaftlichen Fehlverhaltens Ermittlungen durch universitätsinterne Organe der wissenschaftlichen Selbstkontrolle stattfinden können.

.....
Ort, Datum, Unterschrift